

DATA DISCOVERY ON LIQUEFACTION-INDUCED LATERAL GROUND
DEFORMATIONS

by

Fang Liu

A Dissertation Presented to the
FACULTY OF THE GRADUATE SCHOOL
UNIVERSITY OF SOUTHERN CALIFORNIA
In Partial Fulfillment of the
Requirements for the Degree
DOCTOR OF PHILOSOPHY
(CIVIL ENGINEERING)

December 2008

Copyright 2008

Fang Liu

Dedication

to

the endless support of my parents

Binglin Liu, Hanying Huang

the tireless courage of my sister

Fen Liu

the strength of my husband

Yuanxin Ye

Acknowledgments

I would like to express my gratitude to everyone who has ever helped me with this study.

Particularly, my sincere gratitude goes to my advisor, Prof. Jean-Pierre Bardet, for his guidance and support during the entire course of my doctoral program. Special thanks are extended to my committee members, Prof. Geoffrey R. Martin, Prof. Iraj Ershaghi, Prof. Amy Rechenmacher, and Prof. Roger Ghanem, for their constructive criticism and advices. Special appreciation also goes to Prof. Craig Taylor, for his strong encouragement and generous help. Equally sincere gratitude goes to Prof. Jian-Min Zhang, my former advisor at Tsinghua University, for lightening my first desire to step into an adventurous field of research.

I would recognize the special contribution and many helpful suggestions from Dr. Jianping Hu and Dr. Craig Davis, who generously provided me valuable data, and shared with me their rich knowledge and experiences. I would also thank Saikiran Vajrapu for helping me to program Web interfaces.

A special note of appreciation goes to my graduate fellows, Xiuying Xing and Zhiqing Kou, for their constant support and friendship. My gratitude also extends to my colleagues in the geotechnical engineering group, Dr. Youngsoo Lee, Amir Zand, and

Nazila Mokarram, for contributing a friendly and inquisitive atmosphere I found at the University of Southern California.

Finally, I would appreciate my family's continuing understanding and support. They provided me strength to turn fears into desires to succeed.

Table of Contents

Dedication	ii
Acknowledgments	iii
List of Tables	viii
List of Figures	ix
Abbreviations	xiv
Abstract	xvi
Chapter 1. Introduction	1
1.1. Liquefaction and Lateral Ground Deformations	1
1.2. Learning from Earthquakes	3
1.3. Research Objectives	4
1.4. Organization of Dissertation	5
Chapter 2. Past Empirical Procedures of Liquefaction Evaluation	7
2.1. Mechanism of Liquefaction-Induced Lateral Ground Deformation	7
2.2. Physical Origins of Liquefaction-Induced Lateral Deformations	12
2.3. Case Histories of Liquefaction-Induced Deformations	13
2.3.1. Bartlett and Youd (1992) Database	13
2.3.2. Rauch (1997) Database	15
2.3.3. USC Database (Bardet et al. 1999)	16
2.4. Simplified Procedure for Predicting Liquefaction Occurrence	18
2.4.1. Generic Methodology	19
2.4.2. Stress-Based Models	20
2.4.3. Energy-Based Models	26
2.5. Liquefaction Potential Index	27
2.6. Models for Liquefaction-Induced Lateral Ground Deformation	29
2.6.1. Empirical Formulations Derived from Sliding Block Analogy	29
2.6.2. Regression Models Based on Case Histories	32
2.7. Summary	36
Chapter 3. Information Management for Post-Earthquake Reconnaissance	38
3.1. PER and Earthquake Engineering	38
3.2. Techniques Employed in PER	45

3.2.1.	Application of GPS	45
3.2.2.	Geo-Referencing Photos	47
3.2.3.	Embedding Metadata into Photos	47
3.3.	Evolution of PER Information Release	49
3.3.1.	Internet Application	50
3.3.2.	Web-Based GIS System	51
3.3.3.	Google Maps Application	53
3.4.	Next Step – Embedded Metadata	57
3.4.1.	Application of Embedded Metadata	57
3.4.2.	Example – 2008 Wenchuan Earthquake	59
3.5.	Scale-up to Virtual Earthquake	62
3.5.1.	Extensible Format	63
3.5.2.	Data Quality and Search Engine	64
3.6.	Summary	65
Chapter 4.	Information System for Liquefaction Case Histories	66
4.1.	Sharing Geotechnical Information	66
4.2.	Web-based GIS Systems for Sharing Spatial Data	67
4.3.	Application of Google Maps	71
4.4.	Lightweight System for Liquefaction Case Histories	72
4.4.1.	System Architecture	72
4.4.2.	System Configuration	73
4.4.3.	Data Structure	74
4.4.4.	Optimization of Vector Rendering	75
4.4.5.	Major Functions and User Interfaces	78
4.5.	Summary	82
Chapter 5.	Case Study of Liquefaction Assessment	83
5.1.	Site Description and Earthquake Impacts	83
5.2.	Seismic Strong Motions	87
5.3.	Topographic Setting	89
5.4.	Subsurface Soil Conditions	90
5.4.1.	Regional Geology	90
5.4.2.	Geotechnical Investigation Data	91
5.5.	Ground Water Level	94
5.6.	Liquefaction Severity Assessment	96
5.7.	Evaluation of Liquefaction-Induced Lateral Deformations	98
5.7.1.	Youd et al. (2002) Model	98
5.7.2.	Bardet et al. (2002) model	101
5.7.3.	Zhang et al. (2004) model	102
5.8.	Summary	103
Chapter 6.	Motions of Gently Sloping Ground during Earthquakes	105
6.1.	Model for Gently Sloping Ground	105

6.2.	Seismic Deformation of Statically Unstable Sloping Ground	110
6.3.	Factors Controlling Motions of Unstable Sloping Ground	115
6.4.	Probability for Earthquake Contribution δ	119
6.5.	Probability for Earthquake Contribution δ'	122
6.6.	Application to Case Histories	128
6.7.	Summary	132
Chapter 7.	Summary and Conclusions	133
7.1.	Summary of Research	133
7.2.	Highlights of Original Contributions	135
References		137
Appendix A	Tabulated Results of Case Study	147

List of Tables

Table 2.1	Databases of case histories of liquefaction-induced deformations	14
Table 2.2	Summary of the USC database (Bardet et al. 1999; Hu 2003)	17
Table 2.3	Liquefaction severity categories based on <i>LPI</i>	28
Table 2.4	Parameters of empirical models for liquefaction-induced lateral displacement	33
Table 3.1	Organizations releasing PER information	43
Table 3.2	PER reports released by GEES	44
Table 5.1	Seismic parameters and resulting maximum deformations in two quakes	85
Table 6.1	Summary of case histories of liquefaction-induced lateral ground deformations in gently sloping ground	129
Table A.1	Calculation results of case study	147

List of Figures

Figure 1.1	Data / Discover phases and dissertation organization	5
Figure 2.1	Timing of ground deformation and earthquake: (a) simultaneous with earthquake; and (b) delayed after earthquake (after Bardet 2003; Towhata et al. 1999)	12
Figure 2.2	Algorithm for average (courtesy of Bardet et al. 2002)	15
Figure 2.3	Comparison between Bartlett and Youd (1992) database and USC database	17
Figure 2.4	A sample site deformed during: (a) the 1971 quake; and (b) the 1994 quake	18
Figure 2.5	Capacity against liquefaction derived from case histories (modified from Kramer 1996)	19
Figure 2.6	Liquefaction resistance based on SPT results (courtesy of Youd et al. 2001)	22
Figure 2.7	Liquefaction resistance based on CPT results (courtesy of Robertson and Wride 1998)	23
Figure 2.8	Energy-based procedures based on (a) SPT N-value; and (b) CPT penetration (courtesy of Kayen and Mitchell 1997)	27
Figure 2.9	Newmark sliding theory: (a) block analogy (after Newmark 1965); and (b) double integration approach (after Wilson and Keefer 1983)	29
Figure 3.1	Advances in earthquake engineering after major earthquakes	39
Figure 3.2	Timeframe of field investigations after major earthquakes (After Holzer et al. 2003, modified from LFE)	40
Figure 3.3	Sequence of major events in NSF-sponsored PER	41

Figure 3.4	Exponential growth of information volume archived on the GEES website since the inception of the Internet	44
Figure 3.5	Geo-referencing a picture using its timestamp and a GPS track log	46
Figure 3.6	Layer structure for GIS systems	52
Figure 3.7	Main tools used in PER	52
Figure 3.8	GEES photo repository integrating Google Maps with database	54
Figure 3.9	Software configurations for GEES photo repository	55
Figure 3.10	PER photos searchable through earthquake names	56
Figure 3.11	GEES repository of aerial and field surveys for 2004 Japan earthquake	56
Figure 3.12	Workflow for generating and archiving photos with embedded metadata	58
Figure 3.13	HTML Web album generated for the 2008 Wenchuan earthquake	60
Figure 3.14	PER data displayed by Google Earth (map data from Google Earth)	61
Figure 3.15	PER data displayed by Google Maps (map data from Google Maps)	62
Figure 3.16	A system supporting multiple contributors and users	63
Figure 4.1	Self-supported Web applications	68
Figure 4.2	Web application using external data over Web services	70
Figure 4.3	Lightweight Web application	70
Figure 4.4	Major components constituting a lightweight system	73
Figure 4.5	Software configurations	73
Figure 4.6	Relational diagram	75
Figure 4.7	Dynamic tiles split when zoom level varies	76

Figure 4.8	Mapping a displacement vector into raster image formed by pixels	77
Figure 4.9	Entry page (map data from Google Maps)	79
Figure 4.10	Available boreholes and displacements for the 1971 San Fernando, California, earthquake (map data from Google Maps)	80
Figure 4.11	Satellite imagery as the background for the data set of Figure 4.10 (map data from Google Maps)	80
Figure 4.12	Communications between clients and servers	81
Figure 5.1	Liquefaction-related ground failures in the VNC vicinity after the 1971 and 1994 earthquakes (from USGS 1996)	84
Figure 5.2	USGS ShakeMap for the 1994 shake: (a) Instrumental intensity; and (b) PGA (maps from USGS website http://www.usgs.gov/)	87
Figure 5.3	PGA at the study site during: (a) the 1971 quake; and (b) the 1994 quake (data from USGS website http://www.usgs.gov/)	88
Figure 5.4	Accelerograms recorded at the Jensen Filter Plant Station during the 1994 quake (data source: http://peer.berkeley.edu)	88
Figure 5.5	Accelerograms recorded at the Sylmar Converter Station during the 1994 quake (data source: http://peer.berkeley.edu)	89
Figure 5.6	Slope map of the study site	90
Figure 5.7	Geologic setting in the VNC vicinity	91
Figure 5.8	Spatial distribution of available geotechnical borings	92
Figure 5.9	Consultant firms involved in collection of geotechnical boring data	93
Figure 5.10	Drilling year of geotechnical boring data	93
Figure 5.11	Interpolated GWL map of the 1994 earthquake; labeling numbers are the ground water depth in meters below the ground surface	95
Figure 5.12	Interpolated GWL map of the 1971 earthquake;	95
Figure 5.13	An example of <i>LPI</i> calculation	96

Figure 5.14	Spatial distribution of LPI showing the liquefaction severity	97
Figure 5.15	An example for calculating T_{15} from CPT test results	99
Figure 5.16	T_{15} map showing the liquefiable thickness; dots labeled with F_{15} values in percentage followed by the D_{5015} values in mm	100
Figure 5.17	Predicted lateral ground deformations based on Youd et al. (2002) model	101
Figure 5.18	Predicted lateral ground deformations based on Bardet et al. (2002) model	102
Figure 5.19	Predicted lateral ground deformations based on Zhang et al. (2004) model	103
Figure 6.1	Geometry, forces and stresses of an idealized gently sloping ground	106
Figure 6.2	Shear resistance of rigid - perfectly plastic interface	107
Figure 6.3	Instability due to loss in shear strength: (a) time histories of static shear stress and shear strength; and (b) time history of safety factor varying between F_s and F_i	108
Figure 6.4	Algorithm for calculating cumulative displacement	110
Figure 6.5	Time histories of earthquake acceleration recorded at Rinaldi Receiving Station during the 1994 Northridge, California, earthquake (data source: http://peer.berkeley.edu)	111
Figure 6.6	Time histories of stress ratio of a 5° slope when $F_i=2, 0.9$ and 0.4	112
Figure 6.7	Time histories of mass velocity and ground velocity when $F_i= 2, 0.9$ and 0.4	114
Figure 6.8	Time histories of mass displacement for $F_i = 2, 0.9$ and 0.4 corresponding to velocity of Figure 6.7	114
Figure 6.9	Definitions of earthquake contributions to unstable ground motions: δ - areas between Lines A and B; δ' - areas between Lines A and B'	117
Figure 6.10	Histograms and empirical probabilities for PGV ; PGA ; and Arias Intensity when $\delta_{\theta}=1$ cm and 10cm (Y defined in Equation 6.8);	

earthquake data from PEER strong motion database, http://peer.berkeley.edu/	121
Figure 6.11 Histograms and empirical probabilities for parameters F_i and θ when $\delta_0=1$ cm and 10cm	122
Figure 6.12 Histograms and empirical probabilities for seismic parameters: PGV ; PGA ; Arias Intensity when $\delta_0'=1$ cm and 10cm (Y' defined based on δ')	124
Figure 6.13 Histograms and empirical probabilities for physical parameters F_i and θ when $\delta_0' =1$ cm and 10cm	125
Figure 6.14 Histograms and empirical probabilities of k_s when $\delta_0' =1$ cm and 10cm	126
Figure 6.15 Probability curves predicted by Equation (6.12) for various values of F_i , θ and δ_0'	127
Figure 6.16 Histograms of (a) measured displacements; (b) liquefiable soil thickness; and (c) slope (data after Bartlett and Youd, 1995; Bardet et al., 1999)	130
Figure 6.17 Comparison between measured displacement and displacement computed from Equation (6.13)	131

Abbreviations

AJAX	Asynchronous JavaScript and XML
API	Application Program Interface
BOD	BOrehole Database
CPT	Cone Penetration Test.
DBMS	Database Management System
DGPS	Differential GPS
EERI	Earthquake Engineering Research Institute
EQII	Earthquake Image Information
EXIF	Exchangeable Image File Format
FTP	File Transfer Protocol
GEES	Geotechnical Earthquake Engineering Server
GEER	Geo-Engineering Earthquake Reconnaissance
GIS	Geographic Information System
GML	Geography Markup Language
GPS	Global Position System
HTML	HyperText Markup Language
IMS	Internet Map Service
IPTC	International Press Telecommunications Council
LIDD	Liquefaction-Induced ground Deformation Database
LFE	Learning from Earthquake

MCEER	Multidisciplinary Center for Earthquake Engineering Research
MLR	Multiple Linear Regression
NCSA	National Center for Supercomputer Applications
NEHRP	National Earthquake Hazard Reduction Program
NISEE	National Information Service for Earthquake Engineering
NSF	National Science Foundation
PER	Post-Earthquake Reconnaissance
PHP	Hypertext Preprocessor
PGA	Peak Ground Acceleration
PGV	Peak Ground Velocity
SPT	Standard Penetration Test
USGS	U.S. Geological Survey
WAAS	Wide-Area Augmentation System
XML	Extensible Markup Language
XMP	Extensible Metadata Platform

Abstract

Liquefaction-induced deformations during earthquake pose considerable risks to lifeline systems in urban areas. Empirical models, benefiting from case histories, are preferable for regionally assessing those deformations. Case histories of liquefaction grow rapidly and require new information technologies in data management. Based on pure regression analysis, those existing empirical models explain little physical mechanism. The objectives of this research are to improve data management of liquefaction-related case histories, and to develop the new generation of models that corroborate physical mechanism of liquefaction-induced lateral ground deformations. This goal is approached in four major steps.

The first step provides guidelines on gathering perishable information and automating Web reports of Post-Earthquake Reconnaissance (PER). Embedded metadata formats are applied to an example of the 2008 Wenchuan, China earthquake when documenting PER data. This application identifies the potential of inline metadata formats in establishing the Virtual Earthquake, a global-wide information system for archiving and sharing PER data in a spatial context.

The second step presents a new information system useful for distributing case histories of liquefaction-induced ground deformations over the Word Wide Web. Benefiting from

AJAX (Asynchronous JavaScript and XML), and database technologies, this system is an interactive and lightweight application supported by external data from multiple data vendors.

The third step scrutinizes existing empirical models using a subset of case histories that are gathered and managed in the previous steps. This case study develops maps of liquefaction severity and liquefaction-induced lateral deformations from those existing models. The disagreement between the simulation results and the field observations infers a knowledge insufficiency in the regional evaluation of liquefaction-induced lateral ground deformations and therefore raises a demand for the next generation of models.

The fourth step is towards a new model that corroborates physical mechanism of liquefaction-induced deformations. Using a physical model and probabilistic analysis, PGV (Peak Ground Velocity) is demonstrated to be a significant parameter that characterizes earthquake contributions to the motions of mass that temporarily loses shear strength due to liquefaction. A PGV-dependent model is derived based on case histories to account for the importance of PGV for liquefaction-induced lateral ground deformations.

Chapter 1. Introduction

1.1. Liquefaction and Lateral Ground Deformations

Originally coined by Mogami and Kubu (1953), liquefaction is those behaviors of loose saturated cohesionless soils associated with the generation of excess pore pressure under undrained conditions. In a more formal manner, liquefaction is defined as “the transformation of a granular material from a solid to a liquid state as a consequence of increased pore-water pressure and reduced effective stress” (Marcuson 1978). As a direct cause of liquefaction, excess pore pressure buildups are the consequences of earthquakes or other rapid loads.

Liquefaction and its related phenomena have been responsible for a tremendous amount of damage in historical earthquakes around the world. Liquefied soils may exhibit considerable losses in shear strength, leading to localized hazards (e.g., foundation bearing failure, structural settlements, etc.) or even pervasive ground failures such as large translational deformations. Those deformations often take place on relatively flat areas (i.e., with inclination angle less than 10°) underlain by recent alluvial and deltaic deposits as well as loosely placed sandy fills along streams and other waterfront. They could cover several square kilometers of soil deposits that laterally shift up to the order of ten meters. They could be caused by different mechanism associated with liquefaction, e.g., lateral spreads and flow slides (see Kramer 1996 for distinction). In this dissertation,

the term “liquefaction-induced lateral ground deformations” refers to all those horizontal deformations occurred on gently sloping ground in contrast to vertical settlements.

Spectacular examples of lateral ground deformations due to liquefaction during earthquakes were observed and documented in the past. In Alaska earthquake, as recalled in post-earthquake reconnaissance reports (e.g., Seed 1968; Youd 1978), over 250 highway and railway bridges were distorted by liquefaction-induced lateral spreads. In the 1971 San Fernando earthquake, a large slide, extending from the Juvenile Hall in San Fernando Valley towards southwest, laterally displaced railroad tracks. During the 1995 Hyogoken-Nanbu, Japan earthquake, liquefaction-induced ground deformations substantially damaged lifelines, pile-foundations of buildings and bridge piers along the Kobe shoreline (e.g., Hamada et al. 1996a; Hamada et al. 1996b; Karube and Kimura 1996; Matsui and Oda 1996; Tokimatsu et al. 1996). During the 1999 Kocaeli, Turkey, earthquake, liquefaction-induced deformations were so pervasive that they completely destroyed water-supply network throughout the city of Adaparazi, Turkey (e.g., Youd et al. 2000).

Liquefaction-induced lateral ground deformations pose catastrophic influences particularly on urban lifeline systems, such as utility lines and transportation routes, which should continue uninterrupted operation during and after an earthquake. Those deformations are extremely disruptive in developed areas, since they most likely occur in areas that are attractive to urban developments. Even though a site is identified to be susceptible to liquefaction, it can not always be avoided by a wide-spreading network of

lifelines. A regional prediction of liquefaction-induced lateral ground deformations is significant for preliminarily assessing their potential impacts and recognizing a need of mitigation.

1.2. Learning from Earthquakes

Liquefaction-induced lateral ground deformations are being studied from different angles using experimental tests, analytical models, numerical simulations and empirical simplifications (Bardet 2003). Depending on less site-specific parameters, empirical models are derived from case histories using regression analysis. They are particularly useful in the geotechnical screening process for predicting those deformations on regional scales (e.g., Bardet et al. 1999; Bartlett and Youd 1992; Zhang et al. 2004). They are favorable in risk assessments of lifeline systems for obtaining a preliminary assessment of liquefaction-induced hazards over relatively large regions (e.g., Werner et al. 2006).

Empirical models are based on collections of case histories that were gathered and preserved in the past. The quality and sufficiency of those data are essential to enable a robust model that offers statistically correct predictions. To author's knowledge, existing empirical models were developed from databases including a few hundred measurements (e.g., Bartlett and Youd 1992). They corroborated little physical mechanism since they were purely derived from regression analysis. With the advances in modern survey techniques, available case histories are growing rapidly and forming a robust database consisting of numerous cases (e.g., Bardet et al. 1999; Hu 2003). However, their potential

values have not yet been fully exploited. They require to be handled using new information technologies. They may substantially improve current procedures for deformation prediction, and enable the next generation of models that corroborate more physical mechanism of liquefaction-induced lateral ground deformations.

1.3. Research Objectives

The objectives of this research are: (1) to improve data management for case histories of liquefaction-induced lateral ground deformations; and (2) to develop the next generation of models for predicting those deformations on regional scales.

As illustrated in Figure 1.1, the objectives of this dissertation are approached from two research phases: data phase and discovery phase, each of which includes two steps leading to four core chapters presented in this dissertation. The first phase is intended to apply new information technologies to the management of case histories so that they can be effectively collected, documented and distributed. This phase is to construct an effective data infrastructure that supports the second phase. The discovery phase extends the previous phase to the data utilization. Its emphasis is to scrutinize the existing procedures and to develop the new generation of models for predicting liquefaction-induced lateral ground deformations on regional scales.

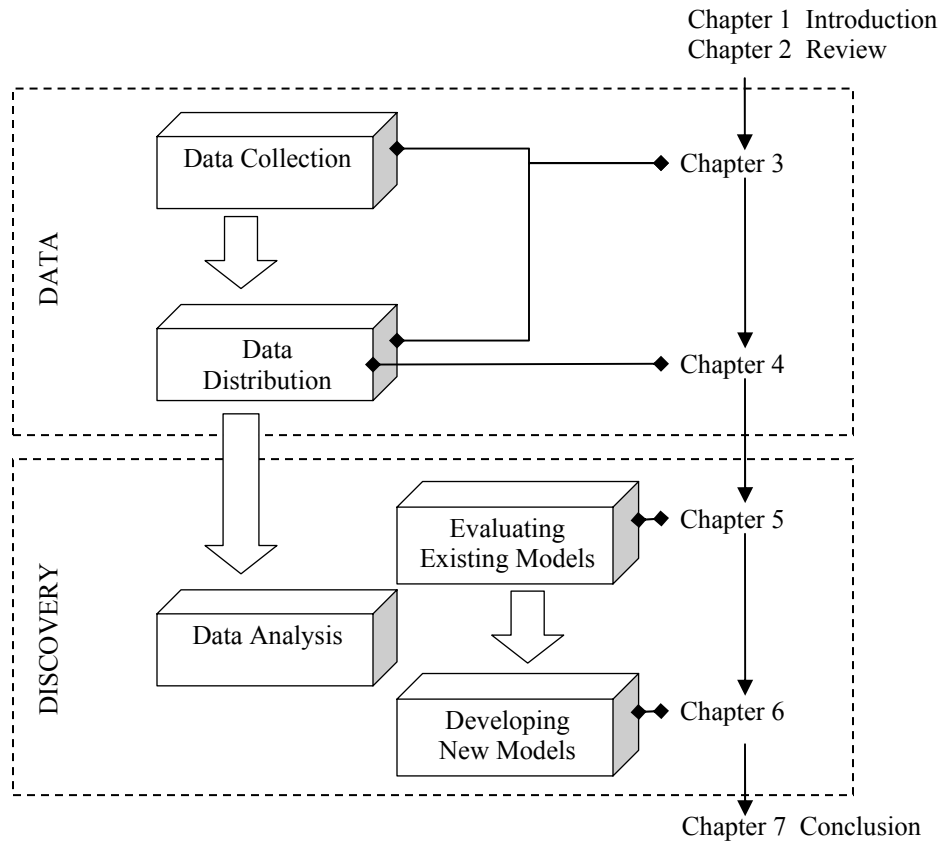


Figure 1.1 Data / Discover phases and dissertation organization

1.4. Organization of Dissertation

Figure 1.1 also shows the organization of this dissertation. Following this introduction chapter, Chapter 2 reviews past studies on liquefaction-related deformations based on case histories of liquefaction. Chapter 3 illustrates how to utilize advanced information technologies to effectively collect, document and distribute PER (Post-Earthquake Reconnaissance) data so that they are fully accessible and usable in a broad community.

This Chapter depicts a technology evolution of PER since the inception of the Internet. It also projects a future trend in globally sharing PER information. Chapter 4 presents a Web-based database-driven system for distributing case histories of liquefaction-induced lateral ground deformations. It illustrates the architecture and configuration of this system in technical point of view. Chapter 5 presents a case study to scrutinize existing empirical models and to explore the necessity of new models for regionally predicting liquefaction-induced lateral ground deformations. Chapter 6 develops a physical model to study the earthquake contributions to the motions of gently sloping ground that has temporarily lost shear strength during earthquakes. The controlling parameters are examined through the physical model and probabilistic analysis. This Chapter also illustrates a new empirical model derived from case histories to corroborate findings of probabilistic analysis. Finally, Chapter 7 summarizes the entire research and highlights the original contributions.

Chapter 2. Past Empirical Procedures of Liquefaction Evaluation

Liquefaction-related studies consist of two major branches, evaluation of liquefaction occurrence and resulting consequence. Different from other methodologies (e.g., experimental tests, numerical simulations, and analytical models), the empirical procedures benefit from case histories of liquefaction. They have advantages over other site-specific approaches for preliminary assessments of liquefaction-induced lateral ground deformations on regional scales. This chapter mainly reviews the procedures and models used in the geotechnical screening process to investigate those deformations.

2.1. Mechanism of Liquefaction-Induced Lateral Ground Deformation

The mechanism of liquefaction-induced lateral ground deformation has been primarily explored through experimental simulations by utilizing shake tables and centrifuge apparatus under controlled conditions. Those experimental studies are particularly helpful in identifying dominant factors that control deformations associated with liquefaction during earthquakes.

1g shake table tests are relatively favorable in Japan (e.g., Towhata 2005). In this type of tests, either scaled or full scale models (e.g., Kagawa et al. 1997) are constructed and placed on a shake table that transfers a pre-designed input excitation to the models. Due to high cost, full-scale models are seldom used in regular engineering practice. Because

scaled models only scale dimensions of soil strata under the normal earth gravity, they cannot produce a representative stress state that matches the field. In the meanwhile, scaled models cause shorter drainage path and faster dissipation of pore pressure than reality. For compensating these limitations, seismic excitations are often elongated artificially in order to represent a fairly long earthquake. The results are therefore interpreted as the maximum possible displacements (Rauch 1997).

Centrifuge tests are competent in simulating the representative stress conditions based on the scale law. In addition, they solve the problem caused by artificially shortened drainage path by replacing water with viscous fluid in physical models. Numerous centrifuge testing results were well documented in Arulanandan and Scott (1993) for a cooperative research project called VELACS (Verification of Liquefaction Analysis by Centrifuge Studies). Some of those tests were intended for exploring the mechanism of liquefaction-induced lateral ground deformations. They provide insights into the following puzzles: (1) dominant factors controlling the magnitude of lateral displacements; (2) delayed deformations; and (3) strain localization prone to form a sliding failure.

In general, factors that dominate deformations associated with liquefaction can be identified from a set of speculated factors using pre-designed centrifuge tests. Those factors can be grouped into three categories: seismic parameters, soil property parameters and geometry parameters. As commonly agreed, earthquake strong motions exert appreciable effects to liquefaction-induced lateral ground deformations. Accordingly, a

few seismic parameters (e.g., the peak ground acceleration, frequency content and strong motion duration) grabbed special attentions. They were extensively examined on centrifuge apparatus. In the mean time, inherent characteristics of soil deposits, such as liquefiable thickness, grain size, initial density, and fine content, received equally extensive explorations. Sharp et al. (2003) recently identified the permeability in soil deposits to be a significant factor largely affecting the deformation patterns. They found out that permanent lateral displacements decreased with the increasing permeability. Geometry boundaries of ground also have substantial influences to displacements. They affect displacements through the slop angle of ground or the free surface ratio, a ratio of the height of a vertical cut against its distance to the location where a displacement is measured.

Those controlling parameters, which are identified by experimental tests, sometimes interact with each other and exhibit coupling effects to the ultimate deformations of liquefied soils. For instance, Kutter et al. (2004) identified the overall effects of density and thickness of liquefiable soils that contributed to permanent lateral deformations. They defined a new parameter (i.e., known as deformation index) to describe the combined influences of depth, density, and thickness on lateral displacements occurred in liquefied soil deposits. Taboada and Dobry (1998) investigated the combined influence of input peak acceleration and the frequency. They concluded that these two parameters affected the permanent lateral ground deformations through the thickness of liquefied soil deposits;

In other words, if the liquefied thickness is considered, the lateral displacements are independent of the peak input acceleration and the frequency.

From a conventional point of view, a gently sloping ground hardly deforms after strong motions end, because the static shear stress of the ground is so small that the residual shear strength of liquefied soils is still sufficient against slip driven by the gravity. The steady-state theory supports this argument. However, delayed deformations after earthquakes have been witnessed in the field. For instance, San Fernando Dam failed a few minutes after the 1971 San Fernando earthquake. Researchers started to question the values of residual shear strength that are originated from the steady-state theory. For instance, Baziar and Dobry (1995) addressed that the values of residual shear strength obtained in laboratories were 1.5-2 times larger than those back-calculated from stability analyses on post-failure configurations. Kulasingam et al. (2004) back-calculated the residual shear strength using centrifuge results, and suggested non-unique correlations between the values of pre-earthquake penetration resistances and the residual shear strength. How to obtain a precise value of the residual shear strength for liquefied soils remains controversial.

Centrifuge tests were designed to reproduce in laboratories delayed deformations in liquefied soil deposits. Instead of uniform soil strata (e.g., Sharp et al. 2003; Taboada and Dobry 1998), layered soil deposits were simulated using centrifuge apparatus. Those tests found some appraisal results. Further investigations demonstrated that thin interlayers of silts within liquefied sands substantially changed the mode of liquefaction-induced

ground movements. Pore water in liquefied sands is prone to go upward during earthquake shaking. As a result, liquefied sands tend to be densified at the bottom while loosened above. This phenomenon is termed as void redistribution which has been well-explained in Kulasingam et al. (2006) and Malvick et al. (2006). Due to the presence of seams of silts or clays, water is trapped and consequently forms a film along interfaces between sands and materials of low permeability (e.g., Kokusho 1999; Kokusho and Fujita 2002; Kokusho and Kojima 2002). If water films connect each other after a long disturbance, they can develop a sliding plane with very low shear strength. In this circumstance, catastrophic ground deformations can happen and continue after earthquakes until the reduced shear strength recover to a level larger than the driven static shear stress. The duration of recovery depends on the diffusion rate of excess pore pressure, and ultimately depends on the permeability in soil deposits and the surrounding environment of drainages. In conditions of slow diffusion, delayed deformations are possible.

Centrifuge tests on homogenous soil deposits produce sinusoidal shapes of deformation profiles with depths (e.g., Sharp et al. 2003; Taboada and Dobry 1998). In the contrary, those tests on layered deposits susceptible to water films reported localized deformations as well (e.g., Kulasingam et al. 2004; Malvick et al. 2006; Taboada and Dobry 1998). They provide supports to the sliding block theory that assumes a well-defined sliding surface caused by the presence of localized zone of strain.

2.2. Physical Origins of Liquefaction-Induced Lateral Deformations

The physical origins of lateral deformations induced by soil liquefaction and pore pressure buildups are still ruled by controversies. In general, both earthquake transient shakings and unbalanced gravity contribute to liquefaction-induced lateral ground deformations (Bardet 2003).

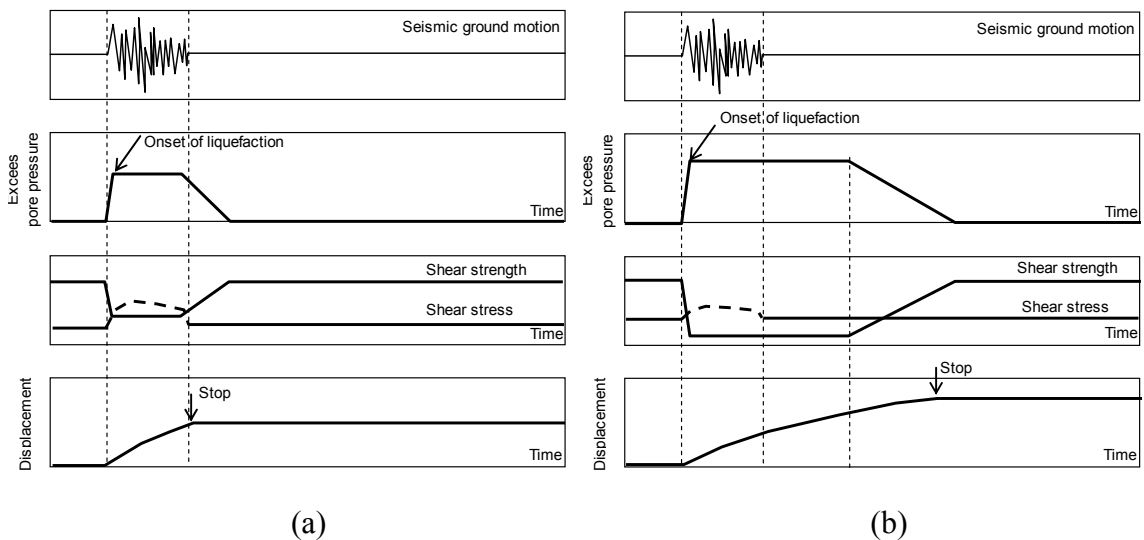


Figure 2.1 Ground deformations: (a) simultaneous with earthquake; and (b) delayed after earthquake (after Bardet 2003; Towhata et al. 1999)

Towhata et al (1999) reconciled field and laboratory observations invoking a simplified model as shown in Figure 2.1. During earthquakes, the pore pressure rises until soil deposits liquefy. The soils remain liquefied over a time interval then gradually solidify and consolidate as the pore pressure decreases. The timing and duration of the liquefaction-induced deformations depend on: (1) the time history of the driving stress and the shear strength; and (2) drainage conditions. Deformations start when the shear

strength is smaller than the driving shear stress, and decelerate when the shear strength becomes larger than the driving shear stress. In a case of rapid drainage as shown in Figure 2.1(a), the shear strength may be restored right after the shaking ends; deformations stop with the shaking. In a case of slower drainage as shown in Figure 2.1(b), the shear strength regains more slowly; deformations may extend after the shaking.

2.3. Case Histories of Liquefaction-Induced Deformations

2.3.1. Bartlett and Youd (1992) Database

The database compiled by Bartlett and Youd (1992) received more attentions than others. It is accessible on the Internet at <http://www.et.byu.edu/>. This database is amended continuously with additional data sets, and it has invoked a few empirical models for predicting liquefaction-induced lateral ground deformations (e.g., Bardet et al. 2002; Bartlett and Youd 1995; Zhang et al. 2004; Zhang and Zhao 2005).

The Bartlett and Youd (1992) database is summarized in Table 2.1 along with other two databases compiled in the past that gathered case histories of liquefaction-induced lateral ground deformations. The Bartlett and Youd (1992) database contains 467 case histories collected from 7 historical earthquakes occurred in Japan and the United States since 1906. Those displacements were measured with various accuracies that range from 2 to 72 centimeters. They form two categories: one includes measurements obtained from gently sloping ground, and the other includes measurements close to free surfaces. This

database later received minor corrections (Youd et al. 2002) and modifications leading to new sets of data (e.g., Rauch 1997; Zhang et al. 2004).

Table 2.1 Databases of case histories of liquefaction-induced deformations

Earthquake	Database	Bartlett & Youd (1992)	Zhang et al (2004)	Bardet et al. (1999)
1906 San Francisco		4 (± 0.1 to ± 0.5)	8 (± 0.1 to ± 0.5)	-
1923 Kanto		-	1 (> 0.5)	-
1948 Fukui		-	4 (± 1.90)	-
1964 Alaska		7 (± 0.1 to ± 0.5)	1 (± 0.1 to ± 0.5)	-
1964 Niigata		299 (± 0.72)	201 (± 0.72)	2498
1971 San Fernando		28 (± 0.47)	14 (± 0.47)	835 (± 0.330)
1979 Imperial Valley		32 (± 0.02)	17 (± 0.1 to ± 0.5)	-
1983 Nihonkai-Chubu		72 (± 0.17)	23 (± 0.17)	2954
1983 Borah Peak		-	-	-
1987 Superstition Hills		6 (± 0.1 to ± 0.5)	3 (± 0.02)	-
1989 Loma Prieta		-	6 (> 0.1)	-
1990 Dagupan		-	7 (> 0.5)	-
1993 Hokkaido		-	6 (± 0.22)	-
1994 Northridge		-	-	1011 (± 0.330)
1995 Hyogoken-Nanbu		-	-	8897
1999 Kocaeli		-	-	1706
Others		19	-	-
Total		467	291	17901

Notes: the horizontal accuracy in meter denoted by the number inside the parenthesis.

Besides displacement measurements, the Bartlett and Youd (1992) database includes other data that depict site characteristics such as the ground geometry, thickness of liquefiable soil deposits, average fine content and average mean grain size. The geotechnical properties at a site with displacements measurements were derived from available geotechnical boreholes adjacent to that site.

Figure 2.2 illustrates an algorithm that was used by Bartlett and Youd (1992) to estimate the geotechnical parameters at a site from a few available boreholes. One identifies up to four nearby boreholes, each of which has a known value X_i of a selected soil parameter X . The parameter at the site of interest, i.e., \hat{X} , is estimated by averaging X_i weighted by a corresponding distance from the site, i.e., d_i . As addressed in Bardet et al. (1999), due to the scarceness of available data, some estimates based on that algorithm are unreliable since they are resulted from boreholes more than 400 m from the site. The approximation of soil properties at the site of interest can be improved by either introducing more borehole data close to the site or utilizing more advanced algorithms of interpolation, for instance, geo-statistical methods (e.g., the Kriging method), which is illustrated later in Chapter 5.

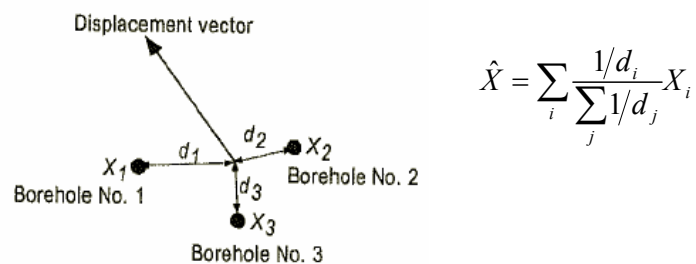


Figure 2.2 Algorithm for average (courtesy of Bardet et al. 2002)

2.3.2. Rauch (1997) Database

Rauch (1997) extended the Bartlett and Youd (1992) database by adding additional data collected from 6 more earthquakes. In contrast to the previous database that considers

individual displacement vectors and average soil properties at the vector locations, the Rauch (1997) database groups those individual displacement vectors, delineates liquefaction-induced slides and averages soil properties within those slides. This database consists of 78 slides, and 1385 displacement vectors. As addressed in Bardet et al. (1999), the delineation of slides becomes difficult and subjective when the displacement vectors are scarce and small in the amplitude.

2.3.3. USC Database (Bardet et al. 1999)

The USC database was first documented by Bardet et al. (1999). It continuously grows with data that aggregate after a few recent earthquakes, such as the 1999 Kocaeli, Turkey, earthquake.

As shown in Table 2.1, this database nowadays contains 17,901 displacement measurements. Figure 2.3 compares the USC database with the previous database compiled by Bartlett and Youd (1992). The number of case histories included in the USC database is about 40 times larger than the previous one. In particular, the USC database contains many more case histories with measured displacements smaller than 2 meters.

The USC database was compiled into a relational DBMS (Database Management System) using Microsoft Access. It includes two sub-databases: LIDD (Liquefaction-Induced ground Deformation Database) and BOD (BOrehole Database). BOD includes geotechnical investigation results derived from two types of geotechnical boreholes: Standard Penetration Test (SPT), and Cone Penetration Test (CPT). Table 2.2

summarizes recent conditions of the USC database. The data dictionary and data structure were documented in detail and well-explained in Hu (2003).

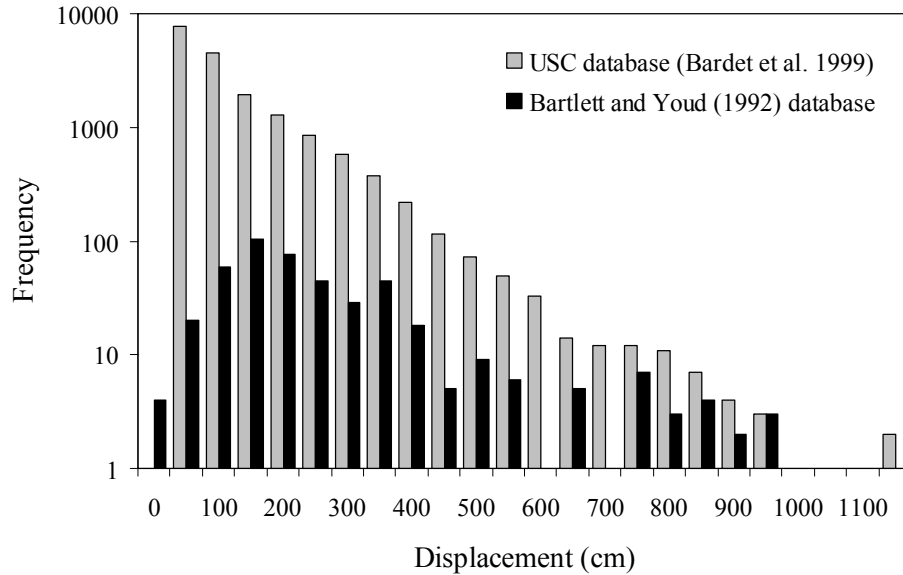


Figure 2.3 Comparison between Bartlett and Youd (1992) database and USC database

Table 2.2 Summary of the USC database (Bardet et al. 1999; Hu 2003)

Earthquake	SPT #	CPT #	Horizontal displacement			Vertical displacement		
			Range (cm)	Acc* (m)	Acc** (m)	Range (cm)	Acc* (m)	Acc** (m)
1964 Niigata	645	-	2.2-1131	-	-	-378 - 262	-	-
1983 Nihonkai-Chubu	71	-	1-565	-	-	-138 - 110	-	-
1971 San Fernando	250	230	2-385	-	-	-267 - 187	-	-
1994 Northridge	4002	-	1-120	±0.330	±0.197	-101 - 167	±0.392	±0.326
1995 Great Hanshin	97	167	0.3-671	±0.330	±0.140	-590 - 745	±0.530	-
1999 Kocaeli	97	167	9-778	-	-	-545-1289	-	-

* accuracy of absolute ground displacements; ** accuracy of relative ground displacements

Figure 2.4 shows a sample site that has been currently included in the USC database. This site experienced two earthquakes in the past, the 1974 San Fernando earthquake and the

1994 Northridge earthquake. Although the two earthquakes have similar intensity, the displacement amplitudes vary a bit. The maximum lateral displacement caused by earthquakes was reported 3.85 meter in the 1971 quake, and 1.2 meter in the 1994 quake. Reasons causing this variation remain uncertain (Davis 2007). As shown in Figure 2.4, the displacement data, which has been exported from LIDD, is represented as displacement vectors overlaying on a geology map using a GIS (Geographic Information System) platform.

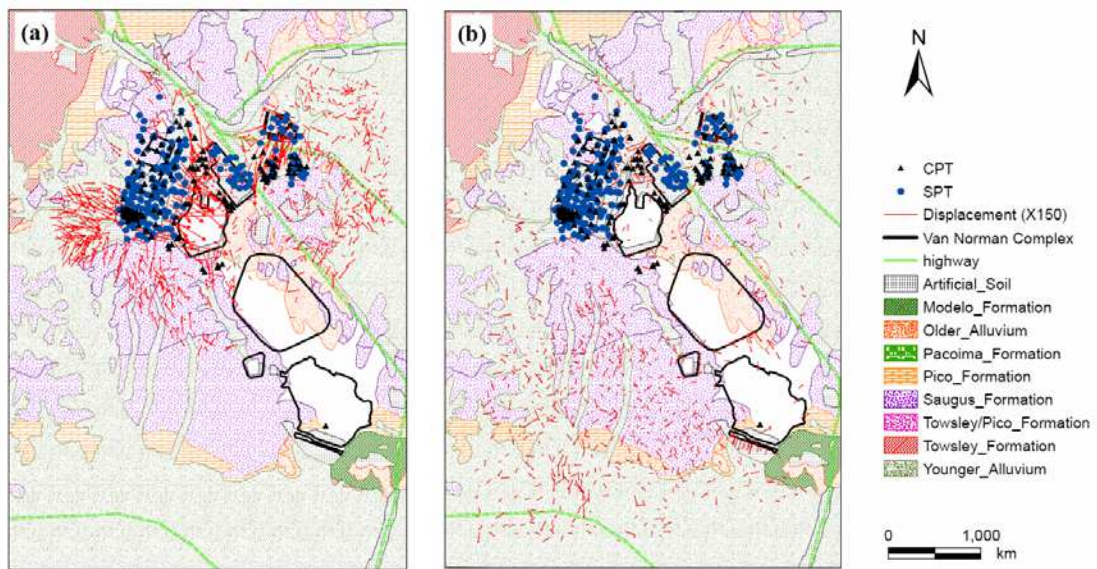


Figure 2.4 A sample site deformed during: (a) the 1971 quake; and (b) the 1994 quake

2.4. Simplified Procedure for Predicting Liquefaction Occurrence

One of the fundamental questions associated with liquefaction evaluation is whether a soil liquefies during a given earthquake. Simplified procedures have been derived from

case histories of liquefaction and they are commonly used in the practice of geotechnical earthquake engineering.

2.4.1. Generic Methodology

In general, those procedures derived from case histories of liquefaction compare two variables: the seismic demand and the capacity against liquefaction (see Kramer 1996). The seismic demand is to characterize a seismic loading imparted to soil deposits, whereas the capacity is the minimum demand required to trigger liquefaction. Eventually, the likelihood of liquefaction occurrence is inferred by a value of the factor of safety, which is defined as a ratio of the capacity to the demand.

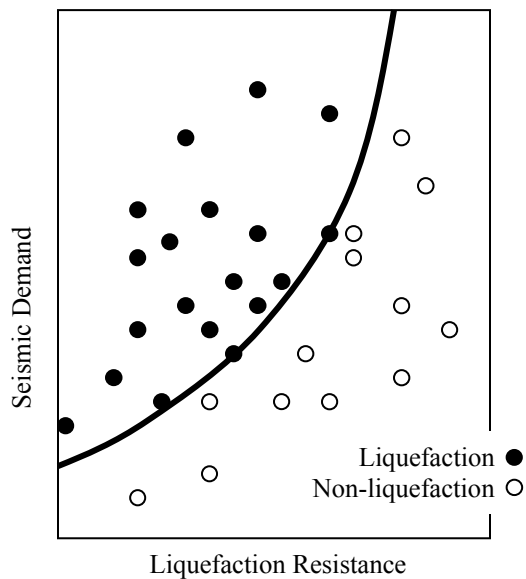


Figure 2.5 Capacity against liquefaction derived from case histories (modified from Kramer 1996)

Distinct selections of the seismic demand classify those procedures into stress-based models, strain-based models, and energy-based models. Regardless of various choices for the earthquake demand, the same procedure remains applicable in developing the capacity against liquefaction from available case histories. As shown in Figure 2.5, those collected case histories are first divided into two categories: liquefaction and non-liquefaction; the earthquake demand for each individual case is plotted against a selected parameter that correlates the resistance against liquefaction. Sufficient case histories likely form a boundary (or transition zone) between liquefaction and non-liquefaction cases. This boundary provides a lower bound of the seismic demand that triggers liquefaction in a given soil stratum. This lower bound in fact denotes the capacity against liquefaction.

2.4.2. Stress-Based Models

Originated in 1971 (Seed and Idriss), the stress-based procedure was accomplished later through a few landmark papers (Seed 1979; Seed and Idriss 1982; Seed et al. 1985). It has evolved over years and led to a comprehensive review paper by Youd et al. (2001) that summarizes the most recent revisions and improvements.

2.4.2.1. Seismic Demand

The seismic demand on a soil layer is expressed in terms of the Cyclic Stress Ratio (*CSR*). Therefore, this procedure is termed as the stress-based model. Irregular earthquake motions are converted to a number of motion cycles with uniform amplitude of 65% peak acceleration based on the assumption that both motions contribute identically to excess

pore pressure buildups. For level ground or gently sloping ground, *CSR* can be expressed as follows:

$$CSR = 0.65 \frac{a_{\max}}{g} \frac{\sigma_{v0}}{\sigma'_{v0}} r_d \quad (2.1)$$

where a_{\max} is the Peak Ground Acceleration (PGA); g is the acceleration of gravity; σ_{v0} and σ'_{v0} is total and effective vertical overburden stresses before earthquakes, respectively; and r_d is stress reduction coefficient accounting for flexibility of the soil profile. As suggested in Youd et al. (2001), for routine practice and non-critical projects, the average values of r_d can be approximated using the following equations (Liao and Whitman 1986) :

$$r_d = \begin{cases} 1.0 - 0.00765z & \text{for } z \leq 9.15m \\ 1.174 - 0.0267z & \text{for } 9.15m < z \leq 23m \end{cases} \quad (2.2)$$

where z is the depth below ground surface in meter.

2.4.2.2. Liquefaction Resistance Based on SPT

The capacity used in stress-based models, termed as the Cyclic stress Ratio Required to induce liquefaction (*CRR*), can be correlated with the SPT *N*-value, which is defined as blow counts required to drive a SPT sample down into soils for one foot. The correlation is usually derived for a standard earthquake with moment magnitude M_w of 7.5, and then scaled to other circumstance using a magnitude scaling factor (*MSF*). Figure 2.6 shows

the curves of $CRR_{7.5}$ (i.e., CRR corresponding to $M_w=7.5$ earthquakes) corresponding to different values of fine content. The x-axis uses N_{160} , known as the standard value of SPT blow counts after correction of driving energies, overburden stresses, sampling methods, rod lengths, and borehole sizes. The detailed procedure for the corrections can be found in Martin et al. (1999).

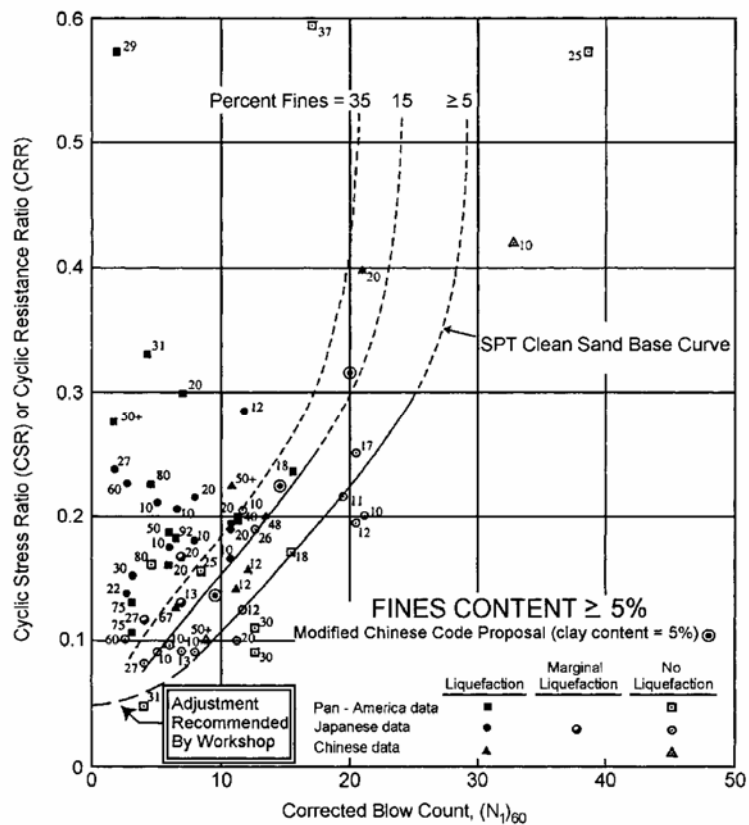


Figure 2.6 Liquefaction resistance based on SPT results (courtesy of Youd et al. 2001)

Finally, a factor of safety against liquefaction, i.e., FS_{Liq} , can be computed from the ratio of $CRR_{7.5}$ and CSR using the following equation:

$$FS_{Liq} = \frac{CRR_{7.5}}{CSR} MSF \quad (2.3)$$

2.4.2.3. Liquefaction-Resistance Based on CPT

CPT tests are receiving gradual appreciation in practice because of their ability to produce continuous measurements and their high performance in data repeatability. The CPT-based procedure becomes a supplemental method to the SPT-based method for evaluating liquefaction potential (e.g., Robertson and Wride 1998).

Robertson and Wride (1998) used Figure 2.7 to estimate $CRR_{7.5}$ of clean sands (i.e., fine content < 5%) from CPT results.

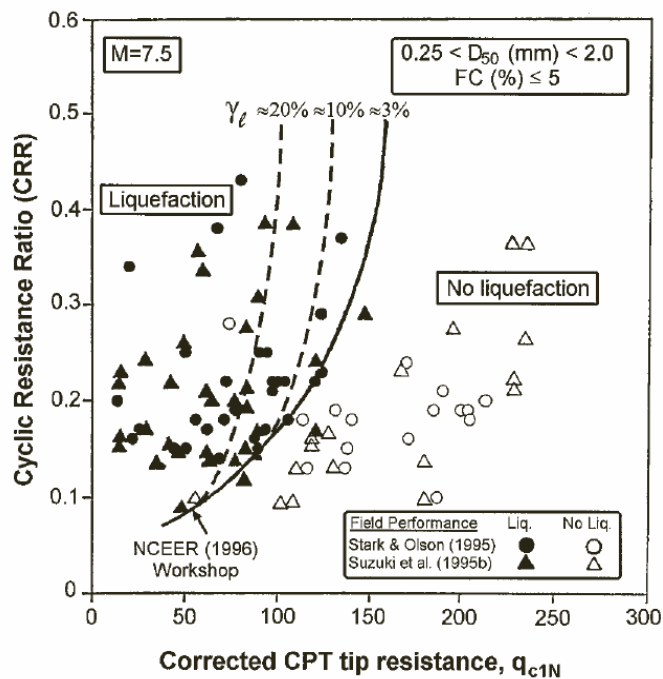


Figure 2.7 Liquefaction resistance based on CPT results (courtesy of Robertson and Wride 1998)

The clean-sand base curve in Figure 2.7 can be approximated by the following equations:

$$CRR_{7.5} = \begin{cases} 0.833 q_{c1N,cs}/1000 + 0.05 & \text{for } q_{c1N,cs} < 50 \\ 93(q_{c1N,cs}/1000)^3 + 0.08 & \text{for } 50 \leq q_{c1N,cs} < 160 \end{cases} \quad (2.4)$$

where $q_{c1N,cs}$ is the clean-sand cone penetration resistance normalized to one atmospheric pressure (i.e., approximately 100 kPa). It can be calculated from:

$$q_{c1N,cs} = K_c q_{c1N} \quad (2.5)$$

where q_{c1N} , the normalized cone penetration resistance can be calculated from:

$$q_{c1N} = C_Q (q_c/P_a) = (P_a/\sigma'_{vo})^n (q_c/P_a) \quad (2.6)$$

where P_a is one atmospheric pressure; q_c is the field cone penetration; n is exponent that varies with soil type, $n = 1.0$ for clays, $n = 0.5$ for clean sands, and $0.5 < n < 1.0$ for silts and sandy silts. n may be determined from the soil behavior index I_c that is defined by following equation:

$$I_c = \left[(3.47 - \log Q)^2 + (1.22 + \log F)^2 \right]^{0.5} \quad (2.7)$$

where

$$Q = \left[(q_c - \sigma_{vo})/P_a \right] \left[(P_a/\sigma'_{vo})^n \right] \quad (2.8)$$

and

$$F = f_s / (q_c - \sigma_{vo}) \times 100\% \quad (2.9)$$

where f_s is the sleeve friction measured in the field. The correction factor K_c in equation (2.5) accounts for grain characteristics. It is defined by the following equations:

$$K_c = \begin{cases} 1.0 & \text{for } I_c \leq 1.64 \\ -0.403I_c^4 + 5.581I_c^3 - 21.63I_c^2 + 33.75I_c - 17.88 & \text{for } I_c > 1.64 \end{cases} \quad (2.10)$$

2.4.2.4. Correlation between SPT N-Value and CPT Cone Resistance

The correlation between SPT N -value and CPT cone resistance sometimes is necessary when SPT tests are not available but preferred in a computation leading to liquefaction evaluation. One of the well-known correlations was developed by Robertson et al. (1983). Anagnostopoulos et al (2003) slightly modified this correlation and proposed an explicit expression as follows:

$$N_{60} = 0.13084 (q_c / P_a) (D_{50})^{-0.26} \quad (2.11)$$

where D_{50} is the mean grain size in mm, which can be computed from the correlation derived from CPT penetration. For example, D_{50} can be approximated using Anagnostopoulos et al (2003) correlation for mechanical cones that states as follows::

$$\lg(D_{50}) = (1.45 - R_f) / 1.36 \quad (2.12)$$

where R_f is the friction ratio defined as the ratio f_s/q_c .

In addition, Jefferies and Davies (1993) proposed an alternative correlation between SPT N -value and CPT penetration:

$$N_{60} = \frac{q_c/P_a}{8.5 \left(1 - \frac{I_c}{4.75}\right)} \quad \text{for } I_c < 4.75 \quad (2.13)$$

Bennert et al (2002) experimentally compared Robertson et al. (1983) and Jefferies and Davies (1993). They concluded that both methods provided N -values that compared favorably to the actual results; however, the second method was consistently more accurate than the first one.

2.4.3. Energy-Based Models

Besides stress-based procedures, energy-based models are receiving increasing attentions in the research field. They compensate stress-based models by considering the combined influences of the duration of cyclic shear motions together with the amplitude (Kayen and Mitchell 1997). Instead of using CSR , Arias Intensity is used to characterize the seismic demand in energy-based models. Different from Equation (2.3), FS_{Liq} is computed from the following equation:

$$FS_{Liq} = I_{hb}/I_h \quad (2.14)$$

where I_h is the horizontal component of Arias Intensity; I_{hb} is the minimum Arias Intensity to trigger liquefaction. Kayen and Mitchell (1997) suggested Figure 2.8 for estimating the values of I_{hb} from either SPT or CPT test results. Green (2001) reviewed many more energy-based procedures.

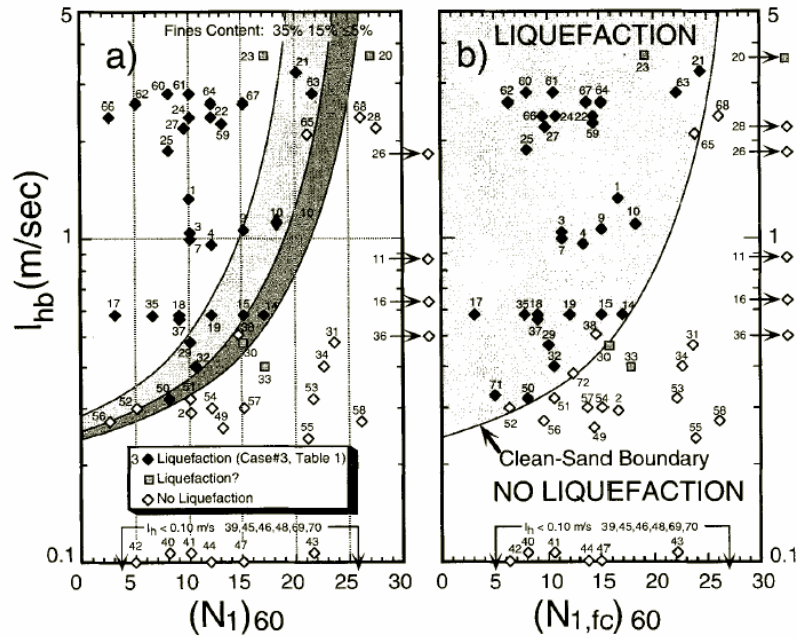


Figure 2.8 Energy-based procedures based on (a) SPT N-value; and (b) CPT penetration (courtesy of Kayen and Mitchell 1997)

2.5. Liquefaction Potential Index

Iwasaki et al (1978) extended the evaluation of liquefaction occurrence at a single depth to the evaluation of liquefaction severity over a soil profile. Iwasaki et al. (1978) defined the liquefaction Potential Index (*LPI*) as follows:

$$LPI = \int_0^{20} F(z)w(z)dz \quad (2.15)$$

where z is the depth in meter below the ground surface, $0 < z < 20$ m; the depth weighting factor $w(z)=10 - 0.5 z$; and

$$F(z) = \begin{cases} 1 - FS_{Liq} & \text{for } FS_{Liq} \leq 1 \\ 0 & \text{for } FS_{Liq} > 1 \end{cases} \quad (2.16)$$

Sonmez (2003) revised Equation (2.15) by considering the threshold value of 1.2 between the non-liquefiable and marginally liquefied categories. He proposed:

$$F(z) = \begin{cases} 1 - FS_{Liq} & \text{for } FS_{Liq} < 0.95 \\ 2 \times 10^6 e^{-18.427 FS_{Liq}} & \text{for } 0.95 \leq FS_{Liq} < 1.2 \\ 0 & \text{for } FS_{Liq} \geq 1.2 \end{cases} \quad (2.17)$$

Table 2.3 provides two classification categories developed by Iwasaki et al (1978) and Sonmez (2003), respectively. Both of them are commonly used in practice for mapping liquefaction severity over large areas.

Table 2.3 Liquefaction severity categories based on *LPI*

Liquefaction Potential Index (<i>LPI</i>)	Liquefaction potential (Iwasaki et al. 1982)	Liquefaction potential (Sonmez 2003)
0	Very Low	Non-liquefiable
$0 < LP \leq 2$	Low	Low
$2 < LPI \leq 5$	High	Moderate
$5 < LPI \leq 15$	Very High	High
$LPI > 15$	Very High	Very High

2.6. Models for Liquefaction-Induced Lateral Ground Deformation

2.6.1. Empirical Formulations Derived from Sliding Block Analogy

Newmark (1965) originally proposed a sliding block model for calculating seismic deformations of slopes subjected to earthquakes. This approach is widely applied in practice to estimate the seismic permanent displacements in dams, embankments and landslides. As illustrated in Figure 2.9 (a), a slope is modeled as a rigid mass m resting on a frictional plane with a slope angle θ subjected to a seismic excitation a_{eq} .

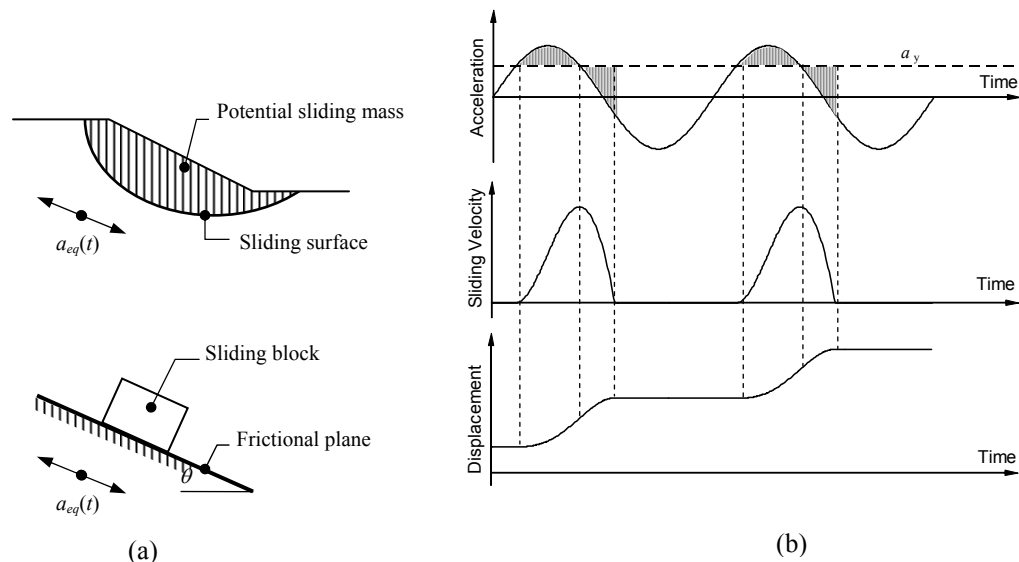


Figure 2.9 Newmark sliding theory: (a) block analogy (after Newmark 1965); and (b) double integration approach (after Wilson and Keefer 1983)

The resistance against sliding along the frictional plan is characterized by the yield acceleration a_y , which is defined as the minimum acceleration in the downslope direction required to overcome the shear resistance against sliding:

$$a_y = (F_s - 1)g \sin \theta \quad (2.18)$$

where F_s is the static factor of safety computed from static slope stability analysis. Usually $F_s > 1$, otherwise, the Newmark sliding analysis becomes inapplicable because of negative yield acceleration.

In the Newmark approach, the block slips only if ground accelerations exceed the yield value. The final displacement of the sliding mass results from the accumulation of displacements each time it slips. Figure 2.9 (b) illustrates the double integration for numerical computation of cumulative displacements (Wilson and Keefer 1983). For a particular earthquake, the cumulative displacement is determined through integrating twice the excess ground acceleration above and below the yield values until the relative velocity vanishes.

Based on regression analysis on strong motions records, a few empirical relations were developed to relate the final displacement to a few seismic parameters that can be estimated from attenuation relationships (e.g., Ambraseys and Menu 1988; Jibson 1993; Jibson 2007; Miles and Ho 1999; Sarma 1975; Yegian et al. 1991). Those models rely on seismic parameters instead of time histories of strong motions. They are suitable for regional assessment of sliding hazards (Jibson et al. 2000). Some of them were reviewed in literatures (e.g., Cai and Bathurst 1996; Miles and Keefer 2000).

The conventional Newmark seismic deformation analysis relies on five assumptions: (1) slip surface behaves rigid - perfectly plastic; (2) dynamic response is simplified; (3) vertical acceleration does not influence motion; (4) sliding mass moves only downward; and (5) shear strength is constant.

Many researchers relaxed these assumptions and developed modified Newmark procedures. Instead of a single rigid block, compliant multiple-block systems were used in either decoupled (e.g., Lin and Whitman 1983; Makdisi and Seed 1978) or coupled manner (e.g., Kramer and Smith 1997; Rathje and Bray 2000; Wartman and Bray 2003). Yan et al. (1996), Matasovic et al. (1998) and Ingles et al. (2006) considered two-way sliding with vertical and horizontal accelerations simultaneously. They concluded that upslope movements and vertical ground motions had negligible contributions to permanent seismic deformations. In addition, Kramer and Lindwall (2004) also investigated effects of two- and three-dimensional ground motions on displacements of sliding mass. They concluded that computed displacements were very sensitive on azimuthal direction of the input motions.

Several adaptations of the Newmark procedure have relaxed the assumption of constant yield acceleration (i.e., constant residual shear strength). According to Martin (2000), the assessment of post-liquefaction residual shear resistance is critical for calculating liquefaction-induced displacements. Martin (2000) showed that the residual shear strength, calculated from undrained laboratory tests, may yield non-conservative results, and recommended instead to evaluate it from case histories. Yegian et al (1995) looked

into linearly decaying yield acceleration associated with progressive liquefaction. Before liquefaction, the yield acceleration was estimated from drained shear strength, whereas the post-liquefaction value of shear strength was back-calculated from pseudo-Newmark sliding analysis based on observed displacements. Biondi et al (2002) derived the yield acceleration as a function of the time history of pore pressure buildups. However, all those methods applies only to slops that undergo moderate reduction in shear strength but remain statically stable (i.e., $F_s \geq 1$), and they do not cover unstable cases (i.e., $F_s < 1$).

2.6.2. Regression Models Based on Case Histories

Based on available case histories of liquefaction-induced lateral ground deformations, a few empirical models were developed from statistical analyses without considering the physical mechanism of liquefaction-related deformations.

Table 2.4 lists some of those empirical models developed since 1980s. They were reviewed in literatures (e.g., Bardet 2003; Rauch 1997). Except Hamada et al. (1986) model and Youd and Perkins (1987) model, other models benefit from the Bartlett and Youd (1992) database.

The performances of empirical models depend on data quality of collected case histories. Rauch (1997) addressed that data biasness could be a problematic issue for those existing models listed in Table 2.4. As shown in Table 2.1, 72% of data in the Barlett and Youd (1992) database were collected from Japan after the 1964 Niigata earthquake and the

1983 Noshiro earthquake. However, models resulted from this database were claimed to be globally applicable.

Table 2.4 Parameters of empirical models for liquefaction-induced lateral displacement

Models	Parameters	M_w	R	H	S	W	T_{15}	F_{15}	D_{5015}	LDI	a_{max}	T_d	L_{slide}	S_{top}	H_{face}	Z_{FSmin}	Z_{liq}
Hamada et al. (1986)				<input checked="" type="checkbox"/>	<input checked="" type="checkbox"/>												
Youd and Perkins (1987)		<input checked="" type="checkbox"/>	<input checked="" type="checkbox"/>														
Bartlett & Youd (1995); Youd et al. (2002)		<input checked="" type="checkbox"/>	<input checked="" type="checkbox"/>		<input checked="" type="checkbox"/>												
Rauch (1997)		<input checked="" type="checkbox"/>	<input checked="" type="checkbox"/>								<input checked="" type="checkbox"/>						
Bardet et al. (2002)		<input checked="" type="checkbox"/>	<input checked="" type="checkbox"/>		<input checked="" type="checkbox"/>	<input checked="" type="checkbox"/>	<input checked="" type="checkbox"/>										
Zhang et al. (2004)					<input checked="" type="checkbox"/>	<input checked="" type="checkbox"/>				<input checked="" type="checkbox"/>							
Definitions:																	
M_w	Moment magnitude of earthquake																
R	Epicentral distance (km)																
S	Slope (%) of ground surface																
H	Thickness (m) of liquefied soil																
W	Free-face ratio (%)																
T_{15}	Thickness (m) of saturated cohesionless soils (excluding depth > 20m and > 15% clay content) with $N_{160} < 15$																
F_{15}	Average fine content (% finer than 75 μ m)																
D_{5015}	Average D_{50} grain size (mm) in T_{15}																
LDI	Lateral displacement index																
a_{max}	Peak horizontal acceleration (g) at ground surface of site																
T_d	Duration of strong earthquake motions at site (surface acceleration ≥ 0.05 g)																
L_{slide}	Maximum horizontal length (m) from head to toe of lateral spread																
S_{top}	Average slope (%) across surface of lateral spread																
H_{face}	Height (m) of free face, measured vertically from toe to crest of free face																
Z_{FSmin}	Average depth (m) to minimum factor of safety in potentially liquefiable soil																
Z_{liq}	Average depth (m) to top of liquefied soil.																

One of the challenges in constituting empirical methods lies in the determination of controlling parameters. Table 2.4 lists some parameters used in the past. They can be grouped into three categories: (1) geometric parameters; (2) seismic parameters; and (3) soil parameters. The slope of ground surface S , and the free-face ratio W are commonly

used variables to characterize the topographical setting of a given site. The moment magnitude of earthquakes M_w and the seismic source distance R are often employed for describing the seismic contributions. R may differ slightly from model to model, and its precise definition should be found in the original publications. Soil parameters adopted in the existing models include liquefiable thickness H , T_{15} , fine content F_{15} , and mean grain size $D_{50_{15}}$. Once a set of dominant parameters is determined, a functional form of displacement is postulated and then calibrated using regression analyses on available case histories. For instance, Bartlett and Youd (1995) assumed a logarithmic-linear-like relation, and used a Multiple Linear Regression (MLR) analysis to obtain values of coefficients. This model received a recent revision (Youd et al. 2002). The current formulation of this model computes lateral deformations for two cases:

In free-face conditions,

$$\begin{aligned} \log D = & -16.713 + 1.532M_w - 1.406 \log R^* - 0.012R + 0.592 \log W \\ & + 0.540 \log T_{15} + 3.413 \log(100 - F_{15}) - 0.795 \log(D_{50_{15}} + 0.1mm) \end{aligned} \quad (2.19)$$

In gently sloping ground conditions

$$\begin{aligned} \log D = & -16.213 + 1.532M_w - 1.406 \log R^* - 0.012R + 0.338 \log S \\ & + 0.540 \log T_{15} + 3.413 \log(100 - F_{15}) - 0.795 \log(D_{50_{15}} + 0.1mm) \end{aligned} \quad (2.20)$$

where D is the estimated lateral ground displacement in meter; W in %; T_{15} in meter; F_{15} in %; $D_{50_{15}}$ in mm; and R^* is defined as:

$$R^* = R + 10^{0.89M_w - 5.64} \quad (2.21)$$

Following the approach of Bartlett and Youd (1995), Bardet et al (2002) proposed a revised model with fewer parameters and comparable performance. They excluded two parameters of soil properties, i.e., $D_{50/15}$ and F_{15} , which are difficult to be reconstituted from the soil reports. This revised model states the estimated lateral deformations as follows:

In free-face conditions,

$$\log(D + 0.01) = -7.280 + 1.017M_w - 0.278 \log R - 0.026R + 0.497 \log W + 0.558 \log T_{15} \quad (2.22)$$

In gently sloping ground conditions:

$$\log(D + 0.01) = -6.815 + 1.017M_w - 0.278 \log R - 0.026R + 0.454 \log S + 0.558 \log T_{15} \quad (2.23)$$

Bardet et al. (2002) repeated the MLR analysis only for case histories with displacement less than 2 meters, and proposed another formulation for data set with $D < 2$ meters:

In free-face conditions,

$$\log(D + 0.01) = -6.909 + 1.001M_w - 0.289 \log R - 0.021R + 0.090 \log W + 0.289 \log T_{15} \quad (2.24)$$

In gently sloping ground conditions,

$$\log(D + 0.01) = -6.747 + 1.001M_w - 0.289 \log R - 0.021R + 0.203 \log S + 0.289 \log T_{15} \quad (2.25)$$

Bardet et al. model (2002) is favorable in practice because it requires less effort in estimating input parameters.

A premise of MLR models is to assume logarithmic relations between displacements and model parameters. This assumption may deviate from the actual physical mechanism of liquefaction-related deformations. In order to integrate correct mechanism into empirical

models, Zhang et al. (2004) developed a semi-empirical model using the maximum shear strain γ_{\max} that is identified from laboratory tests to be a significant factor to lateral displacements. Zhang et al. (2004) defined lateral displacement index (*LDI*) using the following equation:

$$LDI = \int_0^{z_{\max}} \gamma_{\max} dz \quad (2.26)$$

where z_{\max} is the maximum depth up to 23 m below all the potential liquefiable layers with a calculated $FS_{Liq} < 2$; γ_{\max} depends on FS_{Liq} and the relative density of granular soils D_r ; and FS_{Liq} can be computed using the procedures that have been reviewed in section 2.4. Zhang et al. (2004) then derived the lateral displacements as follows:

In free-face conditions,

$$D = 6W^{-0.8} \cdot LDI \quad \text{for } 4 < W < 40 \quad (2.27)$$

In gently sloping ground conditions,

$$D = (S + 0.2) \cdot LDI \quad \text{for } 0.2\% < S < 3.5\% \quad (2.28)$$

This model has advantages in integrating liquefaction potential assessment into the process of displacement predictions.

2.7. Summary

In summary, we have less knowledge in precisely predicting liquefaction-induced deformations than in evaluating liquefaction potential. Existing empirical models for

liquefaction-induced lateral ground deformations were developed from databases including a few hundred measurements (e.g., Bartlett and Youd 1992). They were derived from regression analyses and corroborated little physical mechanism. With the advances in modern survey techniques, available case histories are growing rapidly. They have large potential to improve current procedures for deformation prediction, and enable the next generation of models that corroborate more physical mechanism of liquefaction-induced lateral ground deformations. The first step towards the application of those case histories is to establish a data management system using new information technologies that handles effectively numerous data in order to maximize the data value.

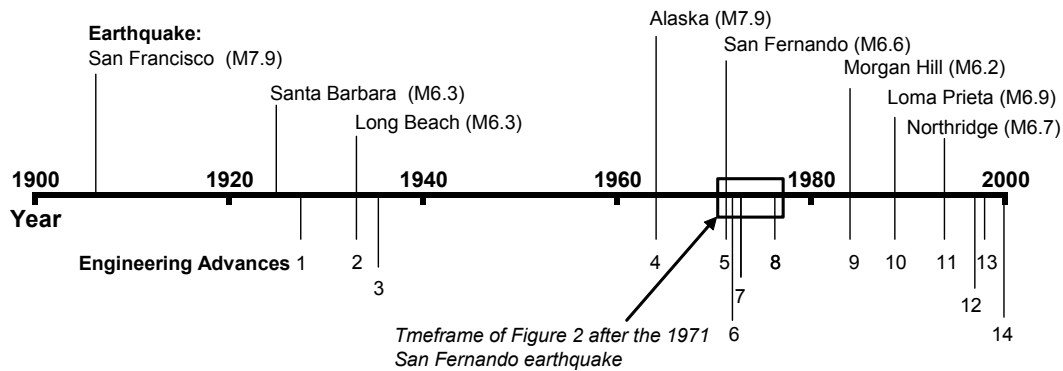
Chapter 3. Information Management for Post-Earthquake Reconnaissance

This chapter illustrates the significance of Post-Earthquake Reconnaissance (PER), reviews the information techniques applied in this field, and presents the work related to releasing PER information on the Internet. The primary purpose of this chapter is to provide basic guideline on how to use recent information technologies for efficiently documenting PER information and automating Web PER reports. The original contributions by the author include: (1) a database-driven Web application for distributing PER information, and (2) the first application of embedded metadata in archiving and releasing PER information on the Internet.

3.1. PER and Earthquake Engineering

Earthquake engineering continuously evolves from information collected after major earthquakes. It leaps forward each time post-earthquake investigations yield observations unexplainable by our current knowledge. As shown in Figure 3.1, revisions to the practice of earthquake engineering in the United States generally follow major earthquakes. For instance, after the 1971 San Fernando earthquake, numerous findings on surface faulting, and damages to hospitals, bridges and dams prompted: (1) the Alquist-Priolo Earthquake Fault Zonation Act in California that forbids housing construction across active faults; (2) new design codes for bridges and hospitals; and (3)

implementation of seismically resistant design for earth dams. After the 1994 Northridge earthquake, extensive observations on cracks in steel structures prompted further upgrades to California building codes of seismic safety, and caused substantial changes in building codes for wood-frame and steel-frame buildings. Rapid developments after destructive earthquakes are not unique to the United States, but are also applied to other seismically active regions such as Japan and Turkey (Sezen et al. 2000; Whittaker et al. 1998).



No.	Major events advancing earthquake engineering
1	Provisions for seismic design included in UBC.
2	First substantive seismic design provisions.
3	Zoning map of equal seismic probability included in UBC.
4	First zoning and land use regulations related to seismic hazards.
5	New bridge design code and new requirements for ductile seismic detailing of reinforced concrete hospitals.
6	The Alquist-Priolo Earthquake Fault Zone Act passed
7	First comprehensive seismic design document ATC 003 based on modern dynamic analysis principles.
8	Geotechnical site factors incorporated into UBC; First national seismic hazard maps proposed.
9	Reduced flexibility of large-span roof in UBC.
10	Recommendations upgraded for open first stories and wharf; Soil factors refined in building codes; Seismic Hazards Mapping Act passed in California that involves mitigation of liquefaction and landslides.
11	Code changed on wood-frame buildings; Recommendations upgraded and new code provisions for tilt-up concrete panel buildings; Soil condition included in the design control factors in NEHRP's Provisions.
12	The Seismic Harzard Mapping Act passed
13	First set of comprehensive guidelines for seismic design that incorporate principles of performance of performance-based seismic design: NEHRP Guidelines for Seismic Rehabilitation of Buildings (FEMA 273).
14	NEHRP requirements adopted by the IBC 2000. Seismic requirements determined by a combination of soil condition and building usage.

ATC - Applied Technology Council; IBC - International Building Code;
 UBC - Uniform Building Code; FEMA - Federal Emergency Management Agency;
 NEHRP - National Earthquake Hazards Reduction Program

Figure 3.1 Advances in earthquake engineering after major earthquakes

Field investigations after earthquakes can take place from hours to years (e.g., Holzer et al. 2003). A window shown in Figure 3.1 indicates the time interval of those investigations following the occurrence of the 1971 San Fernando earthquake. The activity details within that time window are illustrated in Figure 3.2. The term PER is referred to as those activities that take place within weeks after an earthquake, i.e., the shaded time window in Figure 3.2. PER is conducted in a timely manner after earthquakes in order to collect as much as possible time-sensitive data before substantial alterations caused by reconstructions. PER findings often stimulate long-term researches that lead to advances in earthquake engineering.

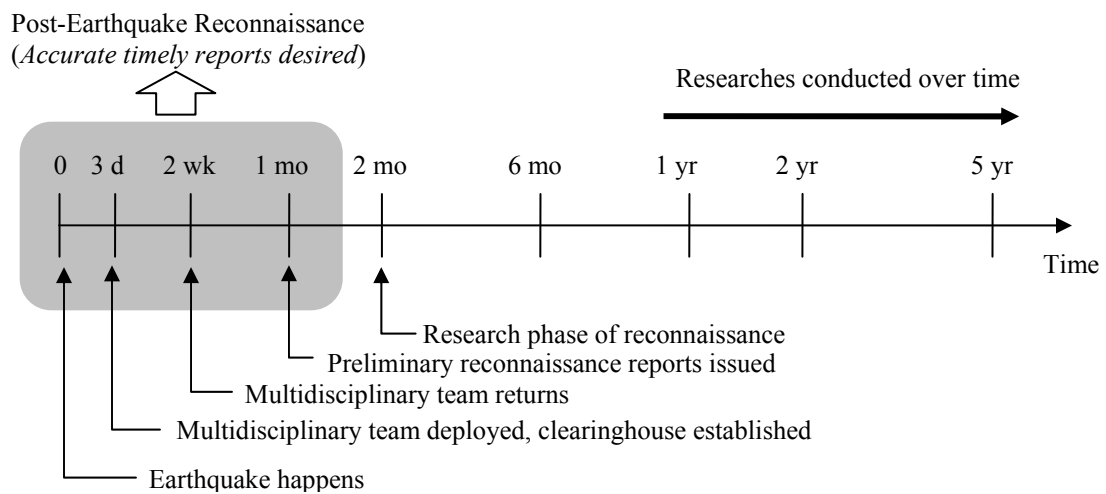


Figure 3.2 Timeframe of field investigations after major earthquakes (After Holzer et al. 2003, modified from LFE)

Figure 3.3 illustrates activity details within the PER time window (see Figure 3.2) using PER projects that were sponsored by the National Science Foundation (NSF). Once a

damaging earthquake happened, a few researchers discussed with NSF program managers on whether PER was warranted based on information available from news media and local researchers in the earthquake-impacted areas. After reaching a decision to proceed, a small team was sent to scout the field. The team members collected damage data, and identified areas that required further investigations by additional personnel. Those PER activities concluded with a collection of data that would be later integrated into a GIS (Geographic Information System) model. The compiled data were disseminated to the public or research institutes on the Internet in terms of Web reports, technical briefings and newsletters. Depending on the significance of PER findings, NSF requested proposals that prompted long-term researches.

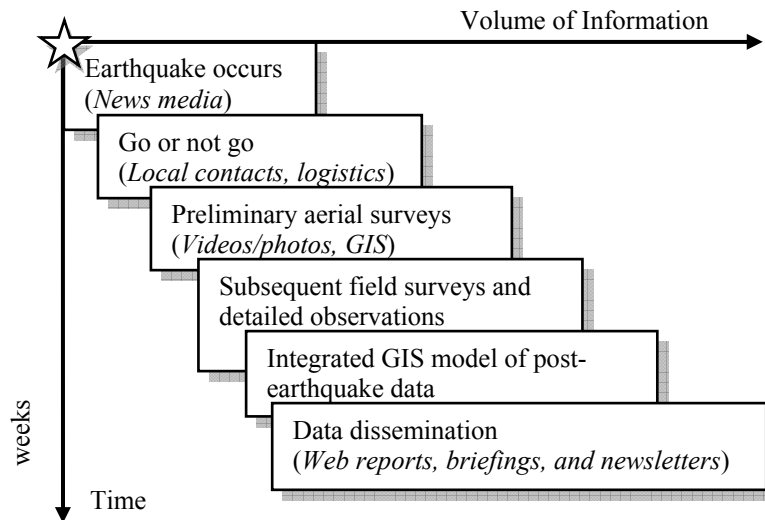


Figure 3.3 Sequence of major events in NSF-sponsored PER

Many professional organizations are participating in the collection and dissemination of PER information. Table 3.1 partially lists a few of them. Geotechnical Earthquake Engineering Server (GEES, <http://gees.usc.edu>) at the University of Southern California is one of the early websites to release PER information. It developed a Web-based data central for PER with emphasis on geotechnical issues. Geo-Engineering Earthquake Reconnaissance (GEER, <http://gees.usc.edu/GEER>) Association also serves as a platform to document PER in geotechnical aspect. Multidisciplinary Center for Earthquake Engineering Research (MCEER, <http://mceer.buffalo.edu/>) promotes novel technologies that facilitate PER activities. It published PER reports based on preliminary surveys aided by new devices (e.g., Adams et al. 2005). The National Information Service for Earthquake Engineering (NISEE, <http://nisee.berkeley.edu>) maintains Earthquake Image Information (EQII) system that contains approximately thousands of digital images from over 200 earthquakes. Earthquake Engineering Research Institute (EERI, <http://www.eeri.org>) developed the Program of Learning from Earthquake (LFE, <http://www.eeri.org/lfe.html>), and launched a virtual clearinghouse for centralizing PER data. In addition to those websites above, a few websites are designed only for a single earthquake. For instance, the Nisqually earthquake information clearinghouse (<http://www.ce.washington.edu/~nisqually>) documents information on that particular earthquake in many aspects including seismological, structural, geotechnical, lifelines, and socio-economic issues. Besides the United States, PER also extensively take place in other seismically active regions such as Japan and Turkey. Some foreign entities are listed in Table 3.1 as well.

Table 3.1 Organizations releasing PER information

Country	Organization / Website URL
USA	Multidisciplinary Center for Earthquake Engineering Research (MCEER) http://mceer.buffalo.edu/research/Reconnaissance
	Learning from Earthquake Program, Earthquake Engineering Research Institute (EERI) http://www.eeri.org/lfe.html
	Geotechnical Earthquake Engineering Server (GEES) http://gees.usc.edu/GEES
	Geo-Engineering Earthquake Reconnaissance Association (GEER) http://gees.usc.edu/GEER
	Image Information System (EQIIS) National Information Service for Earthquake Engineering (NISEE) http://nisee.berkeley.edu/eqiis.html
Japan	Structural Dynamics Laboratory (Kyoto University) http://eqgate.kuciv.kyoto-u.ac.jp
	Disaster Prevention Research Institute (Kyoto University) http://www.dpri.kyoto-u.ac.jp
	Earthquake Research Institute (University of Tokyo) http://www.eri.u-tokyo.ac.jp/
Turkey	the European Association for Earthquake Engineering (EAEE) http://www.eaee.boun.edu.tr/

As shown in Figure 3.4, the volume of PER information has exponentially increased over years since the inception of the Internet. This exponential growth of information results from an increase in the number and resolution of photos. It relates more to changes in digital cameras and web technologies than to the significance of the earthquake itself. The usage of portable digital cameras and Global Position System (GPS) units allows at-ease data collection for PER projects. Nowadays Web technologies enable an era of information explosion.

Table 3.2 lists a few PER reports archived on the GEES website since 1995. The reconnaissance after the 2008 Wenchuan, China earthquake yielded 1852 photos, much more than after the 1995 Hyogoken-Nanbu, Japan earthquake.

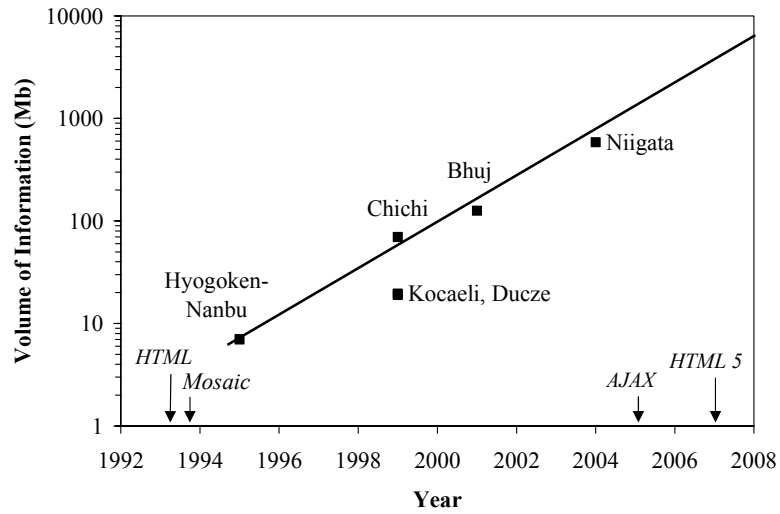


Figure 3.4 Exponential growth of information volume archived on the GEES website since the inception of the Internet

Table 3.2 PER reports released by GEES

Earthquake name	Earthquake date	Arrival date of reconnaissance team	Report release date	Number Of Photos	GIS	Volume of Information (Mb)
Hyogoken-Nanbu, Japan	01/17/95	01/27/95	02/05/95	105	No	7
Kocaeli, Turkey	08/17/99	08/24/99	09/03/99	155	Yes	19
Chichi, Taiwan	09/21/99	09/29/99	10/08/99	235	Yes	70
Dücze, Turkey	11/12/99	11/17/99	11/25/99	121	Yes	20
Bhuj, India	01/25/01	02/12/01	03/01/01	486	Yes	126
Niigata, Japan	10/23/04	10/30/04	11/04/04	497	Yes	585
Wenchuan, China	05/12/08	08/04/08	08/12/08	1852	Yes	-

To manage a large amount of information that is continuously increasing with time, we need competent information technologies. In an attempt to enhance the coordination among various organizations, Holzer et al. (2003) recommended the National Earthquake Hazard Reduction Program (NEHRP) to establish standard formats for data collection, and to archive data in a Web-based data management system. The present study

continues that effort. It aims to propose a simple and effective approach using advanced information technologies available nowadays.

3.2. Techniques Employed in PER

3.2.1. Application of GPS

A GPS unit is essential to obtain photos with spatial information, i.e., geo-referenced digital pictures.

Typically, for PER purposes, GPS units are as accurate as 6 meters. The accuracy of GPS signals can be increased up to 2 meters for receivers compatible with the Wide-Area Augmentation System (WAAS). It can be improved to 1 centimeter over short distances using the technique of Differential GPS (DGPS). Accurate positioning with GPS units depends on the way observations are made. In most cases, photographs and GPS units have practically identical positions in field surveys. However, in aerial surveys, GPS units record locations different from the actual positions of observations on the ground. To position accurately observations requires information of flight direction, altimeter of aircraft, and camera orientation, which can only be approximated roughly. Better accuracy can be obtained using alternate positioning techniques, e.g., laser range finder.

Many GPS units have a tracking system that records positions at regular intervals into GPS track logs. As shown in Figure 3.5, a track log consists of a sequence of points, each of which has a pair of coordinates, i.e., the spatial coordinate \mathbf{X}_i (e.g., longitude and

latitude) and the time t_i . Prior to recoding GPS track logs, users should estimate the anticipated duration of GPS track logs, since most GPS units have limited memory capacity. Their memory may become full if a GPS unit tracks positions all day using too short time intervals (e.g., 1 second). New GPS units offer 10,000-point tracking, which corresponds to about a 14-hours record with a five-second interval. Some GPS units may have no tracking capabilities. A few others optimize the memory storage by retaining only the points that are sufficient for re-tracing back a previous path. Another important aspect of GPS track logs is that they are often interrupted intermittently because of the poor signals of satellites reception when going through tunnels or passing high buildings. Fortunately, many GPS units record the quality of satellite reception as well as spatial coordinates and time.

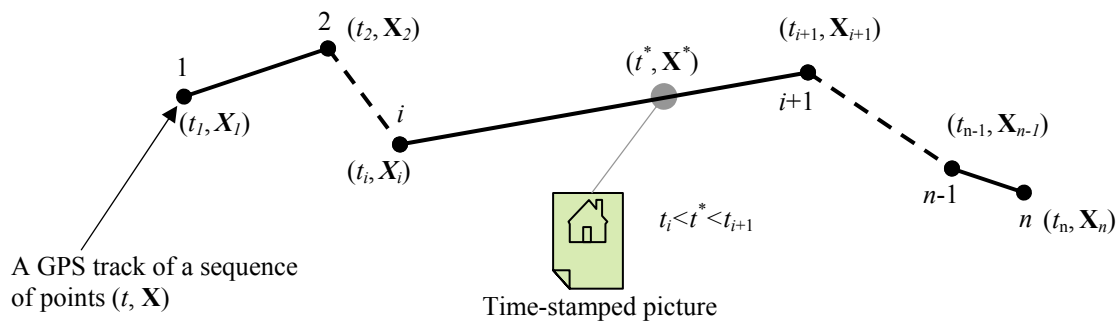


Figure 3.5 Geo-referencing a picture using its timestamp and a GPS track log

3.2.2. Geo-Referencing Photos

A digital camera with a built-in clock can be used along with a GPS unit to geo-reference pictures. The first step of geo-referencing is to synchronize the built-in clock in the camera and the GPS unit so that both of them operate in an identical time system. As a result, pictures taken by the camera will be time-stamped in accordance with the time system used by the GPS unit. Figure 3.5 illustrates the principle for geo-referencing a digital picture using a GPS track log that consists of n points. One takes the picture at time t^* , i.e., $t_i < t^* < t_{i+1}$. By screening the track log, the picture is positioned between two locations (t_i, \mathbf{X}_i) and $(t_{i+1}, \mathbf{X}_{i+1})$. By assuming that the GPS unit travels with a constant velocity between any two successive locations, the spatial coordinate of the picture \mathbf{X}^* can be determined from a linear interpolation:

$$\mathbf{X}^* = \mathbf{X}_i + \frac{\mathbf{X}_{i+1} - \mathbf{X}_i}{t_{i+1} - t_i} (t^* - t_i) \quad (3.1)$$

3.2.3. Embedding Metadata into Photos

Embedded metadata formats are available nowadays to allow embedding data about a file (i.e., metadata of files) into the file itself. Embedding metadata keeps "the truth in the file" and avoids a multitude of problems rooted from vendor-specific metadata. In the past, descriptive information about photos was supplied by a third-party image management application, and was locked into a private database only accessible by that particular application. The metadata could not travel with photos files. The separation

between the metadata and files caused inconveniency in sharing photos among multiple entities. In the contrary, embedded metadata allow easily sharing and transferring photos across products, vendors, and platforms. Because of embedded metadata formats, the metadata can be glued to photos files. If one switches archive tools, or transfers photos to another system, these alterations have little malicious impacts on photo files. A decent archiving tool, which supports embedded metadata, can even recover the metadata database from the embedded metadata.

Three embedded metadata formats are available nowadays: EXIF (Exchangeable Image File Format), IPTC (International Press Telecommunications Council), and XMP (Extensible Metadata Platform). EXIF was established in 1995. It is a specification used by most digital cameras for metadata such as time-stamps, camera settings (e.g., camera make and model, aperture, shutter speed, focal length, ISO speed etc.), and descriptive information. EXIF defines standard tags for the information of GPS locations, which allow one to amend a photograph with spatial coordinates that have been obtained from geo-referencing process as previously illustrated by Figure 3.5. IPTC was originally intended for journalism applications. It has been widely accepted by news and commercial photographers as a standard format of embedded metadata. It extends EXIF, and enables embedded descriptive information such as photographer names, copyright information and captions. IPTC is undergoing a transformation toward an XMP-based system that takes full advantage of XML (Extensible Markup Language), RDF (Resource Description Framework) and Dublin core. Although XMP is not yet well supported, this

format is gradually gaining acceptance over the world. The basic metadata tags defined by the XMP format are those derived from the Dublin Core Metadata Initiative such as titles, descriptions, and creators. The XMP standard is designed to be extensible and flexible. It allows users to add their own metadata along with the basic XMP tags.

Many image metadata tools are available nowadays. They help to capture, share, and leverage the valuable metadata stored in embedded metadata formats. They can automate many process that required manual manipulation years ago. Those tools primarily work as metadata viewers, metadata editors, or image archiving applications for searching and exporting data.

Embedded metadata formats are helpful in the field of PER, because they offer a secured and effective way to handle a large amount of metadata of PER photos, i.e., date and time, spatial coordinates and annotations.

3.3. Evolution of PER Information Release

PER information is so time-sensitive and perishable that the Internet has become the modern way to release PER information as soon as it became operational. Web-based reports rapidly replaced the traditional hardcopy reports. The way to release PER information over the Internet has evolved with advances in digital cameras, GPS units, and Web technologies. This evolution can be retraced by examining the GEES website in existence since the inception of the Internet. Since 1995, GEES went through three major

updates: (1) Internet documentation; (2) Web-based GIS system; and (3) Google Maps application. Future developments will be described in detail in the next section.

3.3.1. Internet Application

To our knowledge, the GEES PER report on the 1995 Hyogoken-Nanbu, Japan, earthquake (Bardet et al. 1995) is the first PER report posted on the Internet. This report was written in Mosaic, a predecessor of the Hyper Text Markup Language (HTML), which had been officially released in 1993 by the National Center for Supercomputer Applications (NCSA). The original Mosaic report was released online only nine days after the reconnaissance team arrived in Japan and ten days before the hardcopy report was distributed. This Mosaic report was written based on preliminary reports in Japanese (Oka et al. 1995a; Oka et al. 1995b). It contained photographs that were scanned from films using flatbed scanners at Gifu University, Japan. The texts and photographs were transmitted by FTP (File Transfer Protocol) to the University of Southern California. Those materials were then compiled into a Mosaic document posted on the Internet. The photographs were of poor resolution in order to reduce the time required for uploading and downloading. After the 1995 report, plenty of PER reports have become available in Web version. They share many commonalities with this early report, although they have advanced HTML formatting features and higher resolution pictures. Application of the Internet for PER purposes removes the need for physical storage room of hardcopy reports, and enables easy accessibility for users located everywhere as long as the Internet access becomes available.

3.3.2. Web-Based GIS System

As shown in Table 3.2, GEES started to apply Web-based mapping technologies after the 1999 earthquakes in Kocaeli, Turkey; Chichi, Taiwan; and Düzce, Turkey. In addition to these web-based maps, GEES reports evolved toward a common format, including general earthquake information, and aerial and field surveys.

In contrast to the 1995 report, the 1999 reports emphasized geospatial information. Pictures were geo-referenced using specially developed EXCEL VBA (Visual Basic Application) macros. The macros read the GPS tracks, identified the photo files that had been time stamped, and calculated the longitude and latitude of photos. The same macros also created HTML reports, and GIS layers of PER photos. As shown in Figure 3.6, the GIS layer contained points, each of which represented a photo. It was displayed on the Internet using an Internet Map Service (IMS). This GIS way of releasing PER information helped researchers to understand the spatial relation between earthquake epicenter and damage locations. However, one of the major issues in 1999 was to find detailed base maps, as digital maps were not commonly available everywhere, especially in remote parts of the world, at that time.

Figure 3.7 illustrates the tools required in the workflow adapted at this stage: a GPS unit with a small antenna, a digital camera, a video camera, and a laptop computer. The collected information is exported from the devices and imported to the computer, which produces Web reports and GIS maps. Those final products are transferred to a server and become accessible to public on the Internet.

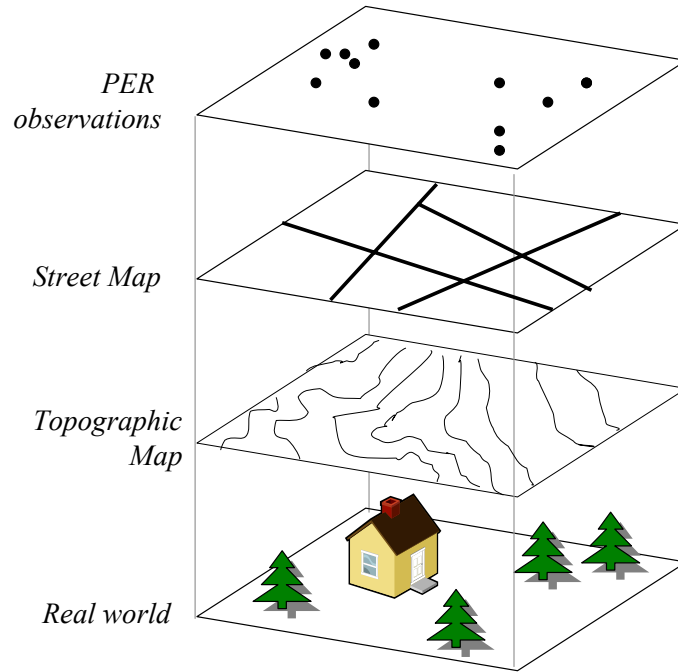


Figure 3.6 Layer structure for GIS systems

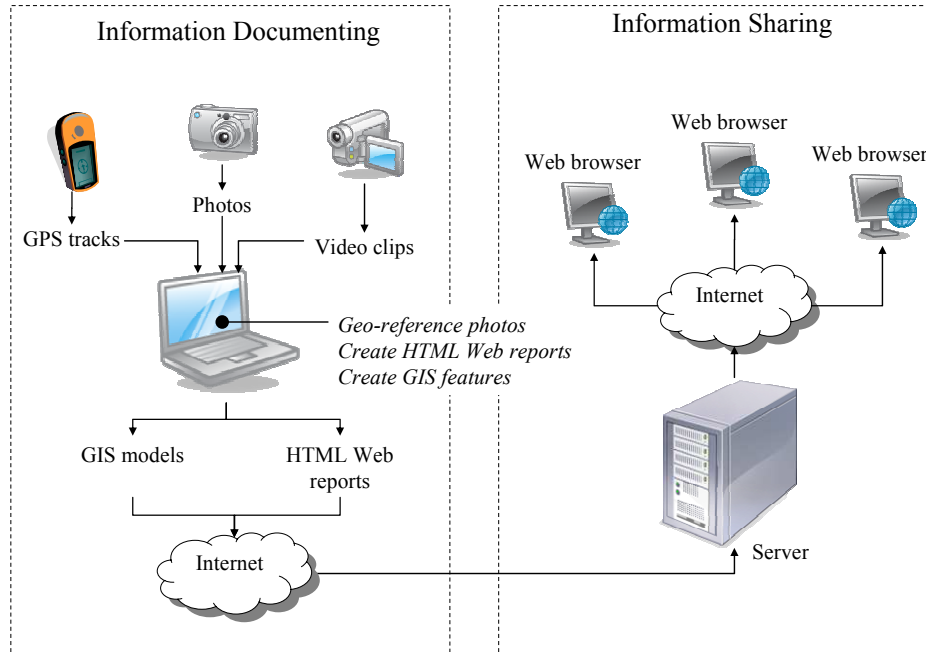


Figure 3.7 Main tools used in PER

The subsequent 2001 and 2004 reports (Table 3.2) inherit many traits from the 1999 reports. The photos have a higher resolution due to advances in digital cameras. The IMS has also a more interactive interface with many query options.

3.3.3. Google Maps Application

Digital base maps (e.g., street maps, satellite imagery and topographic maps), which were not easy to be obtained before, become readily available for many regions, particular in the United States. Many agencies provide GIS maps through gateways known as Web services. Meanwhile, a few third-party Web applications (e.g., Google Maps) bridge data providers and users. They provide users with ready-to-use functions to retrieve digital map data remotely without pain while interacting with Web services. They allow PER researchers to focus their efforts on PER information rather than Web programming. The selection of third-party Web applications depends on users' preference and programming skills.

The technology of database is significant to manipulate a massive amount of PER information. Fortunately, many third-party Web applications support customized databases. Benefited from database technology and Web application, a database-driven application based on Google Maps, PER photo repository, has been launched on the GEES website. It has replaced individual earthquake-specified GIS models. This system retrieves base maps from external sources and displays relevant PER information that is stored in an internal database. The system core is the internal database of PER

photographs, which includes the primary metadata of photos, such as date and time, locations, captions and other essential information for PER researchers.

The system benefits from Google Maps Application Program Interface (API), which exposes the entire Google Maps interface for customization. As illustrated in Figure 3.8, this system consists of two essential components: an interactive search interface based on Google Maps, and a Database Management System (DBMS) as the storage mechanism of photo metadata. They communicate each other through AJAX (Asynchronous JavaScript and XML) technology, which has particular advantages in creating responsive dynamic Web applications.

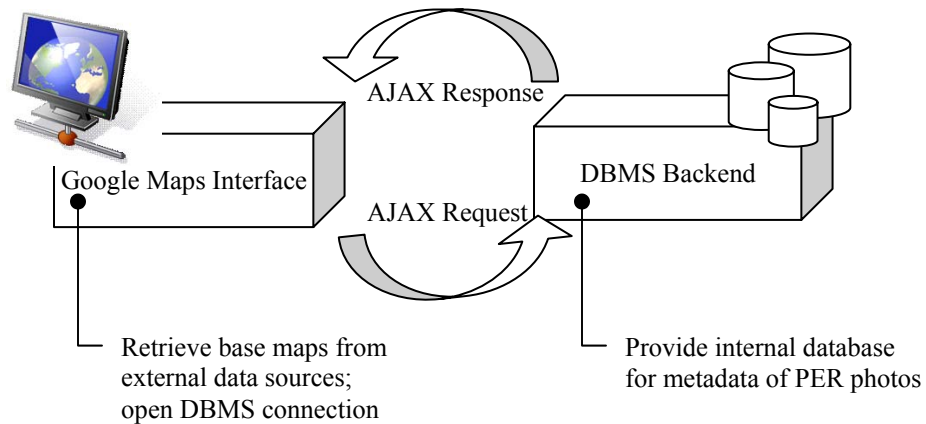


Figure 3.8 GEES photo repository integrating Google Maps with database

Figure 3.9 illustrates software configurations of the system. The system is hosted in a Web server running Red Hat Enterprise Linux 4 and Apache HTTP server patched with PHP (Hypertext Preprocessor). PostgreSQL was used to construct the metadata database

for PER photos. PHP (Hypertext Preprocessor) was employed to connect DBMS and produce interactive Web interfaces coded in Dynamic HTML (DHTML).

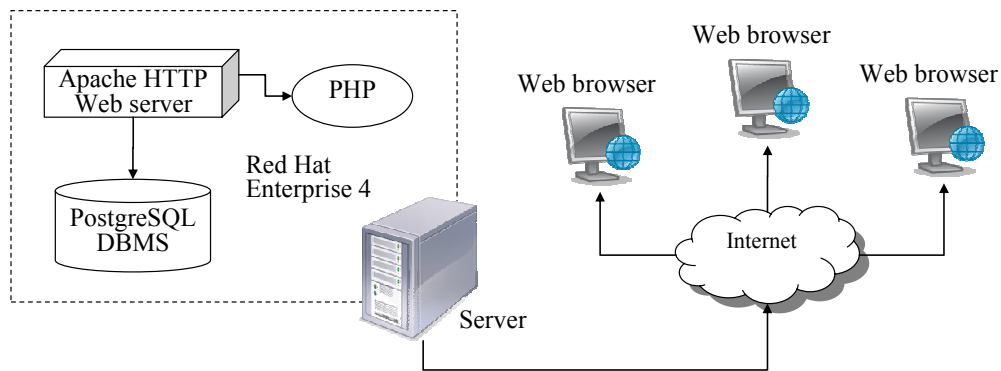


Figure 3.9 Software configurations for GEES photo repository

Figure 3.10 shows an interface of GEES photo repository that includes typical components of Google Maps, e.g., the navigation bar, mode buttons, the scale bar, and the overview window. At the top left corner, a drawdown menu lists earthquakes stored in GEES database.

As shown in Figure 3.11, the earthquake selection triggers a query, and displays relevant photos on Google Maps along reconnaissance GPS tracks if any. Photos are displayed as small balloons colored depending on the reconnaissance dates. GPS tracks and the map legend can be toggled on and off. Clicking on a particular balloon displays an information window along with a photo thumbnail and its metadata, e.g., date and time, location, and engineering annotations. Higher resolution photos can be displayed by

clicking the thumbnail. In the future, additional search capabilities could be deployed, provided that additional metadata be included.



Figure 3.10 PER photos searchable through earthquake names



Figure 3.11 GEES repository of aerial and field surveys for 2004 Japan earthquake

For post-earthquake reconnaissance, Google Maps offers numerous advantages over GIS-IMS applications. They reduce the time-consuming effort of identifying sources of base maps and geo-referencing these maps in remote areas of the World. Google helps PER researchers to focus their energy on collecting information instead of web programming. One drawback of the system architecture in Figure 3.8 is that photos are separated from their photo, and that metadata are arbitrarily stored in databases without any standard structures and formats.

3.4. Next Step – Embedded Metadata

Embedded metadata enable portable digital images that carry embedded information. Many embedded metadata aware programs become available nowadays, and they pave the way to archive and distribute PER photos with embedded metadata. Those photos can be transformed later into many formats according to users' need. Embedded metadata escape the need for database and Web programming, and they largely simplify the procedure for creating PER data repository. This new approach also improves data integrity by minimizing the chance of information loss. Embedded metadata are particularly useful for managing a massive amount of information that rapidly grows over time, such as PER information with an exponential growth.

3.4.1. Application of Embedded Metadata

Figure 3.12 schematically illustrates major steps to use embedded metadata for archiving and distributing PER photos on the GEES website.

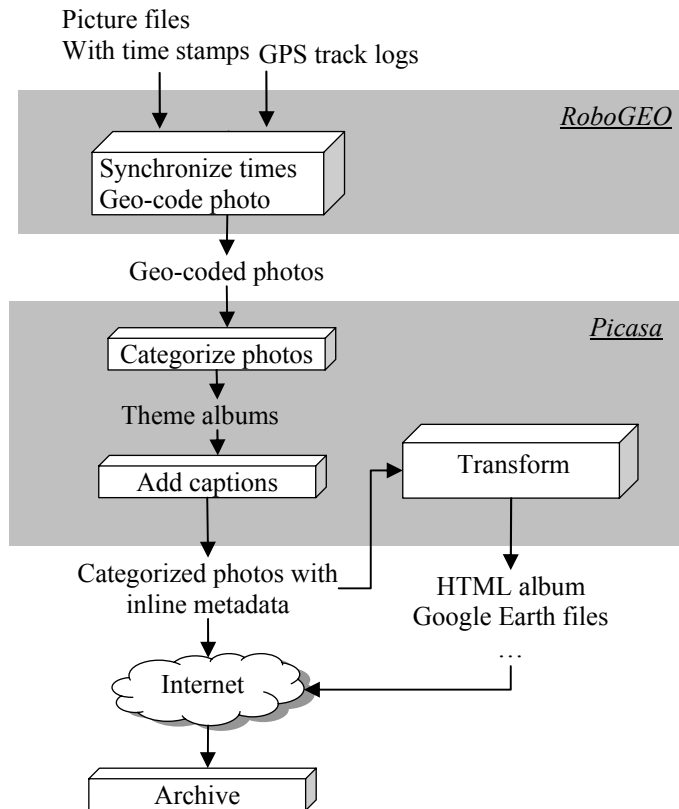


Figure 3.12 Workflow for generating and archiving photos with embedded metadata

As shown in Figure 3.12, PER photos were time-stamped when they were taken in the field. Those photos are imported together with GPS track logs into a commercially available program called RoboGEO (<http://www.robogeo.com/home/>). Using the principle of geo-referencing (see Figure 3.5), RoboGEO correlates the timestamps with the GPS track logs and computes spatial coordinates for each photo. Those coordinates are then embedded to the photo file in EXIF. The geo-referenced photos are then transferred to another program known as Picasa (<http://picasa.google.com/>), a free Google product designed for photo management. Those photos are grouped into different

categories and form a few theme albums. Photos can be polished or edited at this stage. After that, captions are typed into IPTC header for each photo. Professional expertise is needed here to annotate photos using proper terminologies in a consistent manner. Additional metadata can also be added, such as keywords for damage types, damage levels, organizations, and so on. Experts in earthquake engineering will however need to reach a consensus about some standard terminologies for annotating photos in order to make them understandable to a wide audience.

Once photos are geo-referenced and annotated, they are ready to be uploaded into a PER repository. As previously mentioned, photo metadata can be extracted using many applications, which allow to organize and display photos in different ways, for instance, for creating HTML albums, or visualizing photos with Google Maps and Google Earth.

3.4.2. Example – 2008 Wenchuan Earthquake

The approach described above was applied to the post-earthquake reconnaissance of the May 12, 2008 Wenchuan Earthquake. Sponsored by NSF, the reconnaissance team performed a five-day field investigation within earthquake-affected areas. As illustrated in Figure 3.12, the PER photos were embedded with metadata as previously explained. They were displayed on the GEES website in two different ways: (1) HTML Web photo albums; and (2) Google Earth files viewable using Google Maps and Google Earth. The Web photos albums, which are organized by reconnaissance dates, were generated using Picasa.

Figure 3.13 shows a web album of reconnaissance photos collected in the same day. This album has a two-level structure. The upper level is a contact sheet displaying all photos as small thumbnails, each of which links a lower level webpage displaying a single photo and its accompanying caption in higher resolution.

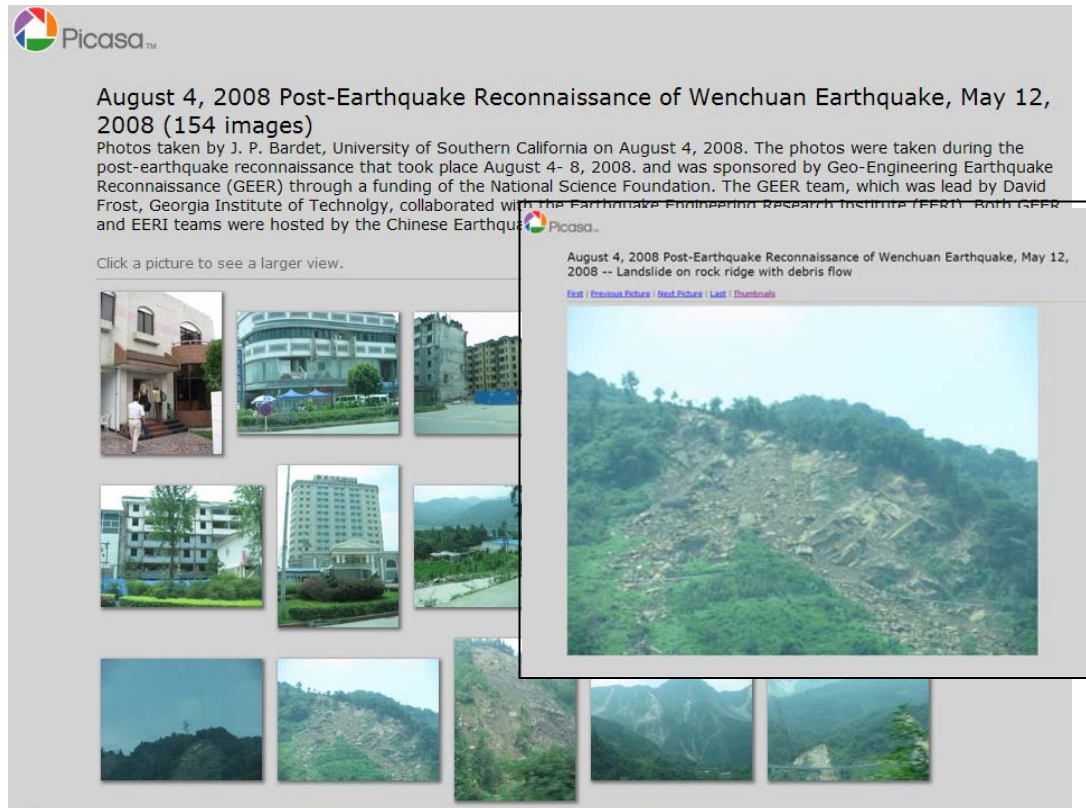


Figure 3.13 HTML Web album generated for the 2008 Wenchuan earthquake

Figure 3.14 shows how Google Earth displays the PER Google Earth file, i.e., KMZ file. Photos appear as small thumbnails located where they were taken during the reconnaissance. Clicking on the thumbnail displays a new window with a high resolution

photo with annotation. Google Earth also offers the advantage of 3D effects trapping viewer into a virtual representation made of satellite images and earthquake damage.

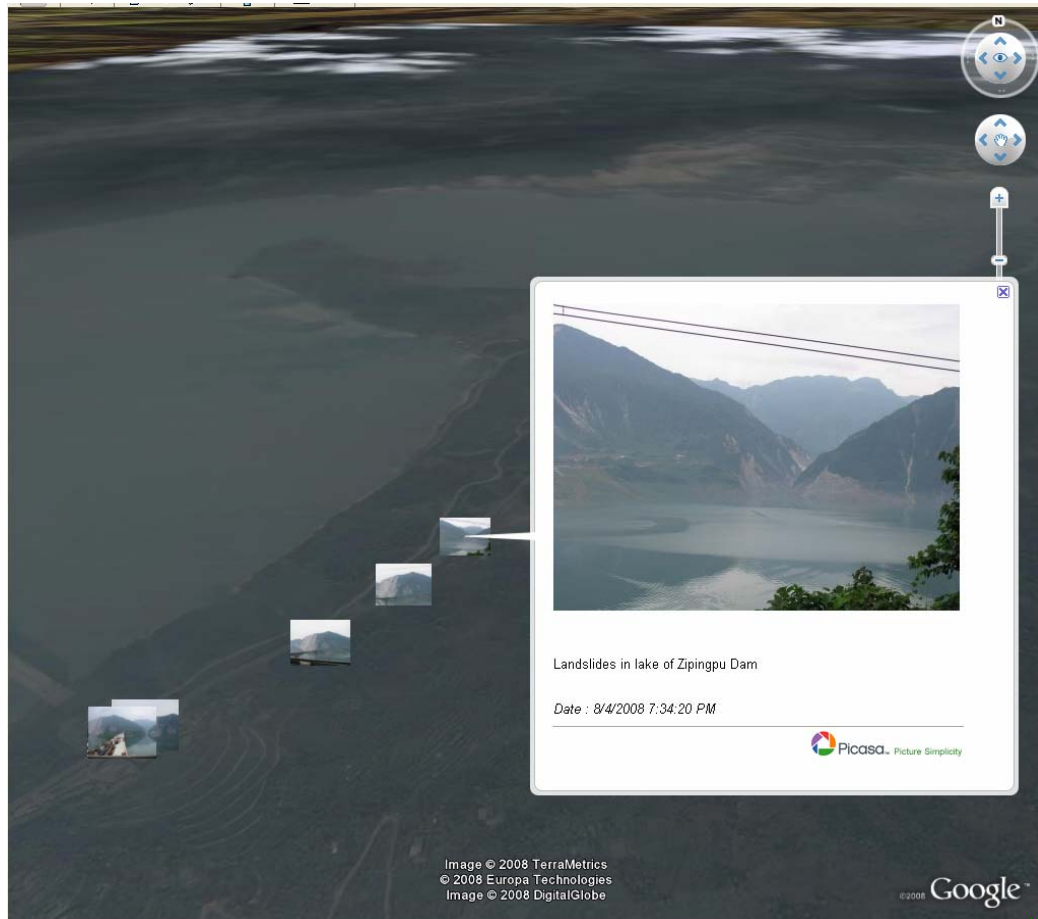


Figure 3.14 PER data displayed by Google Earth (map data from Google Earth)

Compared to Google Earth, which is a desktop application, Google Map displays PER photos as a Web application. Users are able to view data through their Internet browser without having to install Goggle Earth on their computer. Figure 3.15 shows how Google

Maps displays the KMZ file that Google Earth displayed in Figure 3.14. The look is similar, except for the absence of 3D effects.

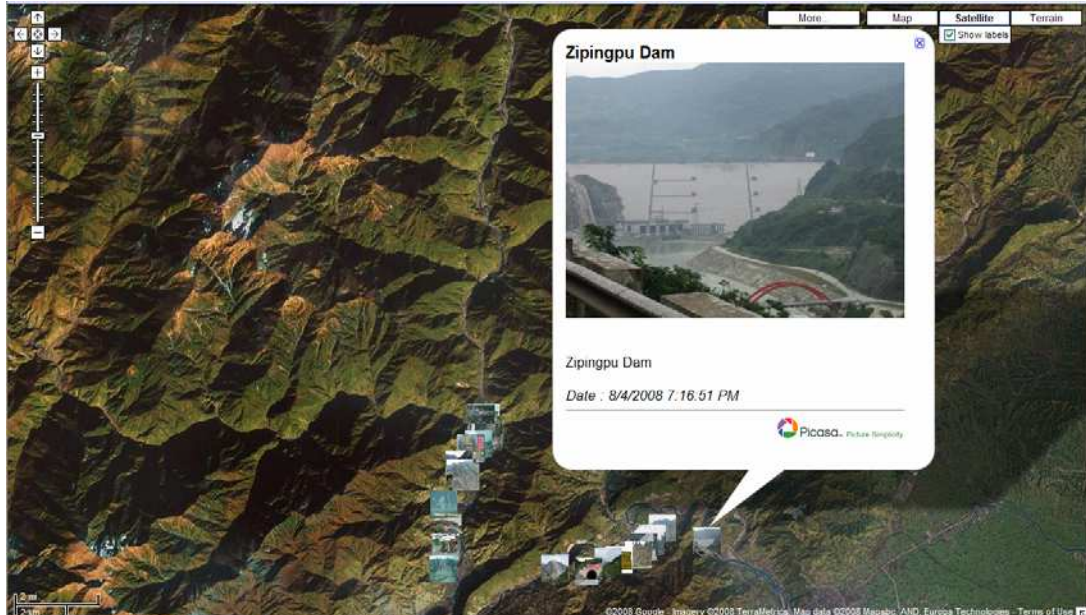


Figure 3.15 PER data displayed by Google Maps (map data from Google Maps)

3.5. Scale-up to Virtual Earthquake

Embedded photo metadata are critical for automating the data workflow for PER websites. They alleviate the few technical difficulties that one encounter when developing Google Maps API. The approach may encourage the public to send their geo-referenced photos into scientific and engineering data repository of earthquake damage. However one needs to get prepared for an explosion in the volume of PER information if the public is to contribute to the whole process. We need a robust system that has sufficient capacity to support massive volume of highly diversified information and

numerous players. Figure 3.16 schematically illustrates a proposed scaled-up system for Virtual Earthquakes. It receives data from multiple contributors at different locations, and releases data to users who have Internet access through Web browser.

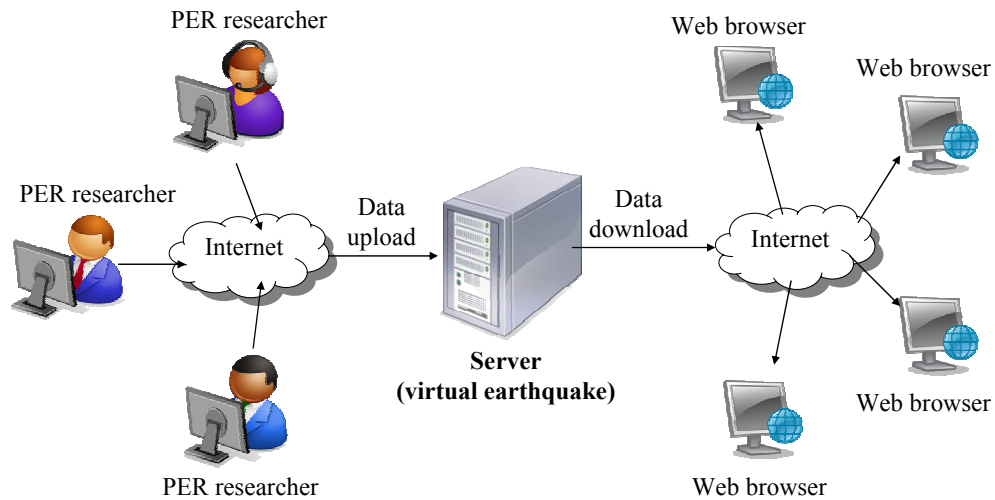


Figure 3.16 A system supporting multiple contributors and users

3.5.1. Extensible Format

So far photo metadata only contains basic information, e.g., time, spatial coordinates and annotations. In the future additional metadata may be required to create Virtual Earthquakes. One of such additional information may be the view orientation. The zoom value, aperture and other optical properties of the cameras may be also of some usage to advanced users. Another issue is the selection of a particular exchange format for PER photo metadata. The XMP format emerges as a future direction due of XML extensibility. It has well-defined basic metadata structure readily adaptable to applications (Adobe,

2005), and flexible enough to define, create, and manage PER-specific metadata. It has become necessary to develop for the PER community to develop a dictionary of PER-specific metadata which provides guidelines for standardizing the way PER researchers report PER information.

3.5.2. Data Quality and Search Engine

Data integrity becomes a challenge when a large number of data providers are involved in Virtual Earthquakes. Data quality needs also to be monitored at the format level as well as the content level. Tools and XML schemas may help to check for format conformity to some extent. However, content relevance and consistency will always rely on expert judgments. Limiting data upload capabilities to a few trusted data providers may be a way to prevent data from being contaminated, but this would invalidate the goal of tapping into the public as data providers. It may be preferable to assign various expertise levels to PER data providers and leave the decision to viewers and users to trust or discard data.

With the growth of information volume, a powerful search engine may become an ally in filtering unwanted information by data providers, times, organizations, annotations and so on. Queries could become more effective when annotations are well written with descriptive information, and contains predefined categories, and even damage levels.

3.6. Summary

Post-earthquake reconnaissance is critical to learn time sensitive information in the aftermath of earthquakes, and to improve knowledge in engineering and sciences. Since 1995, PER has evolved drastically with advances in GPS units, digital cameras, and web technologies. This PER evolution was retraced using PER examples sponsored by NSF in Turkey, Taiwan, India, Japan and China since 1999. Compared to their hardcopy predecessors, the modern PER web reports now contain not only a qualitative description of earthquake effects but also detailed and accurate information about the positions, time and description of engineering observations. The next PER frontiers is embedded photo metadata, which enable information (e.g., spatial coordinates, time, annotations, etc.) to be attached to photo files. Embedded metadata has the potential of highly automating the data workflow for efficiently documenting and distributing PER information at a very large scale, including the public. Embedded metadata-based approach may lay the foundation of Virtual Earthquakes that assembles piece by piece by many contributors with or without technical expertise. The scale-up to build Virtual Earthquakes will require further planning and involvement of the earthquake engineering community.

Chapter 4. Information System for Liquefaction Case Histories

This chapter applies the technologies described in Chapter 3 to distribute the USC database of liquefaction-induced deformations (Bardet et al. 1999; Hu 2003). Although the USC database includes much more information than its precedents, its values has not been fully exploited for improving current procedures of regional prediction of liquefaction-induced ground deformations. This chapter is intended to construct an effective gateway to bridge valuable data and data users who are interested in using this data for their studies. The relevant work has been presented in the 5th China-Japan-US Trilateral Symposium on Lifeline Earthquake Engineering (Liu et al. 2007).

4.1. Sharing Geotechnical Information

Geotechnical information depicts the characteristics of upper soil deposits on which rest most of our civil infrastructure. It can be derived from geotechnical investigation reports based on geotechnical field tests and laboratory tests. This type of information is often overwhelming and comes from different agencies that present data in non-standard formats. It is a big challenge to compile such tremendous amount of diversified information into a seamless data central that receives and releases data across different platforms, applications, and formats. USC geotechnical group have made efforts to apply advanced information technology to manage and exchange geotechnical information. Exchange formats, storage mechanisms and transmission protocols are three major issues

that need special attentions. XML and its revised version, GML (Geography Markup Language) are promising to be the standard format for exchanging geotechnical information over the Internet; however XML schemas specific to geotechnical data are still under development and no unique schemas have received universal acceptance (Mokarram 2006). As for the data structures of geotechnical laboratory tests, an object-oriented metadata model has been developed and expressed in XML schemas (Bardet et al. 2005). Relational RDBMS was employed as the storage mechanism for geotechnical information (Hu 2003); it is experiencing transformation toward object-oriented spatial database that supports spatial queries. In the meanwhile, Web-service techniques were proposed to tunnel the geotechnical data and massive potential users (Zimmermann et al. 2006).

Sharing geotechnical information is a broad topic and the present study only covers a small piece. This study aims to use recent information technologies to develop a system that enables (1) visualization of case histories of liquefaction-induced ground deformations, and (2) accessibility of those case histories over the Internet.

4.2. Web-based GIS Systems for Sharing Spatial Data

Information handled in this specific application is of spatial complexity. The GIS technique stands out to be a potential solution.

In the early stage, GIS systems were confined to desktop applications in which visualization and spatial analysis were the kernel issue. The invention of the Internet

triggered an era of information explosion. Accordingly, to share spatial data becomes equally attractive compared with demands of spatial analysis in GIS systems. GIS started to embrace Web technology and motivated a large number of Web-base GIS applications.

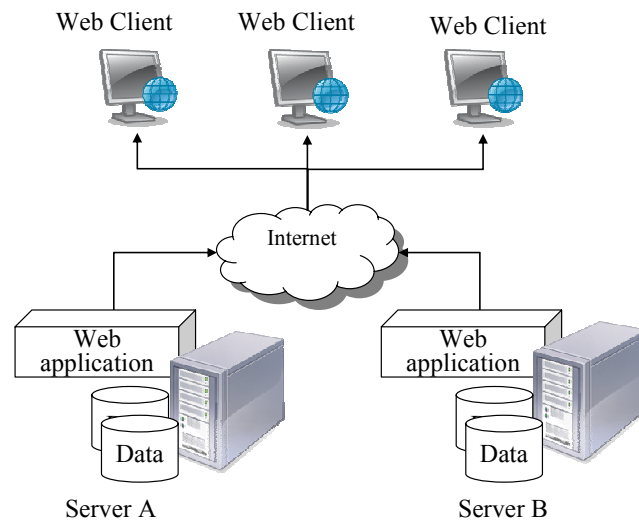


Figure 4.1 Self-supported Web applications

As shown in Figure 4.1, Web-based GIS systems first appeared as self-contained systems that solely depend on internal data. Communication takes place between Web servers and Web clients, but not between Web servers. For instance, the system developed by Chang and Park (2004) is one of those examples to manage borehole and geological data for a local urban area of Seoul in Korea. The independency may strengthen the security level. However, isolation may also cause inconvenience. The system can be quite heavy since it has to possess both application-specific data and secondary supplemental data such as the street maps and topographic maps. Duplicated efforts cannot be avoided particularly toward secondary data that only serve as reference base maps in a specific Web

application. Although large efforts are required to obtain those common data in the past, they nowadays become available at ease from external data providers, such as USGS (U.S. Geological Survey, <http://www.usgs.gov/>) GIS data library, which plays a singular role in collecting nation-wide GIS data. The workload can be reduced remarkably, if we enable collaborations among Web servers and encourage information sharing. It becomes a trend to generate lightweight systems that use external data without possessing them.

Figure 4.2 shows Web servers situated in a networking environment. Web servers communicate each other and exchange information. The roles of those servers include two types: one is to offer Web applications to Web clients; and the other is to provide spatial data to those applications in remote servers. Two essential issues are pertinent to paving the road to GIS network. One is the standardization of spatial data formats, and the other issue is related to Web service infrastructure. OGC (Open Geospatial Consortium) is the lead in this field, and proposes the concepts of WMS (Web Map Service) and WFS (Web Feature Service) which are gradually accepted by the universal GIS community. Accordingly, Web-based applications are not self-contained any longer and depend on multiple data providers through Web services. However, for a common user who has limited knowledge on computer science, adaptation of Web service in his or her applications is not easy. Fortunately, a few third-party programming tools are available and make life easier. Google Maps is one of those products. Those tools remove the barriers while coping with Web services programming. As a result, the process to

communicate Web services becomes transparent to Web application developers. Figure 4.3 schematically illustrates such a system with the presence of the third-party tool.

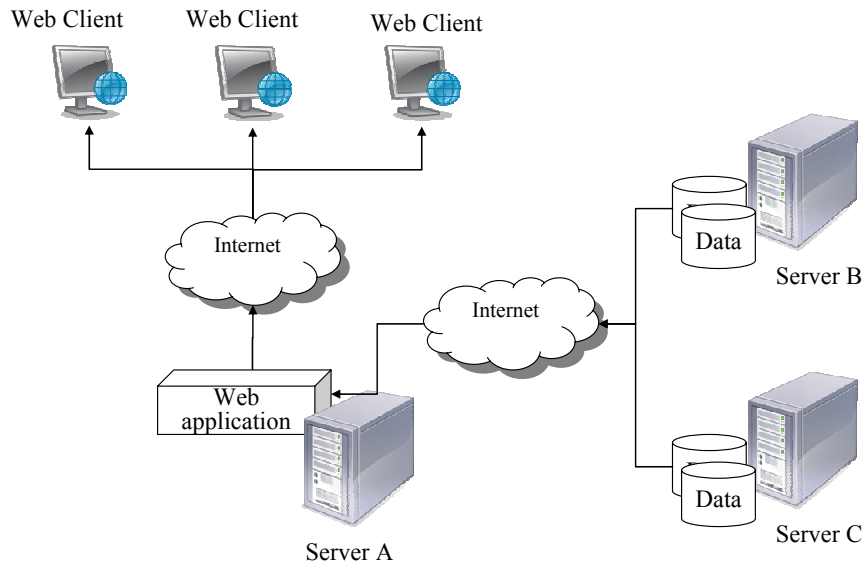


Figure 4.2 Web application using external data over Web services

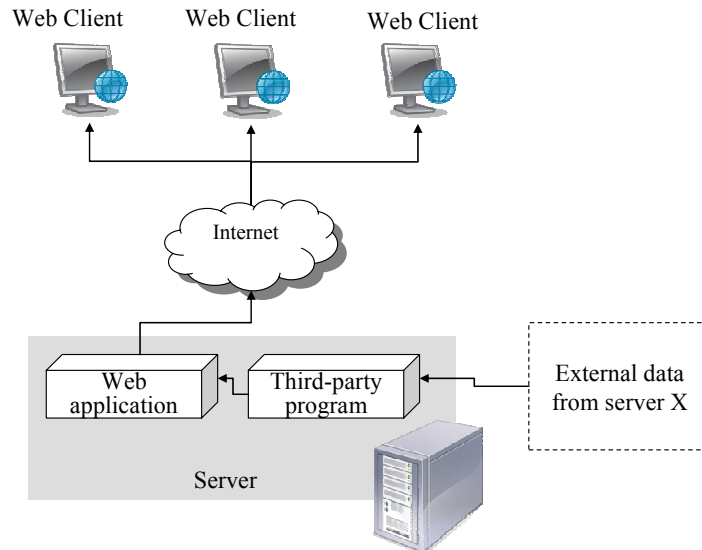


Figure 4.3 Lightweight Web application

4.3. Application of Google Maps

As previously mentioned in Chapter 3, Google Maps is a free Web map server application and technology first announced in 2005. It features a draggable and zoomable map that locates destinations and creates driving directions. The map data used in Google Maps is provided by Tele Atlas and NAVTEQ. The small patches of high-resolution satellite imagery are mainly provided by DigitalGlobe and its QuickBird satellite, and the rest of them come from government sources (Schutzberg 2005). Google Maps API was released in late June 2005, and it later triggered an explosion of Google Maps applications, known as map mash-ups.

As one of the most significant users of AJAX technology, Google employed the paradigm in its map products to achieve fast performance (Wusteman and O'hleceadha 2006). As the name implies, AJAX uses JavaScript and XML to enable asynchronous communication between browser client and server-side system, and achieve responsive, interactive, and customizable Web applications. In contrast to conventional Web applications that always deliver data together with the HTML codes required to render the user interface, AJAX applications only deliver data when user interfaces have been delivered and configured once. AJAX eliminates the time for delivering user interfaces so that it dramatically reduces the network load of Web applications.

Google Maps applications have several noticeable advantages. First, Google Maps offers a quick solution for lightweight Web-mapping systems. Aerial imagery and street data are transported from the remote servers by Google Maps API. Therefore, there is no need

for possessing secondary spatial data that is often large in volume. Second, Google Maps enables fast mapping performance due to the presence of AJAX technology. Third, as the Google Maps code is almost entirely JavaScript and XML, the degree of difficulty is relatively low for developing a Google Maps application in comparison to the application of Web service. Google Maps is not a product designed for spatial analysis. However, it is an ideal solution to those mapping applications whose primary function is to visualize and disseminate location-related data with limited expectation of data analysis.

4.4. Lightweight System for Liquefaction Case Histories

4.4.1. System Architecture

Figure 4.4 conceptualizes the information system of liquefaction case histories. Similar to the system developed for distributing PER information as shown in Figure 3.8, this present system consists of three components: (1) DBMS backend; (2) Google Maps front-end; and (3) AJAX mechanism for message exchange. The USC database (Bardet et al. 1999), as described in Section 2.3.3, is the system backend working as a data engine. A customized Google Maps interface interacts with clients and handles their requests. Upon users' requests, data are retrieved from the database backend through AJAX requests and responses, and are ultimately presented in the front end that retrieves the secondary spatial data from remote Google servers.

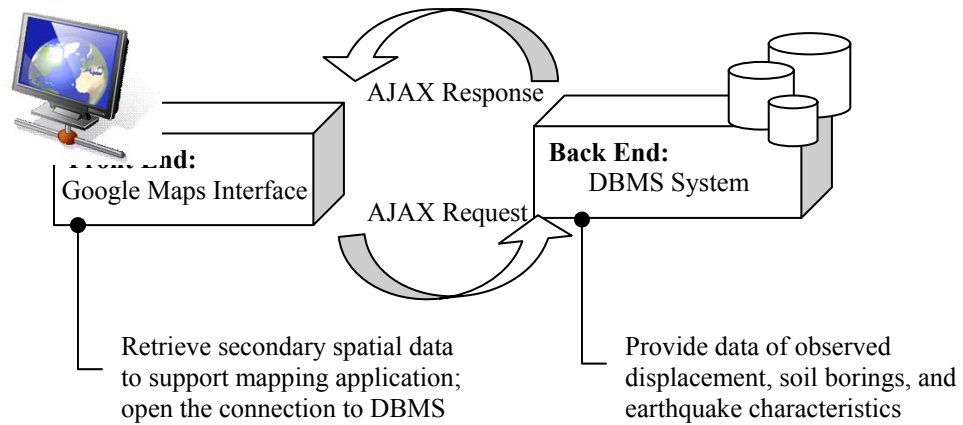


Figure 4.4 Major components constituting a lightweight system

4.4.2. System Configuration

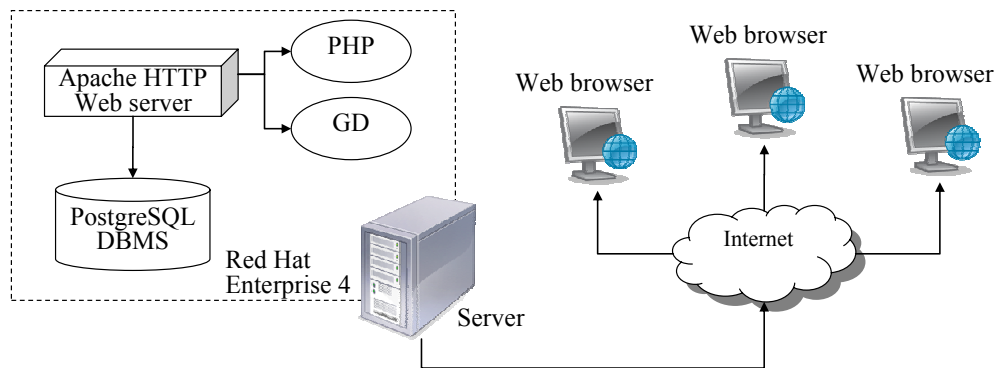


Figure 4.5 Software configurations

Figure 4.5 illustrates the system configuration. Similar to the system developed for PER purposes as shown in Figure 3.9, the present system relies on same software with an exception of GD Graphic Library that patches PHP and helps to dynamically generate

images upon clients' requests in order to display displacement observations. The USC database was originally stored in a Microsoft Access DBMS which, unfortunately, was not fully supported by Linux operating system. To adapt to the new system, data were transferred into a new DBMS powered by PostgreSQL.

4.4.3. Data Structure

When data were transferred from the previous Microsoft Access database to PostgreSQL database, the data structure was kept intact as much as possible.

Figure 4.6 illustrates a simplified relational diagram for the database in PostgreSQL. There are four major objects: Displacement, Earthquake, SPT and CPT. They are illustrated as square boxes in Figure 4.6 with primary attributes denoted by ellipses. Displacement relates to Earthquake by a foreign key, EQ-ID, displaying many-to-one relationship. SPT and CPT are spatial objects with an attribute of location. Unlike the Earthquake and Displacement, SPT and CPT relate to other objects in spatial aspect without explicit connections. Data search of SPT and CPT can be conducted through spatial queries, for instance, a query of SPT tests that are performed within a window which bounds all available displacement measurements. The most valuable data associated with the site characterizations are the boring logs, whose access paths have been assigned to the attributes of SPT log and CPT log. Additional attributes of geotechnical boreholes, although not listed Figure 4.6, were in fact included in the data structure, such as drilling date, drilling equipment, ground water depth etc.

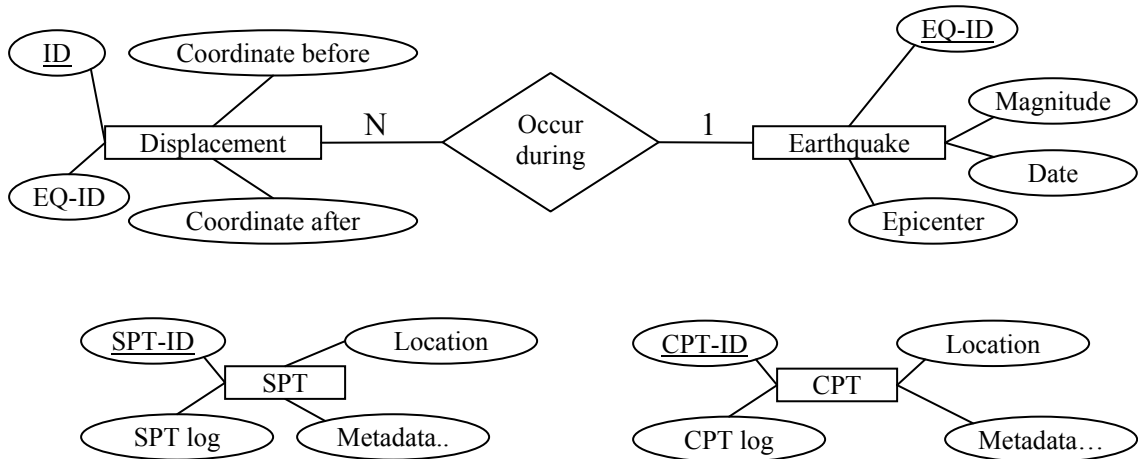


Figure 4.6 Relational diagram

4.4.4. Optimization of Vector Rendering

One of the challenges in technical perspective is how to speed up the visualization of a large number of displacement measurements.

Initially, a conventional approach was tested in this study for creating 2D vectors. Similar to the procedure for plotting geotechnical boreholes, displacement data were dumped into a well-formed XML document. Afterwards, instances of Gpolyline, a class defined by Google Maps API, were created from the XML document. Unfortunately, this process became impractical because of extremely low speed while the number of vectors is large. Hence, a better solution was developed later based on the concept of dynamic tiles (Purvis et al. 2006).

The basic idea of dynamic tiles is to divide a Google Maps into sub-areas, each of which is covered by a GIF (Graphics Interchange Format) raster image of 256 by 256 pixels, known as a tile in the vocabulary of Google Maps applications. The number of tiles required to cover the whole map is determined by current zoom level. As shown in Figure 4.7, the number of tiles increases with the zoom level. If the zoom level increases once, each tile splits itself into four pieces, each of which still covers the same size of areas on computer screen, i.e., 256 by 256 pixels. A unique index is assigned to each tile according to the zoom level and its relative position on the map.

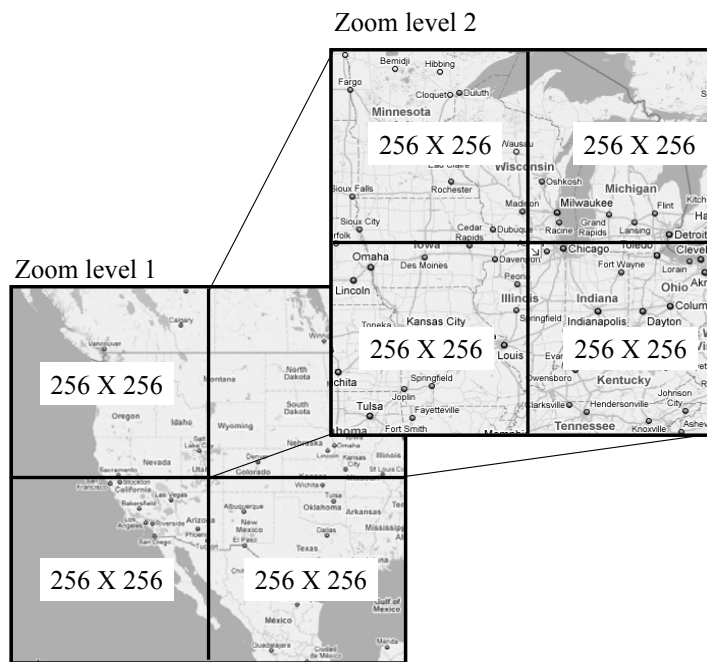


Figure 4.7 Dynamic tiles split when zoom level varies

There are two types of tiles in this application. One is purely transparent covering areas without any displacement measurements, and the other has some measurements within its

boundary. The second type has transparent background and polyline objects drawn using GD Graphic Library in order to represent the displacement measurements. Once a zoom level is specified, a tile processor coded in PHP locates existing tile files based on their indices, or creates new tiles if they do not exist yet.

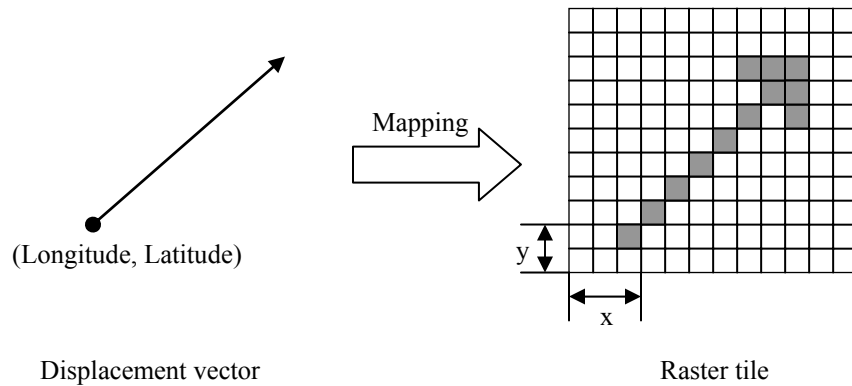


Figure 4.8 Mapping a displacement vector into raster image formed by pixels

Figure 4.8 illustrates how the PHP script plots displacement vectors in raster tiles using pixel representation. For an individual displacement measurement, for instance the displacement vector as shown in Figure 4.8, the script first identifies the tile in which the vector should locate. The index of the proper tiles can be determined by comparing the coordinates (e.g., longitude and latitude in accordance with WGS84 coordinate system) of the vector origin, to the corner coordinates of tiles corresponding to the current zoom level. Once the index of the tile is identified and this tile is visible under the current zoom level, the script does the following: (1) To map the origin of the displacement vector using pixel coordinates, i.e., (x, y) ; and (2) To fill the pixels and form a directive line

with arrow head using proper angle (for direction) and appropriate scale (for amplitude). Compared to the approach that generates vectors from XML documents, the usage of dynamic tiles shortens enormously the time required for displaying thousands of displacements from a few minutes to mere seconds.

4.4.5. Major Functions and User Interfaces

Figure 4.9 shows the entry page for the proposed system using Google Maps. This page was coded in PHP. The map type can be switched among three modes, i.e., street map, satellite imagery, and hybrid map, by clicking on the switch buttons at the top right corner. The map is zoomable through a navigation bar on the right hand side. A navigation window is situated at the bottom right. In this entry page, embedded PHP scripts open database connection, grab earthquake information and list them in a selecting box sitting at the left top corner.

Figure 4.10 shows a Web interface when one specifies the 1971 San Fernando, California, earthquake. A floating control panel with legends appears below the selecting box. Geotechnical boreholes, i.e., SPT and CPT, are represented as clickable balloons, each of which has a hidden information window that will appear upon clicking and provide information about the selected borehole. The borehole layer can be toggled on and off. From user point of view, the speed for visualizing boreholes is acceptable for the current database. No speedup algorithm has been used; however, it might need faster rendering algorithm when the database gets bigger in the future. Two type of speedup algorithm are available nowadays: setting visible zoom levels and clustering. The first approach is

straightforward by simply assigning visible zoom levels for each marker. Dense markers display only in high zoom level and disappear otherwise. The second approach is to cluster multiple objects as a group represented by a single marker.



Figure 4.9 Entry page (map data from Google Maps)

As shown in Figure 4.10, besides geotechnical borings, directive vectors are plotted using the mapping scheme illustrated in the preceding section. Those directive lines with arrowheads were plotted in such way that 50 pixels in length on the screen were equivalent to horizontal displacements of one meter on the ground. Figure 4.11 shows an interface using satellite imagery that contains the same data set as Figure 4.10.

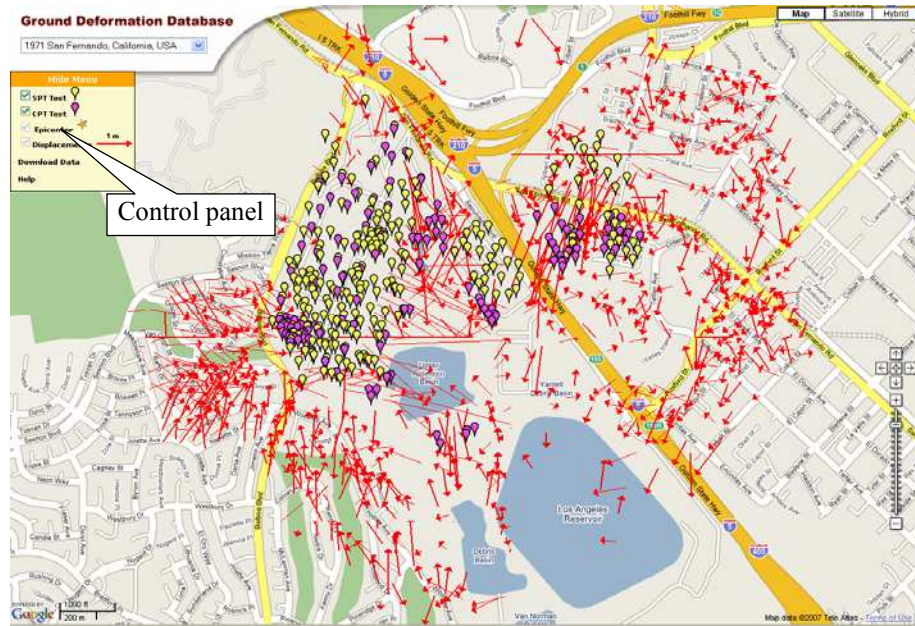


Figure 4.10 Available boreholes and displacements for the 1971 San Fernando, California, earthquake (map data from Google Maps)

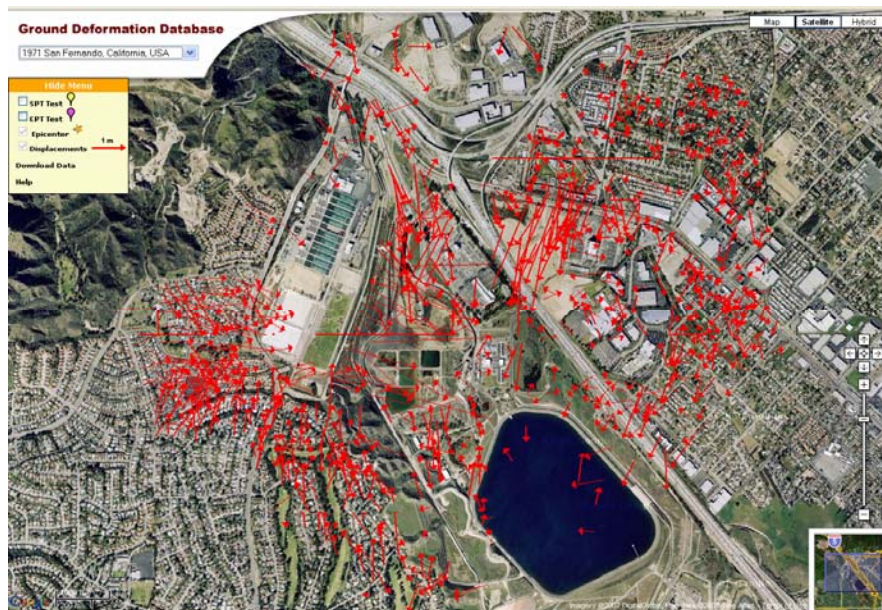


Figure 4.11 Satellite imagery as the background for the data set of Figure 4.10 (map data from Google Maps)

Figure 4.12 illustrates how the proposed system communicates the Web client, internal database and Google sever. The dataflow falls into two categories: data search and data download.

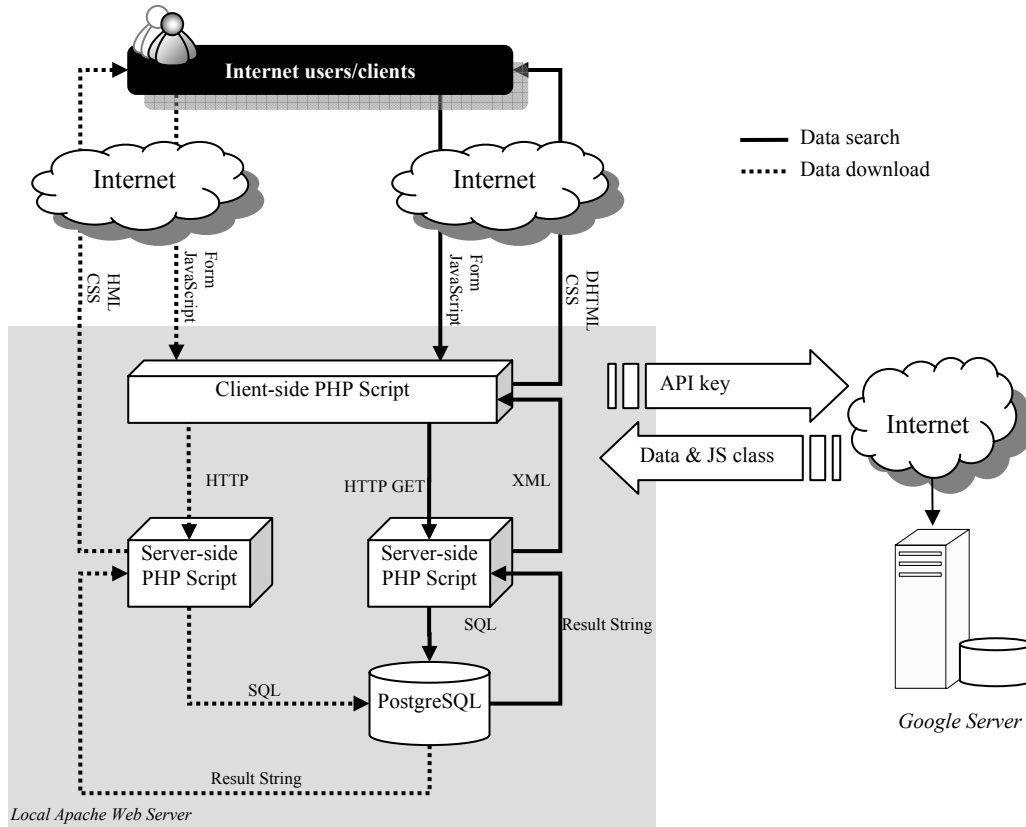


Figure 4.12 Communications between clients and servers

The system can conduct the following four functions:

- (1) Earthquake information search. PHP scripts connect the database, retrieve information of all available earthquake events, and present them in front of Web users.

(2) Visualization of displacements. Once an earthquake event is selected, server-side PHP scripts open the database and search displacements according to the earthquake identifier, parse resulting data in an XML document, and pass it to the client-side PHP scripts, which extract necessary information and plot displacements on Google Maps.

(3) Visualization of geotechnical boreholes. Once Web users request to display geotechnical boreholes, server-side PHP scripts open the database connection and query borings located in the neighborhood of displacement measurements. Search results are parsed into an XML document and sent back to the client-side PHP scripts for visualization process.

(4) Download data. Displacement data can be downloaded as a plain text that tabulates relevant information, e.g., the components of displacements, and their coordinates. Boring log files are also downloadable.

4.5. Summary

A new information system was developed to distribute case histories of liquefaction over the World Wide Web. It benefits from AJAX (Asynchronous JavaScript and XML), Web and database technology. This system takes full advantage of external spatial data offered by multiple data vendors, and enables a lightweight Web application with responsive and user-friendly interfaces.

Chapter 5. Case Study of Liquefaction Assessment

This chapter presents a case study on those case histories managed using advanced information technologies, which was illustrated in the previous two chapters. This chapter aims to scrutinize existing empirical models of liquefaction-induced lateral ground deformations, and to manifest insights on the next generation of models that can account for more physical mechanism of liquefaction-induced deformations.

5.1. Site Description and Earthquake Impacts

Figure 5.1 shows the vicinity the Van Norman Complex (VNC), which is located in the northern San Fernando Valley along Interstate 5 between the 405 and 210 interchanges. The site includes major water facilities operated by the Los Angeles Department of Water and Power (LADWP), such as the Los Angeles Reservoir with the Los Angeles Dam and the North Dike, the Los Angeles Aqueduct Filtration Plant, the Van Norman Bypass Reservoir, and the former Upper San Fernando Dam and Lower San Fernando Dam. Joseph Jensen Filtration Plant, Sylmar Converter Station and Juvenile Hall are adjacent to the LADW facilities in the north side. This particular site witnessed two damaging earthquakes in the past 40 years: the 1971 San Fernando earthquake, and the 1994 Northridge earthquake.

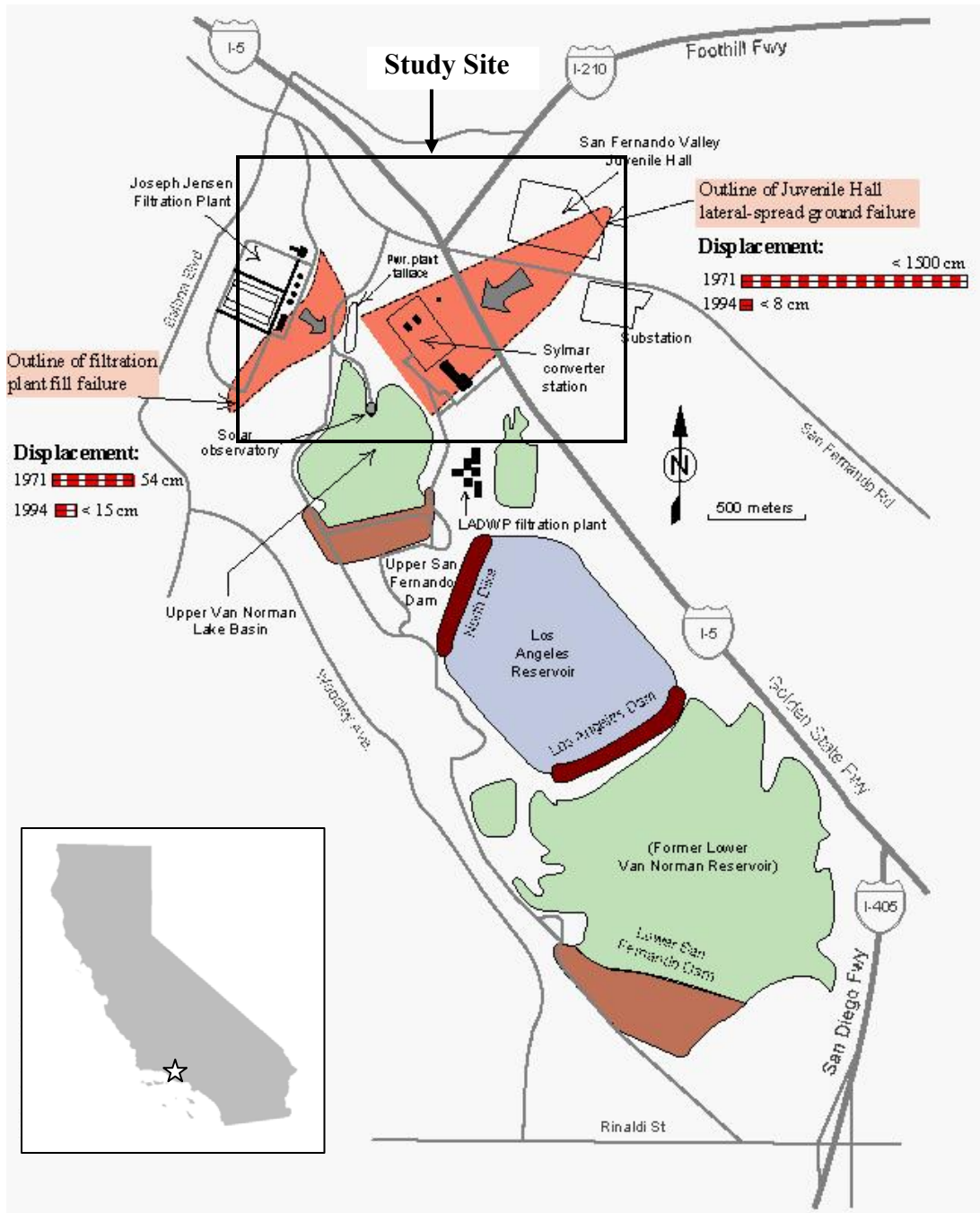


Figure 5.1 Liquefaction-related ground failures in the VNC vicinity after the 1971 and 1994 earthquakes (from USGS 1996)

Table 5.1 compares seismic parameters and resulting deformations after the two earthquakes. The 1971 San Fernando earthquake occurred on the San Fernando fault zone, a zone of thrust faulting, which broke the surface in the Sylmar-San Fernando Area and caused approximate 19 km long surface rupture. The maximum slip was up to 2 meters. The 1994 Northridge earthquake occurred on a blind thrust fault dipping down to the south-southwest beneath the northern San Fernando Valley. It produced the strongest ground motions ever instrumentally recorded in an urban setting in North America (SCEDC, Southern California Earthquake Data Center, <http://www.data.scec.org/>). After the 1994 earthquake, as indicated by a combination of GPS data and Interferometric Synthetic Aperture Radar data, significant after-slips occurred on the main fault after the main-shock, and additional shallow deformations happened to the west of the main rupture plane (e.g., Donnellan et al. 2002).

Table 5.1 Seismic parameters and resulting maximum deformations in two quakes

Earthquake Name	Date	Mw	Depth (km)	Fault Type	Epicenter Distance (km)	PGA (g)	Max Disp. (m)
San Fernando	2/9/1971 6:01 PST	6.6	8.4	Thrust	14	0.36- 0.4	3.85
Northridge	1/17/1994 4:30:55 PST	6.7	18.4	Blind thrust	12	0.72- 0.8	1.20

After the two earthquakes, ground failures (e.g., sand boil, surfacial cracks, lateral spreads and settlements) were widely observed within the VNC vicinity. One of the major reasons causing those damages was attributed to liquefaction in saturated granular soil deposits (USGS 1996). In response to the two earthquakes, in-depth post-earthquake

investigations were performed to geotechnically characterize the site and measure liquefaction-induced ground deformations. The USC database (Bardet et al. 1999) includes those case histories, which help us to better understand the mechanism of liquefaction-induced lateral ground deformations, and to evaluate the existing empirical procedures developed in the past. As shown in Figure 5.1, available geotechnical boring data in the USC database fall into a rectangle area of 2 by 2 kilometers. It is the study site of the present case study on liquefaction severity and resulting lateral deformations.

Post-earthquake investigations indicated less ground deformations in the 1994 Northridge earthquake although its seismic intensity was similar to the 1971 San Fernando earthquake. According to a USGS open file (i.e., USGS 1996), ground improvements after the 1971 earthquake helped to reduce the severity of ground failures in the 1994 earthquake. In 1971, up to 2 meters of ground displacement damaged Juvenile Hall buildings so severely that they were razed and eventually replaced. Investigations after the 1994 earthquake revealed that part of the 1971 failure zone failed again, but the magnitude of displacements decreased to less than 8 centimeters. The Joseph Jensen Filtration Plant was under construction on engineered fills when the 1971 earthquake struck. Liquefaction in alluvium under the fills produced about 0.5 meter of lateral displacements at the main control building, and displacements increased to about 1 meter near Upper Van Norman Lake. However, in the 1994 earthquake, the cumulative width of extensional failures in the fills measured was only about 15 centimeters, suggesting considerable success of installation of numerous gravel columns after the first earthquake.

5.2. Seismic Strong Motions

Figure 5.2 shows an intensity map and PGA map released by USGS after the 1994 Northridge earthquake. The study site situated within red areas that received severe impacts of the strong motion.

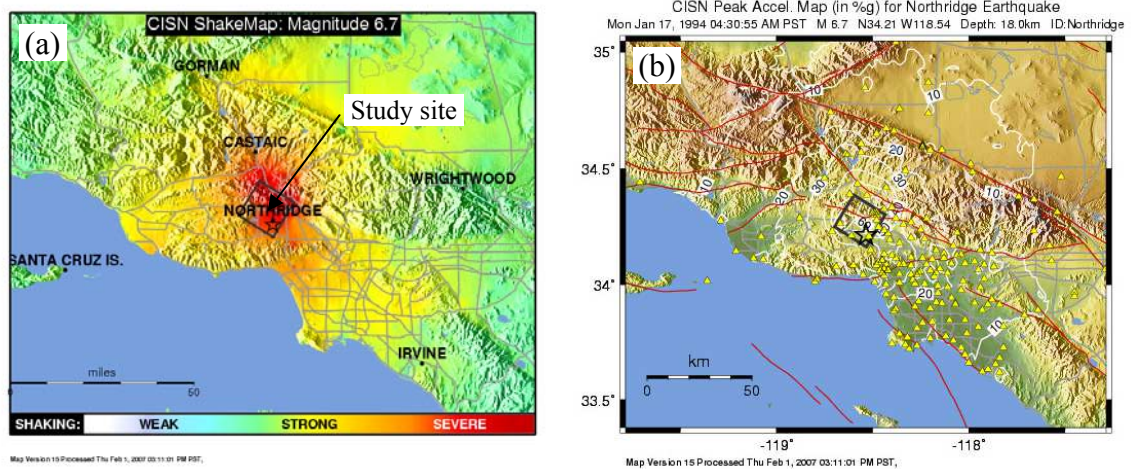


Figure 5.2 USGS ShakeMap for the 1994 shake: (a) Instrumental intensity; and (b) PGA (maps from USGS website <http://www.usgs.gov/>)

Figure 5.3 compares the PGA maps released by USGS after the 1971 earthquake and the 1994 earthquake. The study site experienced higher ground acceleration (i.e., ranging from 0.72 g to 0.8 g) in the 1994 earthquake than the 1971 earthquake.

Figure 5.4 and Figure 5.5 show the horizontal accelerograms recorded during the 1994 earthquake at the Jensen Filtration Plant Station and the Sylmar Converter Station, respectively. Those actual measurements provide some agreement with the values indicated in Figure 5.3. The present case study uses a PGA of 0.8 g to proceed the

assessment of liquefaction potential and deformations corresponding to the 1994 earthquake.

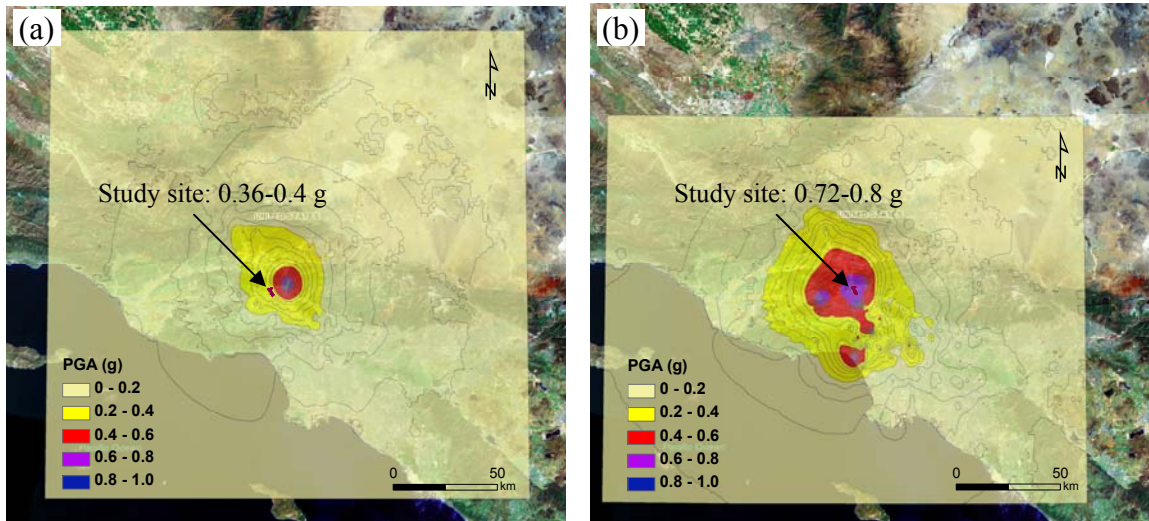


Figure 5.3 PGA at the study site during: (a) the 1971 quake; and (b) the 1994 quake (data from USGS website <http://www.usgs.gov/>)

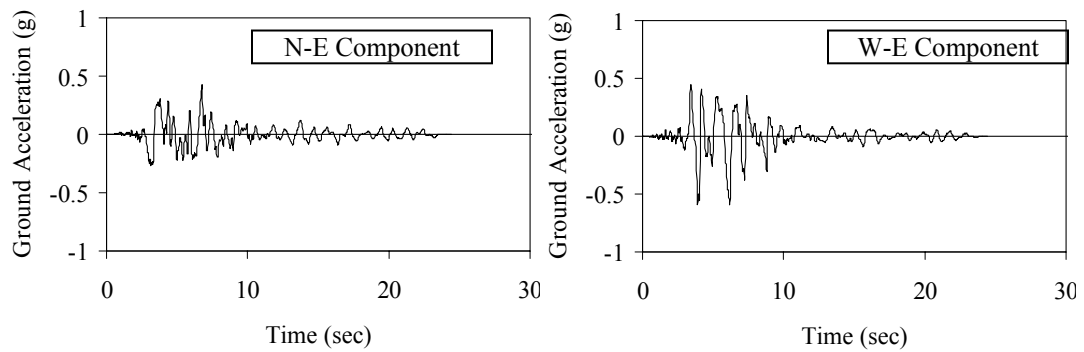


Figure 5.4 Accelerograms recorded at the Jensen Filter Plant Station during the 1994 quake (data source: <http://peer.berkeley.edu>)

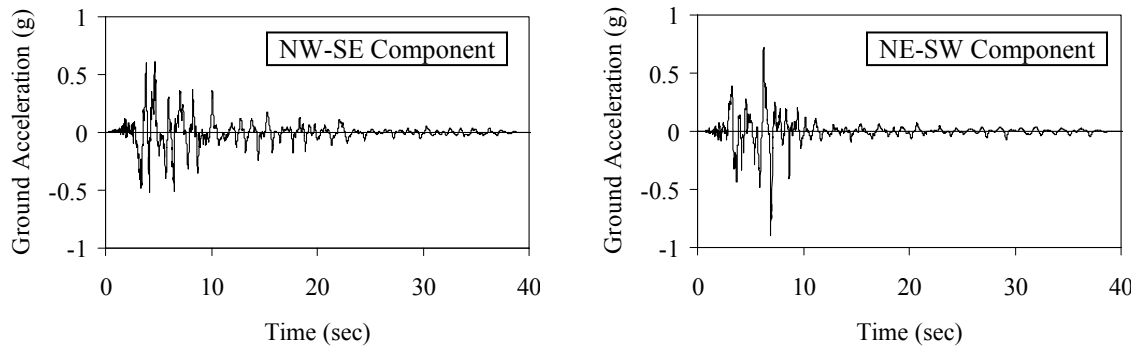


Figure 5.5 Accelerograms recorded at the Sylmar Converter Station during the 1994 quake (data source: <http://peer.berkeley.edu>)

5.3. Topographic Setting

The study site is located within a relatively flat area at the toe of mountains in the North. Figure 5.6 shows a slope map derived from Digital Elevation Model (DEM) available at the USGS website (<http://www.usgs.gov/>). The original DEM file includes elevation data for a ten-by-ten-meter grid, which fully covers the study site. A commercial program, ESRI ArcMap with the extension of spatial and geo-statistical analysis, generated the slope map for ten-by-ten-meter grid using the DEM file. This slope map was re-sampled into a twenty-by-twenty-meter grid (Figure 5.6) for the subsequent analysis which will be presented later. According to this map, the majority of the site lies in gently sloping areas with slope less than 5%. The only exception is the northwestern portion of the Joseph Jensen Filtration Plant, which is situated on hilly areas with slope more than 10 %.

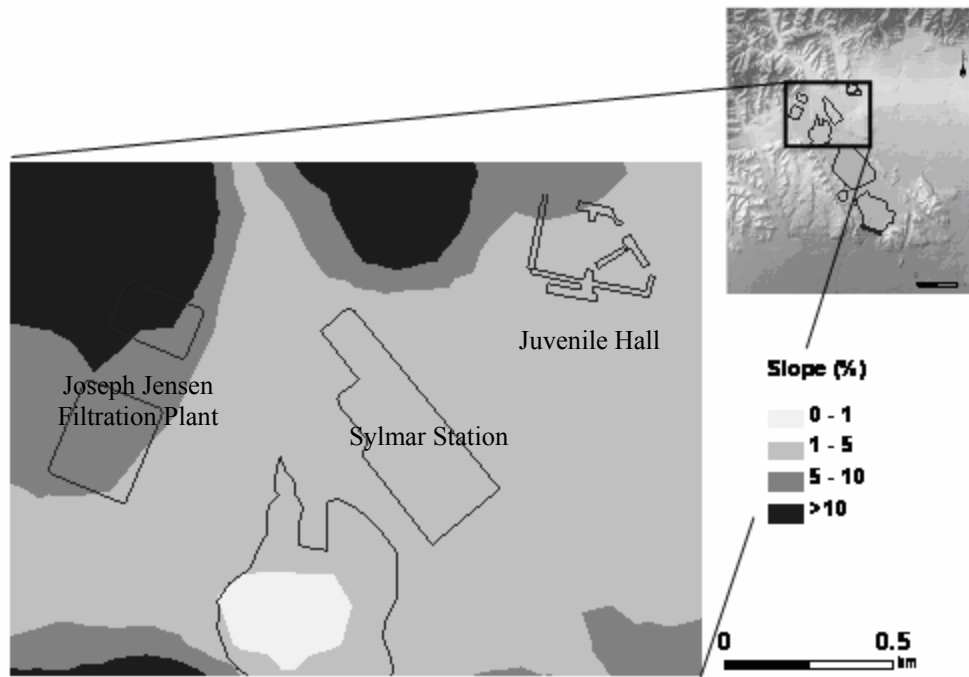


Figure 5.6 Slope map of the study site

5.4. Subsurface Soil Conditions

5.4.1. Regional Geology

Figure 5.7 shows the regional geology setting of the VNC vicinity. The majority of the study site situates on areas underlain by artificial fills and young alluvium. Those soil deposits are susceptible to liquefaction if shallow ground water level is encountered. The only exception is the northwestern portion of the Joseph Jensen Filtration Plant, in which Saugus formation is recognized and shallow bedrocks was encountered in geotechnical drilling boreholes conducted in the past.

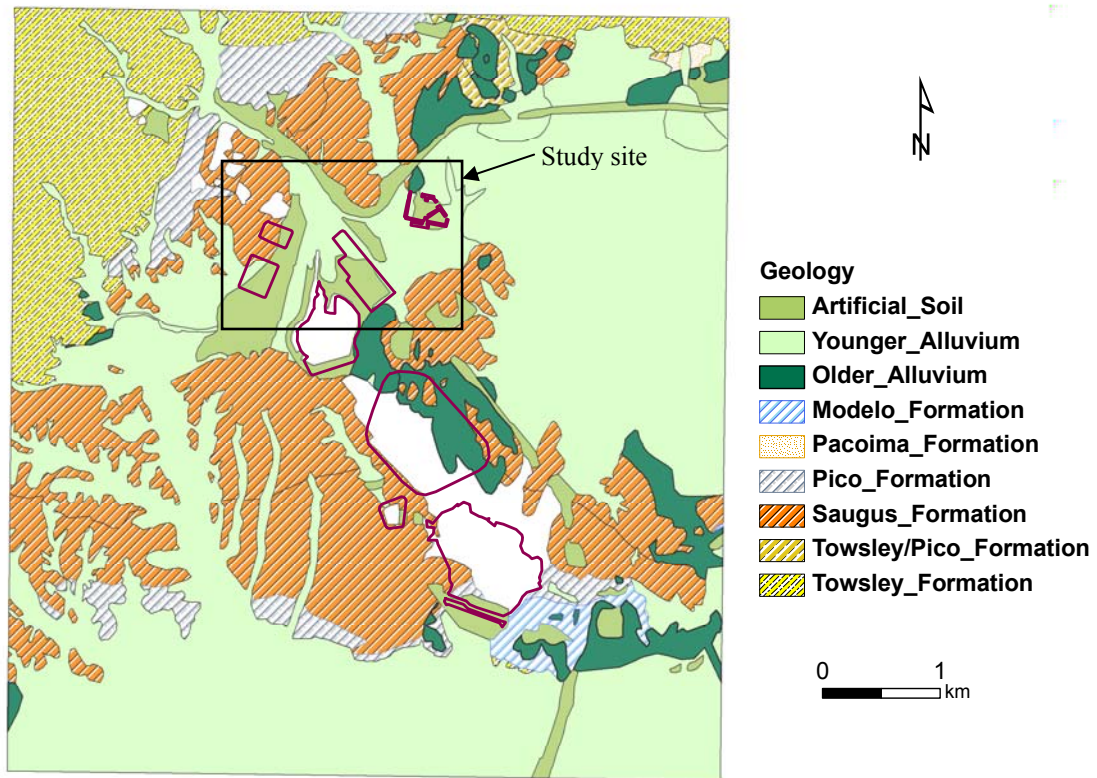


Figure 5.7 Geologic setting in the VNC vicinity

5.4.2. Geotechnical Investigation Data

Other colleagues (e.g., Hu 2003) accomplished the major work on the collection and compilation of geotechnical investigation data into the USC database. Figure 5.8 shows the spatial distribution of geotechnical data relevant to the study site, which is included in the database. They were developed from two types of geotechnical field borings: SPT (Standard Penetration Test) borings and CPT (Cone Penetration Test) borings. Before in-depth data analysis, data consistency was checked in this present study in order to ensure the data integrity.

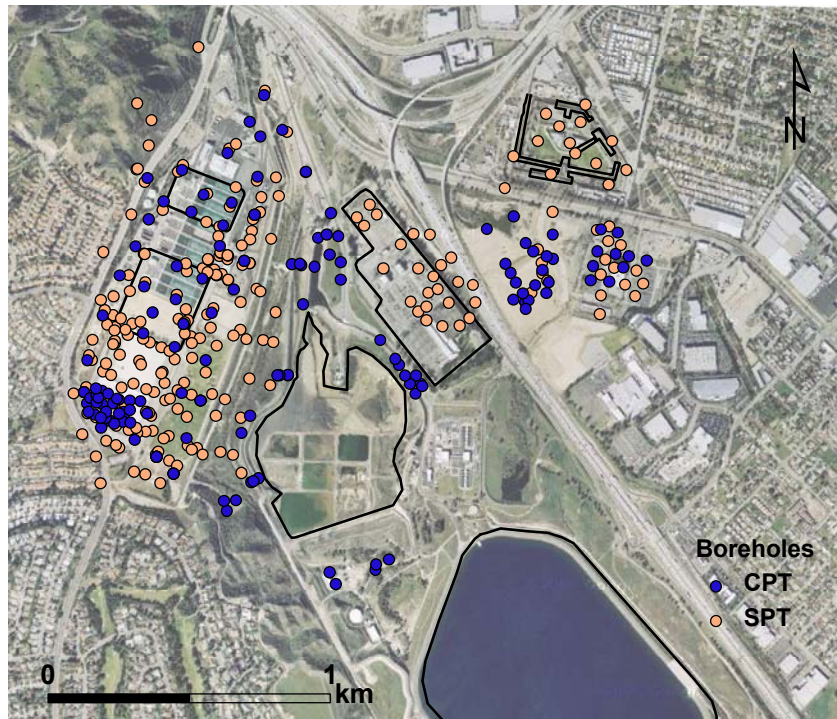


Figure 5.8 Spatial distribution of available geotechnical borings

Figure 5.9 and Figure 5.10 classify the geotechnical data in terms of data providers and drilling years, respectively. Those data were obtained from different agencies that might use different equipments, measure systems and analysis procedures. Special care needs to be taken while converting data between different measure systems, for instance, when calculating N_{160} from N -value obtained from non-standardized sampling procedures. As suggested by Figure 5.10, CPT tests were performed from 1984 to 1995, during which no remarkable alternation took place in the study site due to construction and natural hazard. In the present study, those CPT data were used as major sources for characterizing the site conditions corresponding to the 1994 earthquake, whereas those SPT data were used as supplemental information while estimating the ground water level in the past.

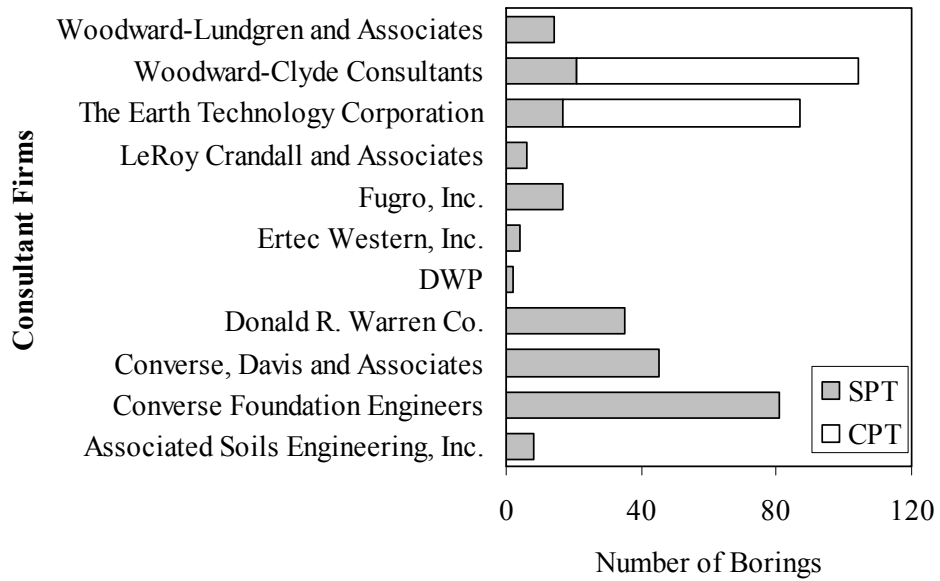


Figure 5.9 Consultant firms involved in collection of geotechnical boring data

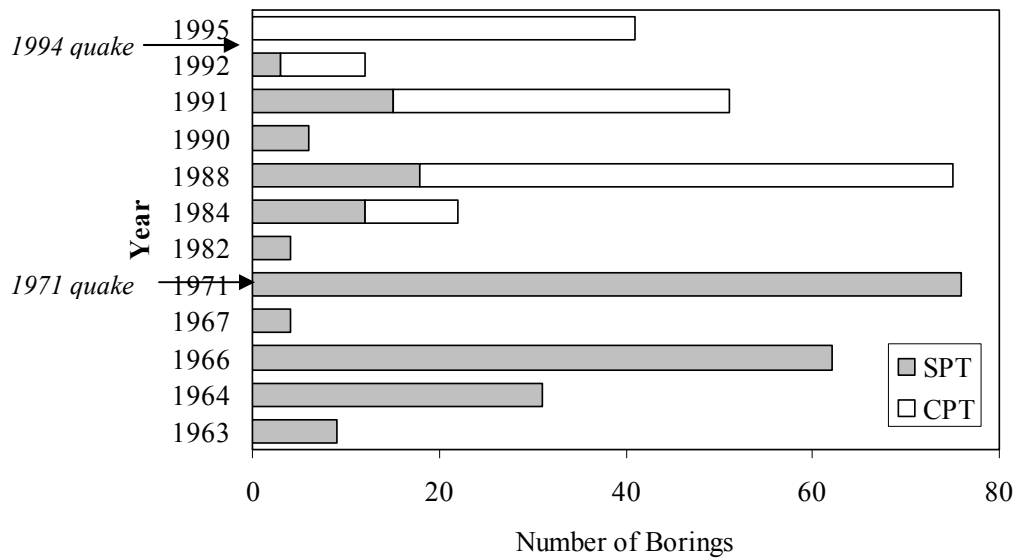


Figure 5.10 Drilling year of geotechnical boring data

5.5. Ground Water Level

Ground water level (GWL) was not been measured or detected in every available geotechnical boring. Fortunately, the unknown GWL can be interpolated at the CPT test locations from nearby measurements using geo-statistical approaches. Considering the variation of GWL over years, available GWL measurements were divided into two groups, one for the 1971 condition, and the other for the 1994 condition.

Figure 5.11 shows a prediction map of GWL for the 1994 earthquake. It was developed from a few available GWL measurements obtained by CPT or SPT tests in the past. The labeling numbers at the test locations correspond to the values of the ground water depth below the ground surface. The ground water depth ranges from 11 to 18 meters in the Jensen Filtration plant, and from 4 to 7 meters near the Juvenile Hall. It reaches the lowest level along the perimeter of the lower Van Norman Lake basin, and the by-pass channels between the Joseph Jensen Filtration Plant and the Sylmar Converter Station, ranging from zero to 4 meters.

For comparison, another prediction map (see Figure 5.12) was produced for the 1971 earthquake as well. The comparison shows that the ground water is deeper in 1994 than in 1971, particularly around the perimeter of the lower Van Norman lake basin, where a reservoir was located when the 1971 earthquake struck the site. The variation of ground water level could be caused by reservoir relocation. It could be one of the reasons that the study site received less liquefaction-related ground failures in the 1994 earthquake than in the 1971 earthquake.

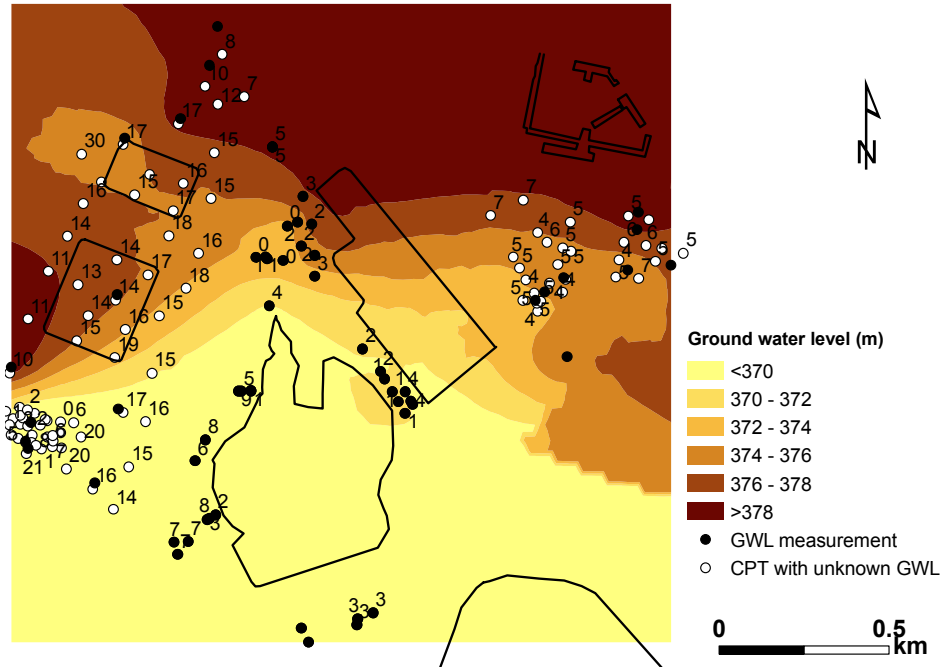


Figure 5.11 Interpolated GWL map of the 1994 earthquake; labeling numbers are the ground water depth in meters below the ground surface

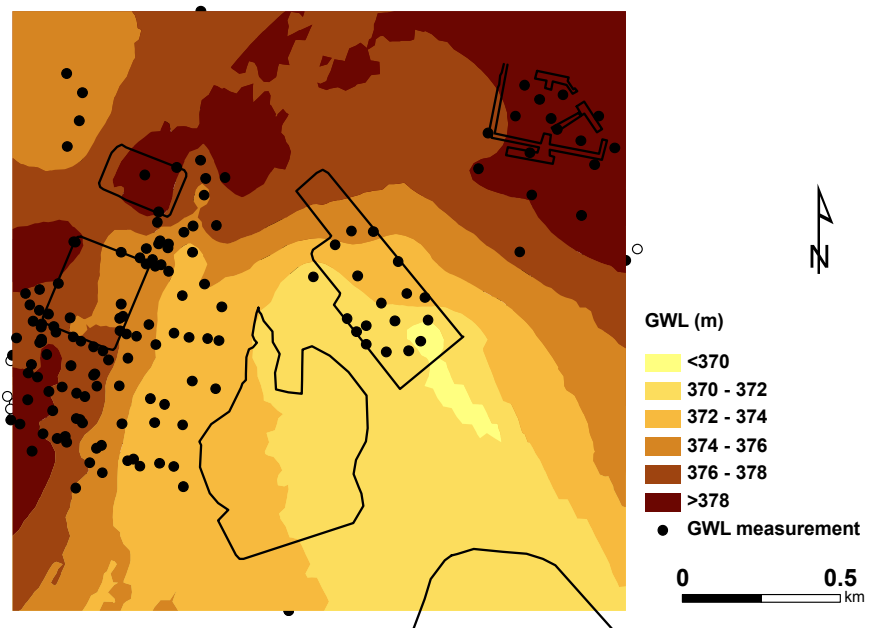


Figure 5.12 Interpolated GWL map of the 1971 earthquake;

5.6. Liquefaction Severity Assessment

Prior to the analysis of liquefaction-induced deformations, the liquefaction severity was evaluated under the conditions of the 1994 earthquake. Liquefaction potential categories developed by Sonmez (2003) was adopted in this study. Figure 5.13 shows an example of *LPI* calculation from an individual CPT test. The color-coded soil strata and *CSR/CRR* chart indicate that liquefiable soils range from 3 to 4.5 meters and from 7 to 8 meters below the ground surface at that particular location. The *LPI* sums up to be 11, inferring “High” potential to liquefaction for that specific soil profile.

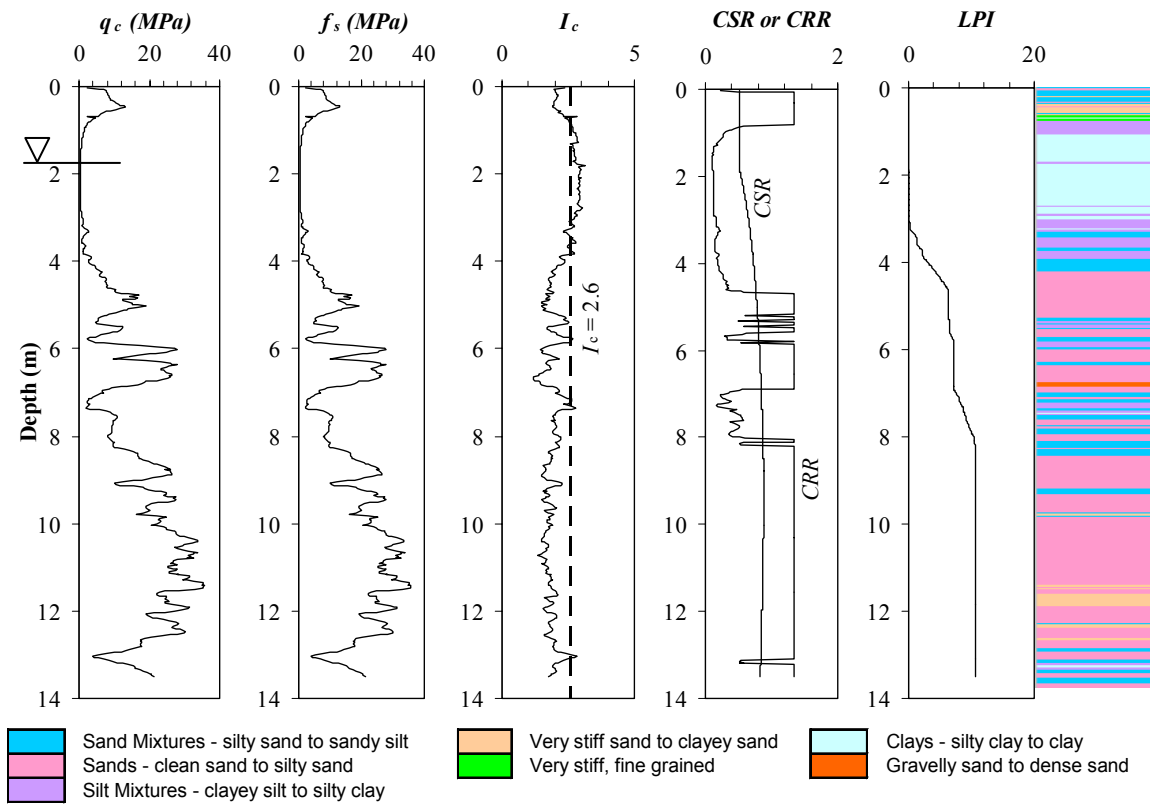


Figure 5.13 An example of *LPI* calculation

The calculation results of all other CPT tests are provided in Appendix A. The maximum *LPI* is 18. Figure 5.14 shows a map of *LPI* developed from all available CPT tests using geo-statistical interpolation approach (e.g., Kriging method). CPT test locations are depicted as red dots, whose sizes vary proportionally to the *LPI* values computed at the locations following the procedures illustrated in Figure 5.13. As shown in the map, high severity of liquefaction appears in the zone between the Joseph Jensen Filtration Plant and the Sylmar Converter Station, and the severity level decreases to the west and to the east. To some extent, an agreement is found between the high severity zone and the areas with larger deformations up to 120 cm along the by-pass channels.

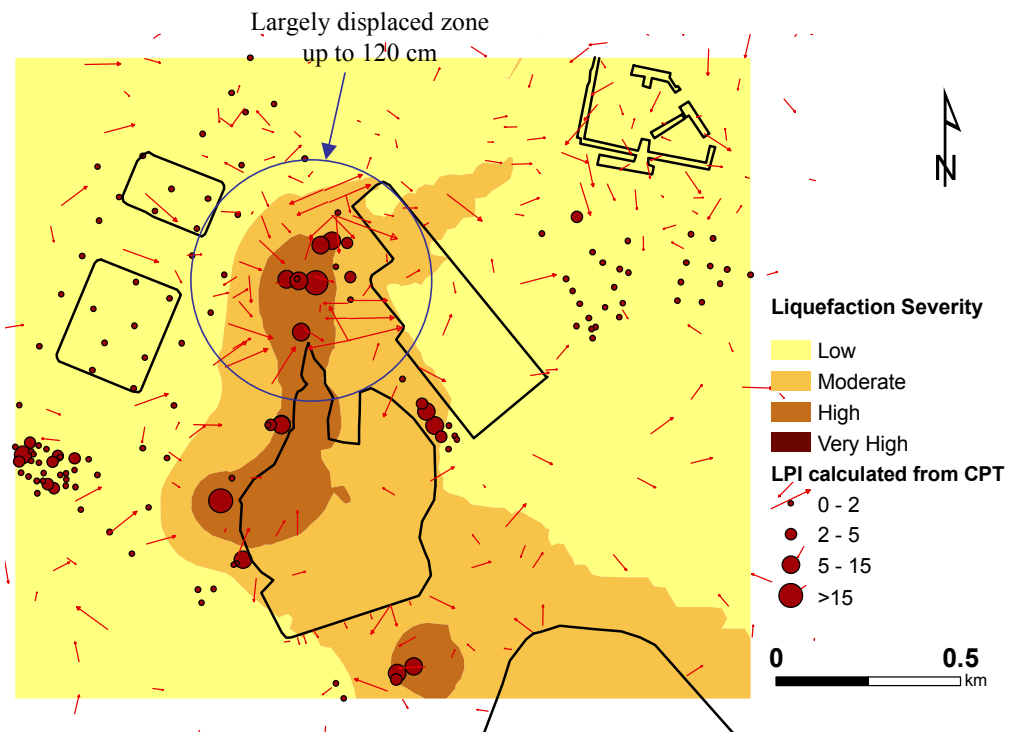


Figure 5.14 Spatial distribution of *LPI* showing the liquefaction severity

5.7. Evaluation of Liquefaction-Induced Lateral Deformations

This section is to scrutinize three existing models based on case histories for estimating liquefaction-induced lateral ground deformation on regional scale.

5.7.1. Youd et al. (2002) Model

As reviewed in section 2.6, Youd et al. model (2002) is a MLR model depending on three parameters of soil properties: T_{15} , F_{15} and D_{5015} , which require values of N_{160} along the vertical soil profile. Using the correlation between CPT test data and SPT data, equivalent values of N_{160} can be compute from CPT test results following the procedure described in section 2.4. Figure 5.15 shows an sample profile of N_{160} that was calculated from a single CPT test using Anagnostopoulo et al. correlation (2003) reviewed in section 2.4 (see Equation 2.11 and 2.12). As shown in Figure 5.15, the average grain size D_{50} ranges from 1 to 2 millimeters, and N_{160} is lower than 15 within depth intervals ranging from 1 to 5 meters, and from 7 to 8 meters.

The fine content FC was computed from the values of the soil behavior index I_c (defined in Equation 2.7). In the example of Figure 5.15, FC is over 50% within a depth interval ranging from 0.5 to 4 meters below the ground surface, inferring a clayey layer near the ground surface. These results are consistent with the soil strata shown in Figure 5.13.

CSR and CRR were computed based on the equivalent N_{160} values derived from the CPT test results, and compared with the CSR/CRR chart directly developed from CPT test results (see Figure 5.13). The comparison shows a good agreement in general.

T_{15} was computed from the cumulative thickness of liquefiable soil deposits with N_{160} lower than 15 and FC less than 15%, below the ground water level and less than 20 meters deep. In the example of Figure 5.15, the value of T_{15} is approximately 0.9 meter. The average mean grain size D_{5015} and average fine content F_{15} within the interval of T_{15} are 0.7 mm and 12%, respectively.

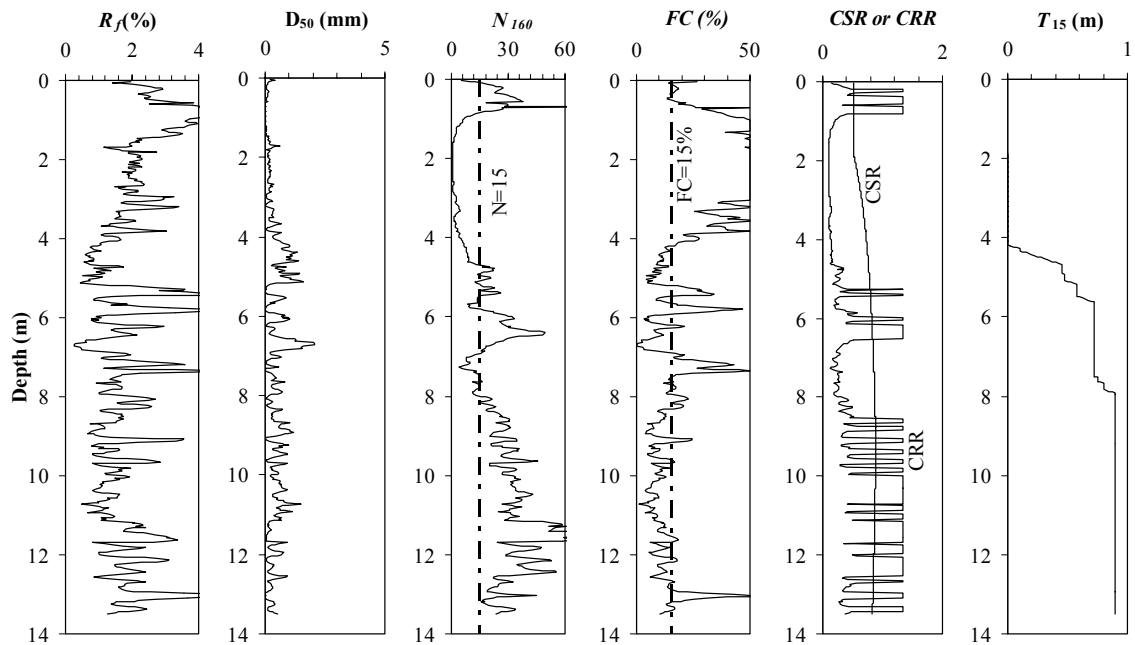


Figure 5.15 An example for calculating T_{15} from CPT test results

Calculation results of T_{15} are tabulated in Appendix A for all available CPT tests. Figure 5.16 shows a map of T_{15} interpolated from all those calculated values. The locations of CPT tests are represented as dots, whose sizes vary proportional to their T_{15} values. Those dots are also labeled with the values of F_{15} followed by D_{5015} . F_{15} ranges from 10% to 14%, while D_{5015} ranges from 0.7 to 2.7 millimeters. As shown in the map, the maximum

T_{15} is 1.2 meters located in the west of the upper Van Norman Lake basin. The second highest value situates between the Joseph Jensen Filtration Plant and the Sylmar converter Station along the by-pass channel. T_{15} exhibits negligible values within the Joseph Jensen Filtration Plant.

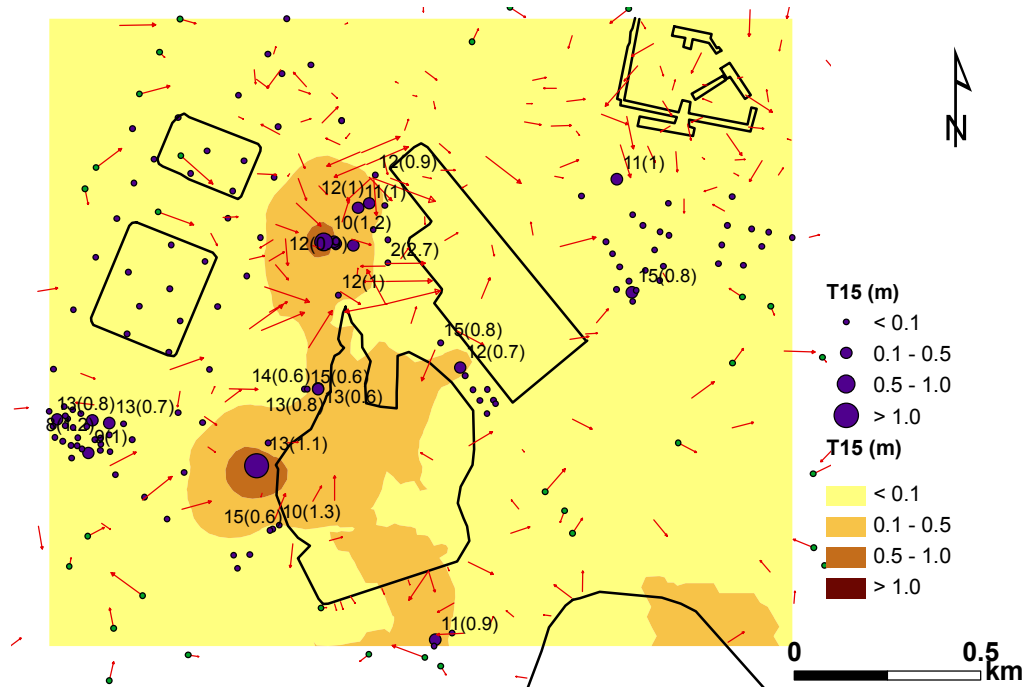


Figure 5.16 T_{15} map showing the liquefiable thickness; dots labeled with F_{15} values in percentage followed by the D_{5015} values in mm

Figure 5.17 shows a map of liquefaction-induced lateral deformations based on Youd et al. model (2002). The predicted deformations are in an order of centimeters. The maximum displacement is about 8 centimeters along the by-pass channels between the Joseph Jensen Filtration Plant and the Sylmar converter Station. Calculated

displacements are lower than the actual measurements, which reach 120 centimeters in the maximum.

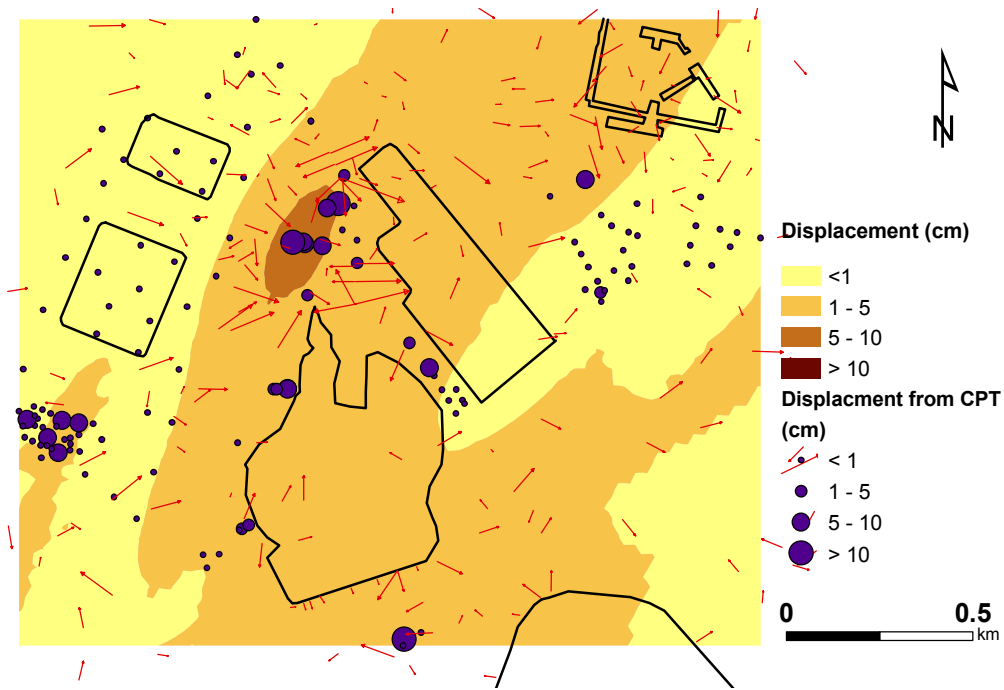


Figure 5.17 Predicted lateral ground deformations based on Youd et al. (2002) model

5.7.2. Bardet et al. (2002) model

Figure 5.18 shows a map of liquefaction-induced lateral deformations predicted based on Bardet et al. (2002) model using the derived T_{15} map shown in Figure 5.16. Similar to the map developed by Youd et al. model (2002), the predicted displacements based on Bardet et al. (2002) model are in an order of centimeters as well. The maximum displacement reaches about 12 centimeters along the by-pass channel between the Joseph Jensen Filtration Plant and the Sylmar converter Station..

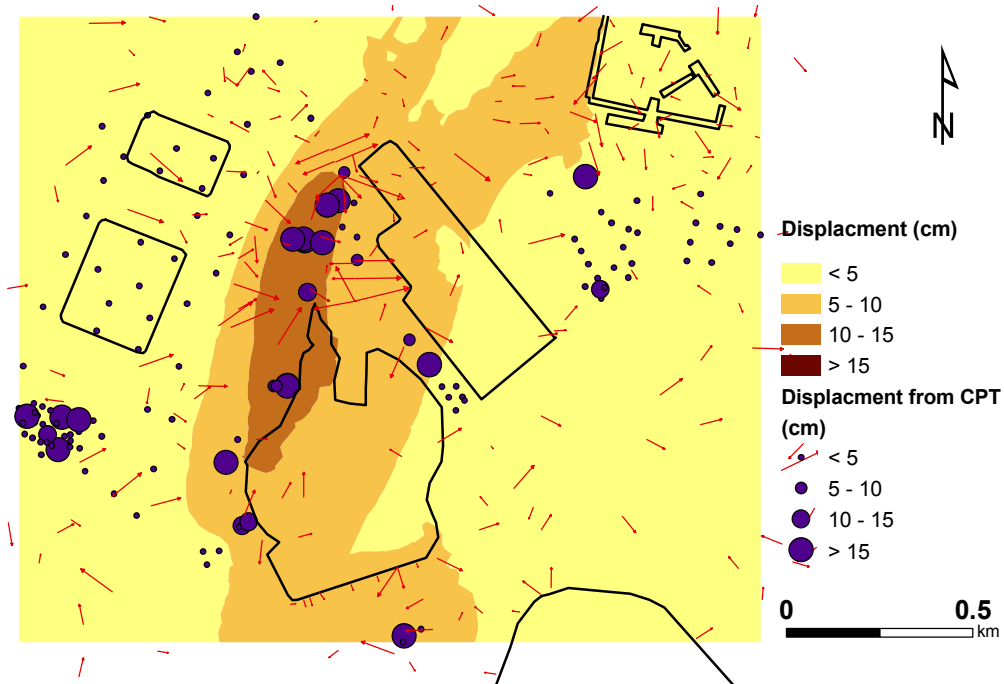


Figure 5.18 Predicted lateral ground deformations based on Bardet et al. (2002) model

5.7.3. Zhang et al. (2004) model

Figure 5.19 shows a map of lateral deformations derived from Zhang et al. (2004) model. The locations of CPT tests are represented as dots, whose sizes vary proportionally with the calculated values of *LDI* ranging from 10 to 150 centimeters. High *LDI* values appear between the Jensen Filtration Plant and the Sylmar Converter Station. In contrast to the results based on the two previous models, Zhang et al. (2004) model produced larger displacements that are in an order of tens of centimeters. The maximum displacement reaches 150 centimeters. These results have magnitudes comparable to the actual measurements.

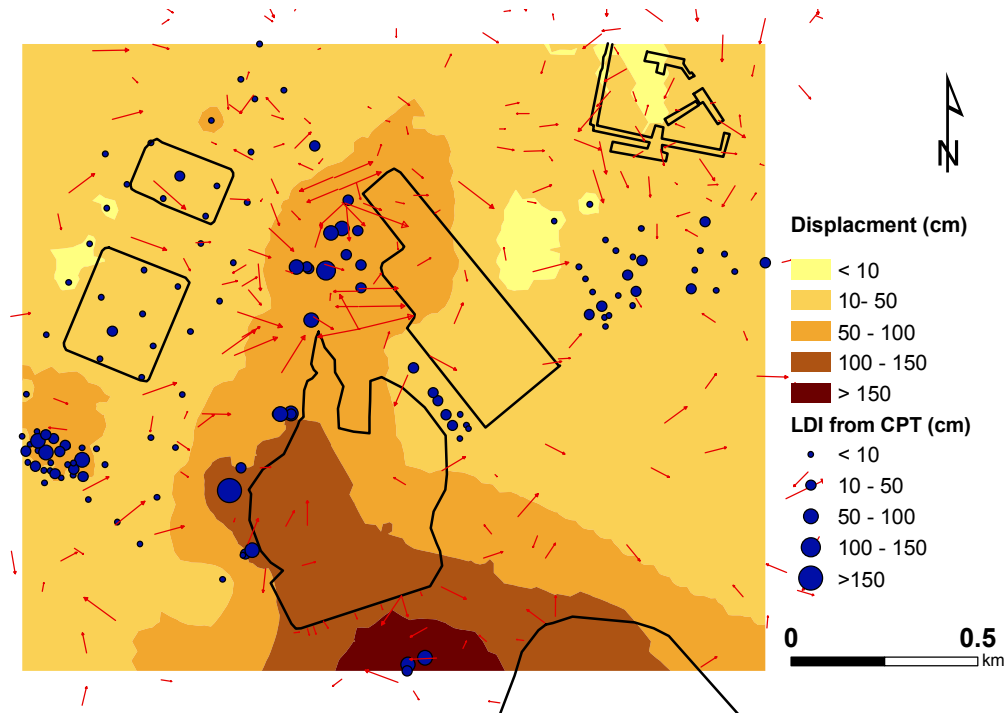


Figure 5.19 Predicted lateral ground deformations based on Zhang et al. (2004) model

5.8. Summary

In this case study, maps of liquefaction-induced lateral ground deformations were developed from three different existing models based on case histories. Those maps showed similar spatial pattern of deformation distributions on large scale. They were compared with the actual measurements. In the modeled results, in agreement with the field observations, larger displacements appear in a narrow zone along the by-pass channels between the Joseph Jensen Filtration Plant and the Sylmar Converter Station. However, the three models are short in providing accurate amplitudes of deformations. Youd et al. (2002) model and Bardet et al. (2002) both provided deformations in an order

of centimeters, lower than the actual measurements, whose maximum values reaches up to 120 centimeters. Zhang et al. (2004) model produced deformations comparable to the actual measurements. There is a growing demand for developing new models that can collaborate more physical mechanism and better predict liquefaction-induced lateral ground deformations on large scale.

This case study is preliminary and provided a rough comparison among different models. The ground geometry was derived from a DEM model without differentiating free face conditions and gently sloping ground conditions. Computations were presented only for gently sloping ground. Further study can be performed while distinguishing liquefaction-induced local deformations and overall tectonic movements.

Chapter 6. Motions of Gently Sloping Ground during Earthquakes

This chapter continues the work presented in Chapter 5 and aims to improve the existing models for predicting liquefaction-induced lateral ground deformations on regional scales. This chapter extends a sliding block model to gently sloping ground that has become unstable due to temporarily losses in shear strength after liquefaction. The fundamental questions to be answered in this chapter are: (1) whether or not earthquakes contribute to the motions of mass that has become unstable; and (2) how to characterize the earthquake contributions. The ultimate goal of this chapter is to gain insights into the new generation models for predicting liquefaction-induced lateral ground deformations. Part of this chapter has been submitted for publication (Bardet and Liu 2008).

6.1. Model for Gently Sloping Ground

Figure 6.1 proposes a physical model for studying the motions of gently sloping infinite ground. The failure plane is at depth H parallel to the ground surface with an inclination angle θ . The unstable mass above the failure plane is represented by a vertical slice with mass m subjected to the gravity force W , friction force R and normal force N . The lateral forces acting on the vertical sides cancel each other in case of infinite ground. The magnitude and direction of force R may vary with time depending on how the unstable

mass moves relative to the ground. For homogenous ground of unit weight γ , the static stresses are:

$$\begin{cases} \sigma_o = \gamma H \cos^2 \theta \\ \tau_o = \gamma H \cos \theta \sin \theta \end{cases} \quad (6.1)$$

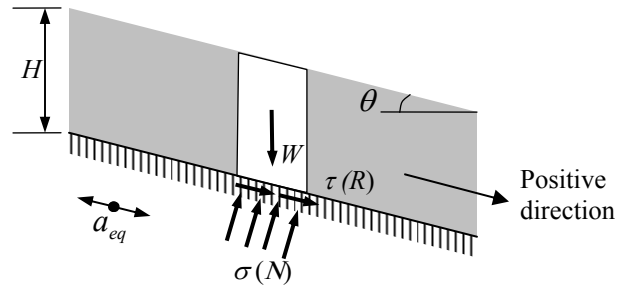


Figure 6.1 Geometry, forces and stresses of an idealized gently sloping ground

The seismic acceleration a_{eq} is assumed parallel to the ground surface, and the effects of vertical accelerations are assumed negligible for small ground inclination. During earthquakes, the normal stress σ_d remains constant (i.e., $\sigma_d = \sigma_0$) whereas the shear stress τ_d varies with time and depends on the constitutive behavior of soil deposits. In case of a rigid - perfectly plastic interface under the moving mass (Figure 6.2), τ_d can be described in term of the relative mass velocity v_r (relative to ground velocity) and a constant residual shear strength τ_f as follows:

$$\tau_d = \tau_f \text{sign}(-v_r) \quad (6.2)$$

where $\text{sign}(\cdot)$ is the sign function (i.e., 1 when $x > 0$ and -1 when $x < 0$). Figure 6.3 represents the assumed variation of shear strength in the physical model, which idealizes the experimental observations in Figure 2.1. The shear strength, initially larger than τ_0 , is allowed to drop to τ_f below τ_0 during a time interval, and to re-increase to its previous level. The factor of safety, which is initially above 1, decreases to a value smaller than 1 at the onset of instability and then regains its initial value. This sudden step variation in shear strength, which simplifies the behavior shown in Figure 2.1, is convenient to examine the effects of instability on the sliding mass motions. It may also be used to account for instability generated by other physical phenomena.

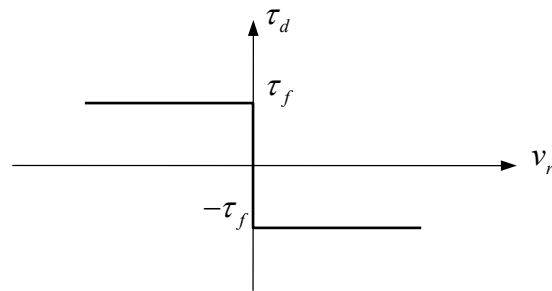


Figure 6.2 Shear resistance of rigid - perfectly plastic interface

The dynamic equilibrium equation of mass m parallel to the slope (Figure 6.1) is:

$$ma = W \sin \theta + R \quad (6.3)$$

where a is the mass acceleration. Equation (6.3) can be written as:

$$a = g \sin \theta \left(1 + \frac{\tau_d}{\tau_0} \right) \quad (6.4)$$

Combination of Equations (6.2) and (6.4) yields:

$$a = g \sin \theta [1 - \text{sign}(v_r) F_i] \quad (6.5)$$

where F_i is defined as the ratio of residual shear strength τ_f to static shear stress τ_0 (i.e., $F_i = \tau_f / \tau_0$), which is different from the static factor of safety F_s (Figure 6.3).

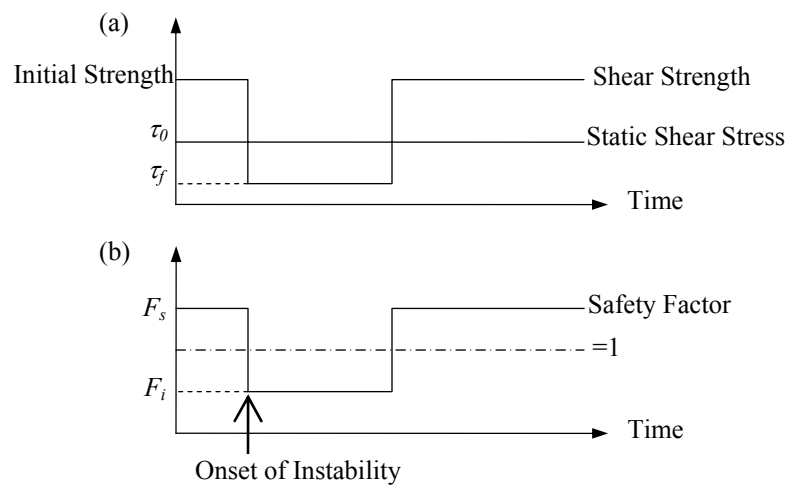


Figure 6.3 Instability due to loss in shear strength: (a) time histories of static shear stress and shear strength; and (b) time history of safety factor varying between F_s and F_i

When the groundwater reaches the ground surface, and the slope has a gentle inclination, F_i can be approximated as follows:

$$F_i = \frac{\gamma_{sat} - \gamma_w}{\gamma_{sat}} \frac{\tau_f / \sigma'_v}{\sin \theta \cos \theta} \approx \frac{\tau_f / \sigma'_v}{2\theta} \quad (6.6)$$

where σ'_v is the vertical effective stress; γ_{sat} is the saturated soil unit weight; γ_w is the water unit weight; and θ is in radian. Equation (6.6) is useful to define a range of variation for values of F_i . The values of τ_f / σ'_v in liquefied soils have been found to range from 0.01 to 0.2 using numerous back-calculations of liquefied slopes (e.g., Olson and Stark 2002). F_i becomes smaller than 1 when τ_f / σ'_v is less than 2θ , and can become as small as 0.06 for extreme cases, e.g., $\tau_f / \sigma'_v = 0.01$ and $\theta = 5^\circ$.

The first and second order integrations of Equation (6.5) lead to the velocity and displacement of the unstable mass, respectively. When $v_r = 0$ in Equation (6.5), a and τ_d are calculated as described in Figure 6.4, which illustrates the procedure implemented in Matlab using well-known time-integration algorithms (e.g., Hughes 2000).

The physical model of Figure 6.1 differs from other Newmark-type models in several aspects. It calculates the absolute motion of the unstable mass, whereas other models depict its relative motion. Both approaches lead to identical permanent ground deformations, provided that earthquake shakings are zero-mean process. While other models discard instability ($F_i < 1$) due to their reliance on positive yield accelerations, the present model remains valid for any values of F_i . The present model also considers two-

way sliding, a relevant feature in gently sloping ground which may move either upslope or down-slope during earthquake shakings.

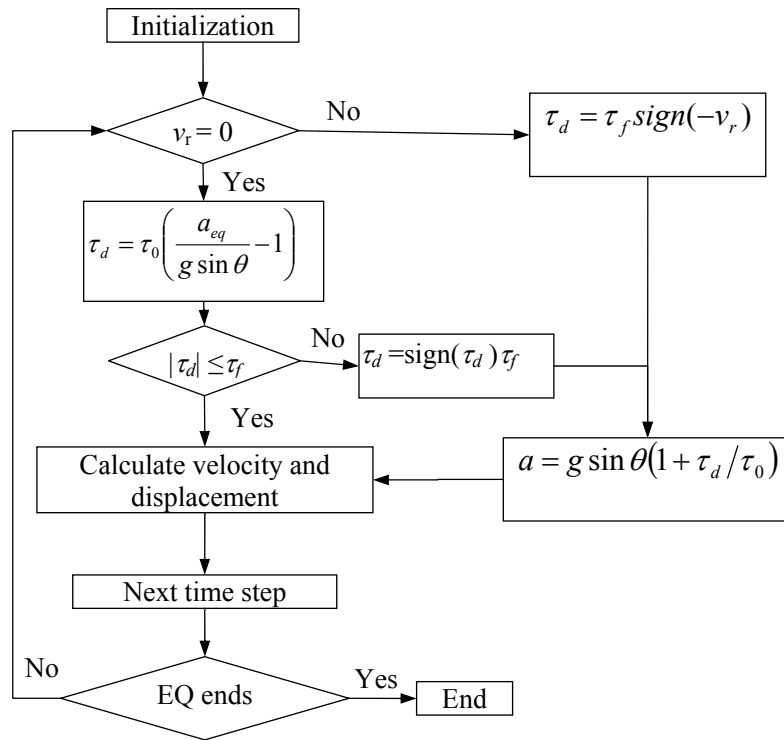


Figure 6.4 Algorithm for calculating cumulative displacement

6.2. Seismic Deformation of Statically Unstable Sloping Ground

The capability of the proposed model can be illustrated for a specific earthquake and a few cases of shear strength reduction. Figure 6.5 shows the time history of ground acceleration in use, which was recorded at Rinaldi Receiving Station during the 1994 Northridge, California, earthquake. The ground acceleration is assumed parallel to the

ground surface. For illustration purposes, the shear strength is arbitrarily assumed to drop instantly at time $t_i = 2$ seconds after the beginning of the earthquake, and to remain constant after t_i , resulting a constant value of F_i . Time t_i represents the time required for the soil either to liquefy completely or to reach a constant pore pressure level. Particular values of time t_i can be assessed using various liquefaction occurrence models (e.g., Kayen and Mitchell 1997; Seed and Idriss 1971; Youd et al. 2001).

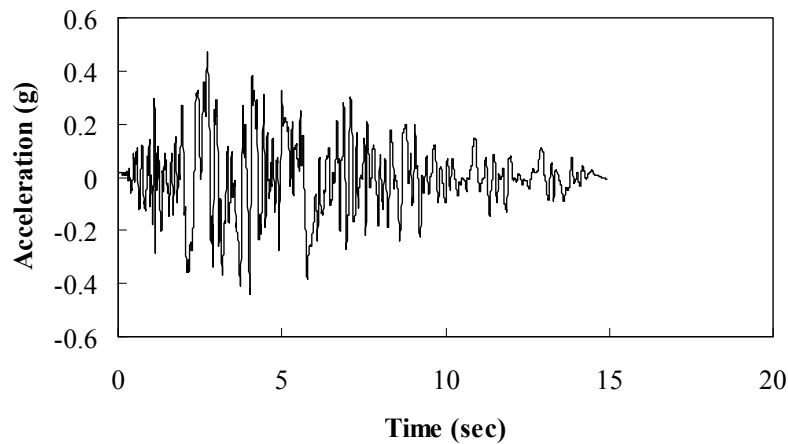


Figure 6.5 Time histories of earthquake acceleration recorded at Rinaldi Receiving Station during the 1994 Northridge, California, earthquake (data source: <http://peer.berkeley.edu>)

Figures 6.6 to 6.8 present the results for a 5° slope with a reduced shear strength which remains constant until the end of the duration of significant strong motions t_S (after Trifunac and Brady 1975). Figure shows the time histories of the ratio of the dynamic to static shear stress (i.e., τ_d/τ_0) when $F_i = 2, 0.9$ and 0.4 . The ratio τ_d/τ_0 is bounded by $\pm F_i$ since τ_d is controlled by the maximum available shear strength τ_f . For $F_i = 2$, τ_d/τ_0

fluctuates a lot and changes sign frequently, which implies that the unstable mass switches frequently between upward and downward motions. Conversely, for $F_i = 0.9$, τ_d/τ_0 remains mostly $-F_i$ after the onset of instability, indicating that the mass is mostly subjected to upward resistance regardless of seismic shaking. When F_i decreases to 0.4, τ_d/τ_0 remains equal to -0.4 after the onset of instability; the mass is purely driven by gravity independently from earthquake shakings after it becomes unstable. In other words, the earthquake motions do not influence the permanent displacements after the shear strength drops below a certain level.

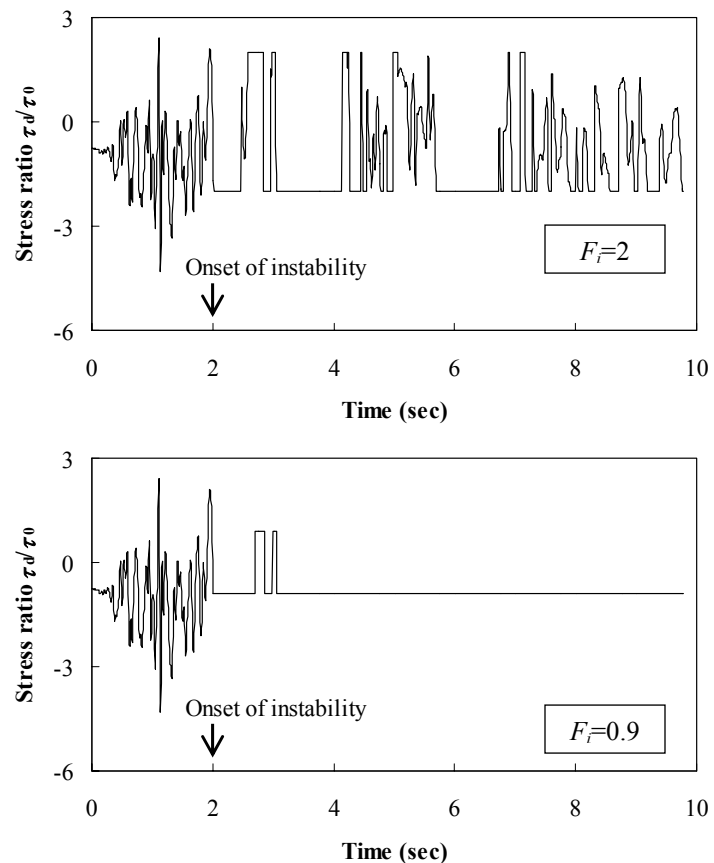


Figure 6.6 Time histories of stress ratio of a 5° slope when $F_i=2$, 0.9 and 0.4

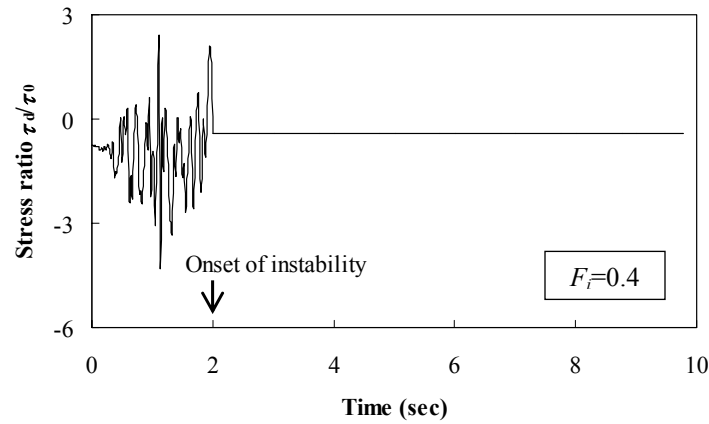


Figure 6.6 Continued

Figure 6.7 compares time histories of mass velocity and ground velocity for $F_i = 2$, 0.9 and 0.4. In contrast to stable ground (e.g., $F_i = 2$), the velocity of unstable ground (e.g., $F_i = 0.4$ and 0.9) increases monotonously and almost linearly with time. When $F_i = 0.9$ after the onset of instability, the mass slides down initially driven by gravity, independently of the ground shaking. When the ground velocity rises rapidly and overcomes the mass velocity, the ground drags the mass downwards and accelerates it until the mass velocity exceeds the ground velocity. Once the moving mass has become unstable, its velocity can be only increased by earthquake motions that are faster than the mass velocity; otherwise, the earthquake motions cannot affect the mass motion. For example, as shown in Figure 6.7, in the case of $F_i = 0.4$, the sliding mass has a velocity linearly increasing with time as if there were no seismic motion, and its displacement after the onset of instability solely results from gravity. These examples suggest that the mass motions after the onset of instability are not influenced by earthquake shakings for large reduction in shear strength,

while they may be significantly influenced by pulses of earthquake ground velocity for smaller reduction in shear strength.

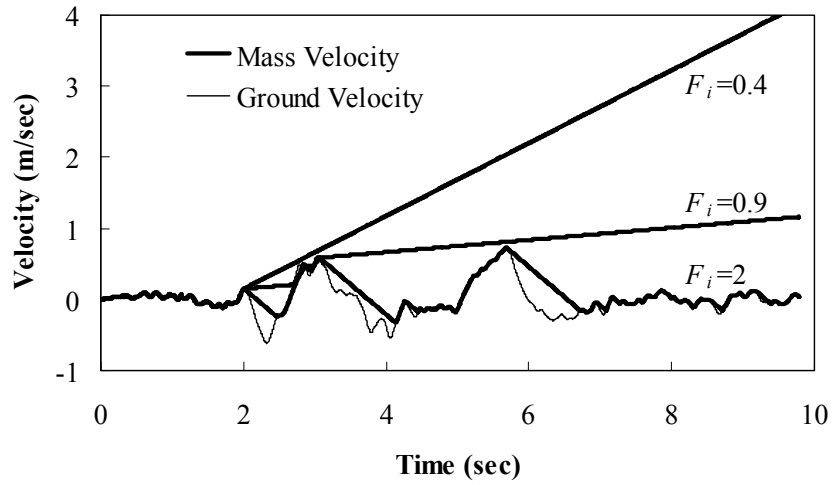


Figure 6.7 Time histories of mass velocity and ground velocity when $F_i = 2, 0.9$ and 0.4

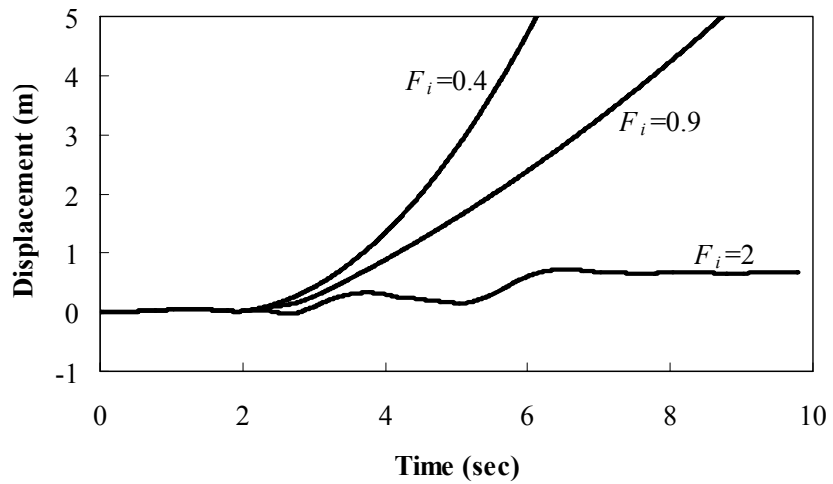


Figure 6.8 Time histories of mass displacement for $F_i = 2, 0.9$ and 0.4 corresponding to velocity of Figure 6.7

Figure 6.8 shows the time histories of displacements for stable mass (e.g., $F_i = 2$) and unstable mass (e.g., $F_i = 0.4$ and 0.9). The displacement for $F_i = 2$, which can also be described by Newmark model, eventually stops at the shaking end, whereas the displacement increases almost as a parabolic function of time and ends resulting in very large deformations when $F_i = 0.9$ and 0.4 .

6.3. Factors Controlling Motions of Unstable Sloping Ground

The physical model (Figure 6.1) is useful to analyze the factors influencing the deformations of unstable ground. As suggested in Figures 6.6 to 6.8, the mass displacements depend on slope inclination θ , reduction in shear strength F_i , timing of shear strength reduction t_i , and earthquake strong motions. θ is a controlling factor. In general, the steeper the slope, the larger are the gravity forces and resulting displacements. F_i and t_i also influence slope displacements. F_i and t_i are physical parameters related to residual shear strength and time of occurrence of liquefaction. Obviously larger and longer reduction in shear strength leads to larger permanent displacements. In general, earthquake strong motions affect the motions of unstable slopes in two ways: (1) they may trigger pore pressure buildups and possibly liquefaction; and (2) they may interfere with the movement of unstable mass. However, it is difficult to tell whether or not earthquake strong motions will influence the motions of sloping ground because seismic motions are largely stochastic.

Figure 6.9 illustrates two different definitions for characterizing the earthquake contributions to the motions of sloping ground. After the onset of instability, the unstable ground moves at a linearly increasing velocity (i.e., constant acceleration), and accelerates more when the underlying ground velocity exceeds their velocity. As shown in Figure 6.9, the total displacement D is obtained by integrating the velocity of the moving mass, i.e., Line A.

First definition (δ): The displacement δ_s resulting from instability is completely independent of earthquake motion (Line B). The corresponding velocity v_0 is zero at the onset of instability, and increases linearly with time (Line B) because the acceleration is constant. The associated unstable displacement δ_s is the area under Line B, which is independent of the earthquake motion. The earthquake contribution is $\delta = D - \delta_s$.

Second definition (δ'): The initial velocity v_0 of the moving mass is not necessarily equal to zero due to the earthquake motion at the onset of instability at time t_i . The corresponding velocity of the unstable mass corresponds to Line B' in Figure 6.9, which starts from v_0 at time t_i . The associated unstable displacement δ'_s is the area under Line B'. The earthquake contribution is $\delta' = D - \delta'_s$.

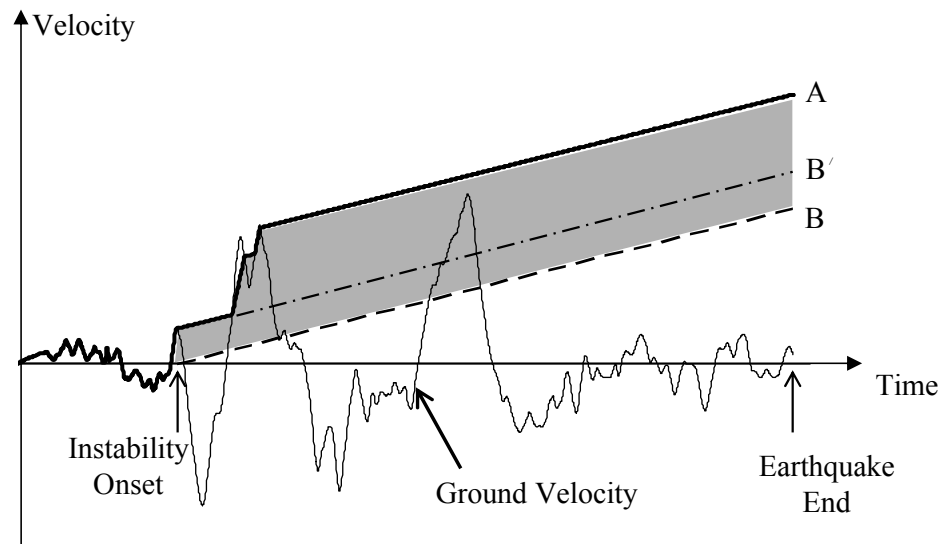


Figure 6.9 Definitions of earthquake contributions to unstable ground motions: δ - areas between Lines A and B; δ' - areas between Lines A and B'

The first definition assumes that the unstable displacement is completely independent from earthquake motions (i.e., v_0). The second definition is useful to understand whether or not unstable masses are affected by earthquake motions after they started moving downhill. Both definitions δ and δ' can be related by invoking that the unstable displacements δ_S and δ'_S are themselves related as follows:

$$\delta'_S = \delta_S + v_0(t_S - t_i) \quad (6.7)$$

where t_S is the time when the instability ends, and v_0 the ground velocity at time t_i . Both definitions have physical relevance and present slightly different perspectives in analyzing the effects of earthquake motions on unstable ground.

The primary question of the paper, i.e., “*Do earthquake transient shakings influence the motions of gently sloping ground that become temporarily unstable?*” can be investigated using the first definition, i.e., δ . It can be also rephrased differently using a secondary question: “*Once gently sloping ground has become unstable, can earthquake transient shakings still influence its motions?*” The second question requires using δ' instead of δ as the effects of initial earthquake velocity should be now excluded.

Both questions can be examined using a statistical approach applied to the definitions of earthquake contribution δ and δ' . To this effect, the following binary variable Y is introduced:

$$Y = \begin{cases} 1 & \text{if } |\delta| \geq \delta_0 \\ 0 & \text{if } |\delta| < \delta_0 \end{cases} \quad (6.8)$$

where δ_0 is the arbitrarily selected cutoff value below which the earthquake contribution δ can be neglected (i.e., $Y=0$). Equation (6.8), which applies to δ , can be readily adapted to δ' by using prime superscripts. Y is a random variable, and the likelihood for δ to exceed δ_0 (i.e., $Y=1$) can be defined using a probability function F . The conditional probability of $Y=1$ for a given state parameter X can be represented as:

$$\text{Prob}(Y = 1 | X) = F(X) \quad (6.9)$$

X may include a combination of independent physical parameters (e.g., θ , F_i). The functional form of $F(\cdot)$ is usually assumed and calibrated using regression analysis and maximizing the likelihood function (e.g., Greene 2000).

6.4. Probability for Earthquake Contribution δ

The probability function $F(\cdot)$ was determined using Monte Carlo realizations on 1062 accelerograms from the PEER (Pacific Earthquake Engineering Research, <http://peer.berkeley.edu/>) strong-motion database. The accelerograms included the horizontal components from 37 historical earthquakes with moment magnitudes M_w ranging from 4.7 to 7.4. Their PGA were larger than 0.1g, which is an approximate minimum PGA value to trigger liquefaction. During Monte Carlo simulations, the accelerograms were randomly selected, while the other parameters (i.e., θ , F_i , and t_i) were assumed continuously random with a uniform distribution within pre-defined ranges. The ranges of F_i , θ and t_i were $0 \leq F_i \leq 1$, $0 \leq \theta \leq 5^\circ$ and $0 \leq t_i \leq t_s$, respectively. For each scenario, random values of θ , F_i , and t_i were first generated, and Y was determined from the computed values of δ using a cutoff value δ_θ . Simulations included 30,000 scenarios that were divided into two Y -subsets (i.e. $Y=0$ and $Y=1$), and two Y' -subsets (i.e. $Y'=0$ and $Y'=1$).

Figures 6.10 and 6.11 show the histograms of input parameters for the entire dataset and subset $Y=1$ when $\delta_\theta = 1$ cm and $\delta_\theta = 10$ cm, and the empirical probability of $Y=1$, (i.e., p_1), which is the relative proportion of subset $Y = 1$ to entire data set. In general, the

empirical probability reflects the true probability when there are many data in a histogram bin; otherwise, it becomes less reliable. As shown in Figure 6.10, the probability p_I increases with Peak Ground Velocity (PGV) for both $\delta_0 = 1\text{cm}$ and $\delta_0 = 10\text{ cm}$, and is much less dependent on PGA and Arias Intensity. As shown in Figure 6.11, the probability p_I is independent on the physical parameters θ and F_i . Therefore, PGV is a better candidate for X , i.e., $X = \{PGV\}$. The probability function $F(\cdot)$ is assumed to be a Probit model, which is a common assumption for discrete random variables. Using the EasyReg program (Bierens 2007), the following model is obtained for predicting the probability that δ exceeds δ_0 :

$$F(PGV, \delta_0) = \Phi(1.43 \log_{10}(PGV) - 1.25 \log_{10}(\delta_0) - 0.524) \quad (6.10)$$

where $\Phi(\cdot)$ is the standard normal cumulative distribution function; PGV is in cm/s; and δ_0 in cm. As shown in Figure 6.10, the probability computed using Equation (6.10) fits well the empirical value p_I .

Figure 6.10 and Equation (6.10) are useful to answer the primary question, i.e., to determine the likelihood for earthquakes to contribute to the displacements of gently sloping ground beyond a selected threshold, i.e., 10 cm. For instance, an earthquake with $PGV = 60\text{ cm/s}$ has 80% chance to affect the displacement of gently sloping ground.

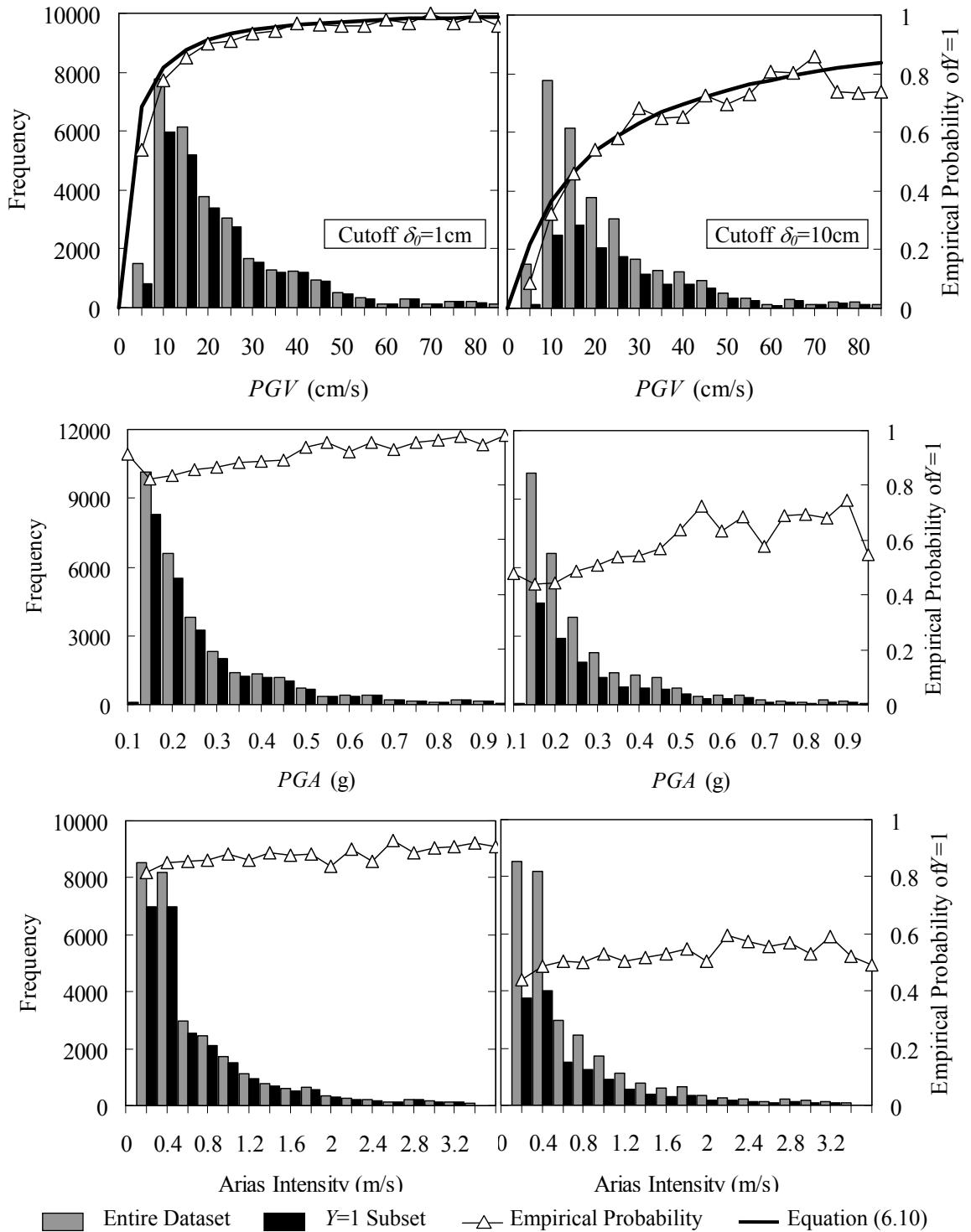


Figure 6.10 Histograms and empirical probabilities for PGV ; PGA ; and Arias Intensity when $\delta_0=1$ cm and 10cm (Y defined in Equation 6.8); earthquake data from PEER strong motion database, <http://peer.berkeley.edu/>

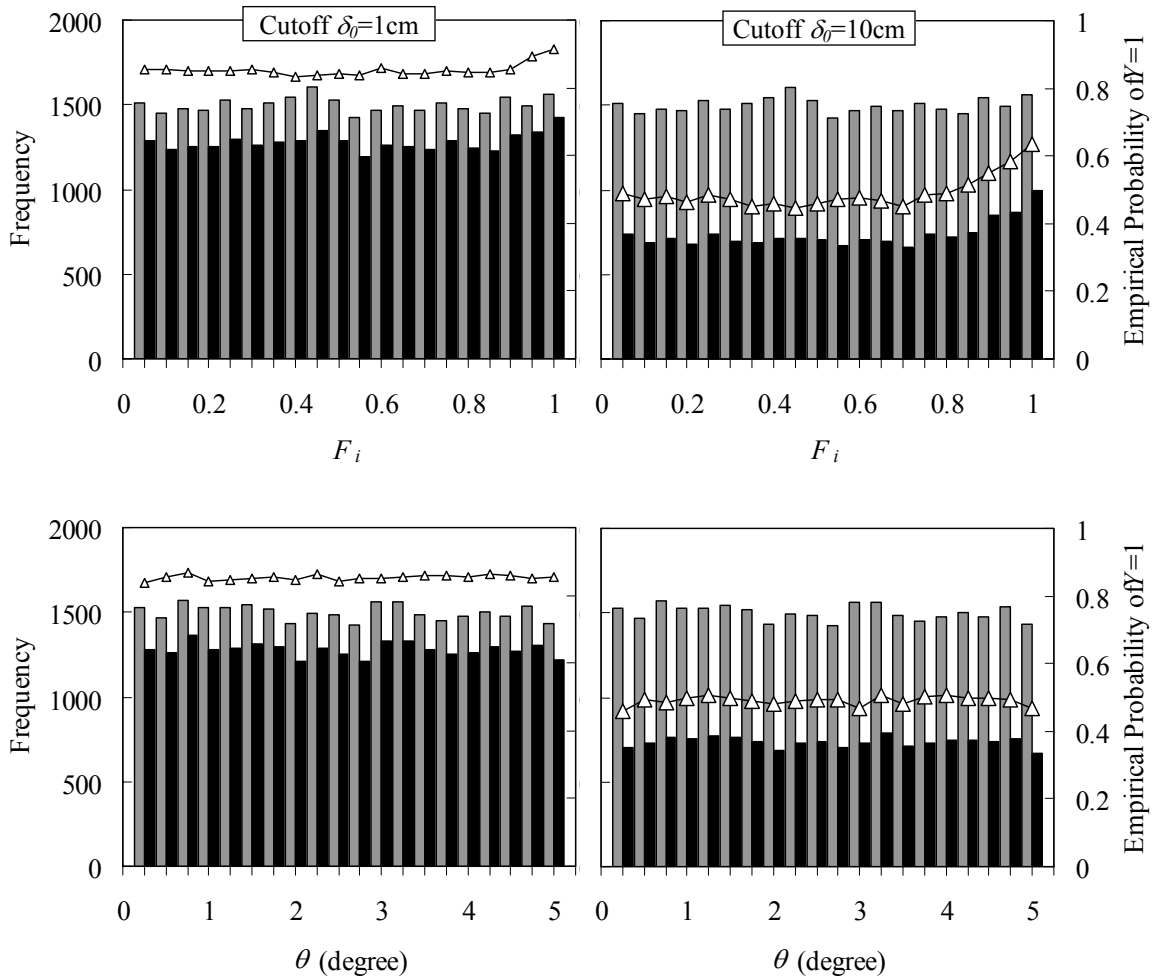


Figure 6.11 Histograms and empirical probabilities for parameters F_i and θ when $\delta_0=1$ cm and 10cm

6.5. Probability for Earthquake Contribution δ'

The analysis performed for the first definition of earthquake contribution δ can be applied to the second definition of earthquake contribution δ' . Figures 6.12 to 6.14 show the histograms of input parameters for the entire dataset and subset $Y=1$ when $\delta_0 = 1$ cm and

$\delta_0 = 10$ cm. They show results different from those in Figures 6.10 and 6.11. Figure 6.12 shows the histograms of seismic parameters PGV , PGA , and Arias Intensity. The empirical probability of $Y=1$ (i.e., p'_1) increases with PGV , similarly to p_1 ; for both definitions of earthquake contributions, PGV is likely to affect the displacement of gently sloping ground. Figures 6.12 and 10 show similar histograms for the entire data set, which is an obvious result. However, in contrast to p_1 , p'_1 depends on PGA and Arias Intensity as well as PGV . This result demonstrates the influence of accounting for the initial velocity v_0 at the onset of instability, and can be explained by invoking the fact that v_0 is related to PGV . Subtracting the primary PGV effects mobilizes the secondary effects associated with other variables e.g., PGA and Arias Intensity. In conclusion, PGV is a more relevant indicator for characterizing the potential contribution of earthquakes on displacements of gently sloping ground.

Figure 6.13 shows the histograms in terms of F_i and θ for the entire data set, subset $Y=1$, and the empirical probability p'_1 when $\delta_0 = 1$ cm and $\delta_0 = 10$ cm. In contrast to p_1 (Figure 6.11), the probability p'_1 depends on F_i and θ . Compared to δ , δ' depends more on the physical parameters F_i and θ . As previously noticed, the removal of the primary contribution of PGV enhances smaller effects resulting from F_i and θ .

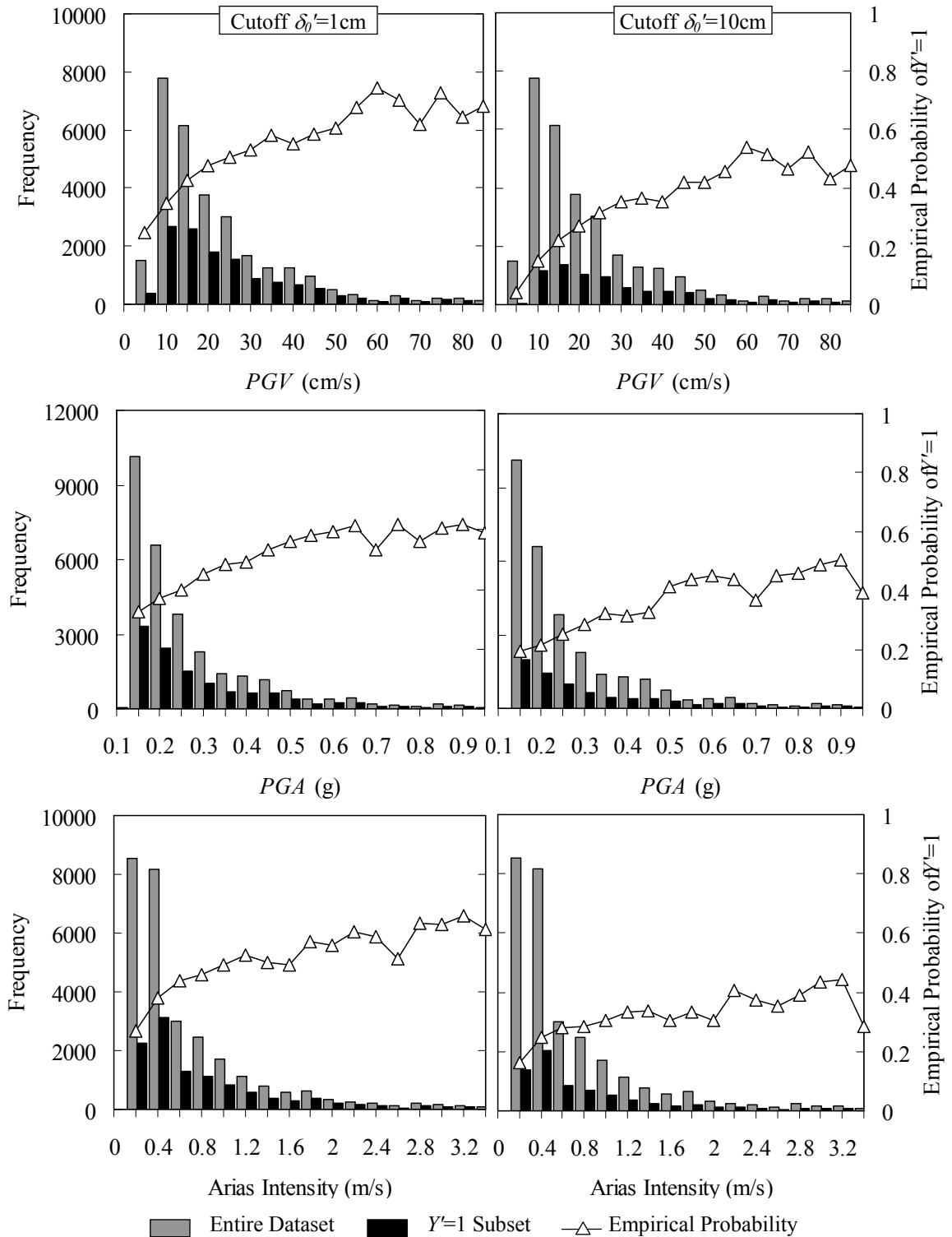


Figure 6.12 Histograms and empirical probabilities for seismic parameters: PGV ; PGA ; Arias Intensity when $\delta_0' = 1$ cm and 10 cm (Y' defined based on δ')

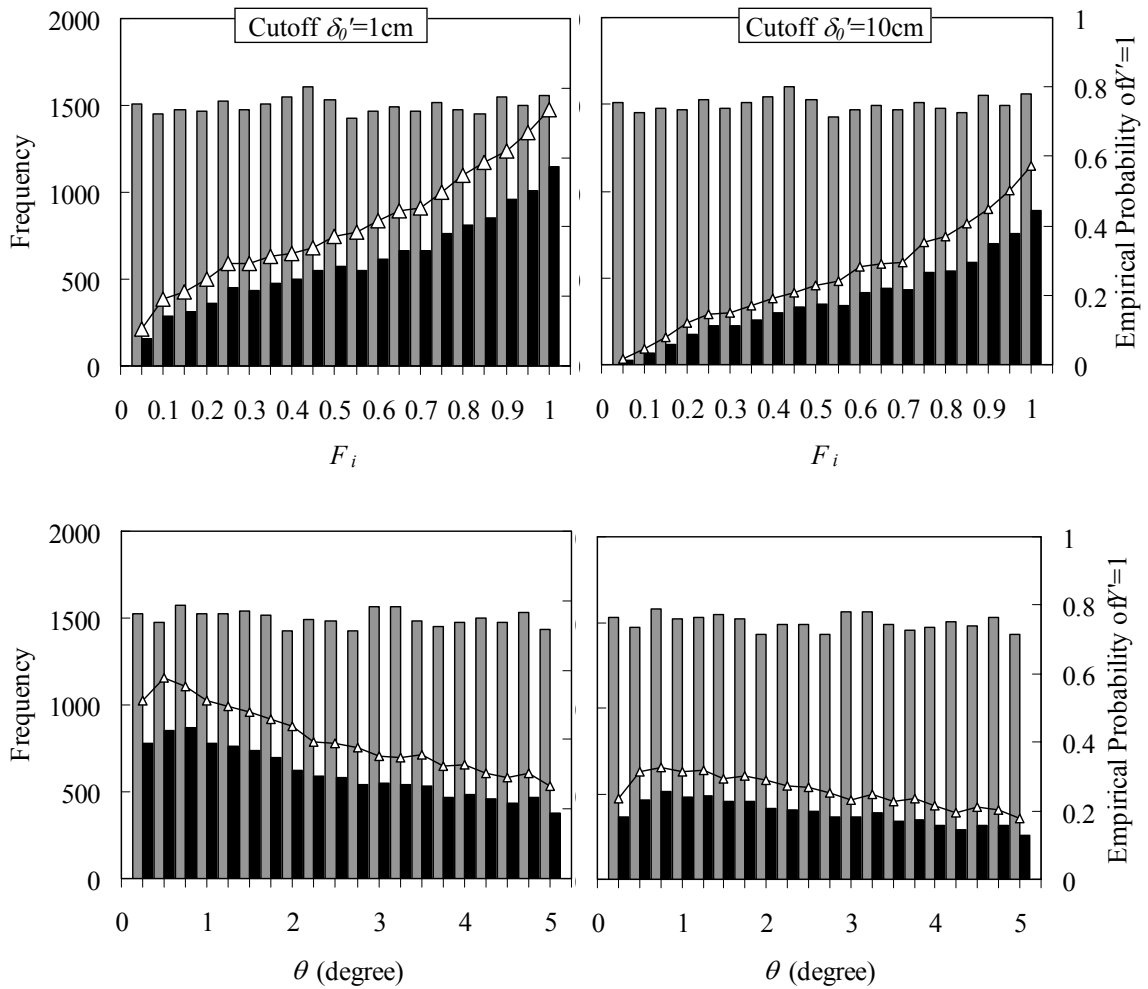


Figure 6.13 Histograms and empirical probabilities for physical parameters F_i and θ when $\delta_0' = 1 \text{ cm}$ and 10 cm

As shown in Figure 6.13, the probability p'_i increases with F_i ; it means that the sloping ground with large reduction in shear strength (i.e., small F_i values) moves largely unaffected by earthquake motions. When soil deposits completely liquefy and the residual shear strength approaches to zero, the earthquake shakings do not affect the

ground motion at all. The combined effects of F_i and θ can be described using the coefficient k_s :

$$k_s = (1 - F_i) \sin \theta \quad (6.11)$$

k_s , which is related to the gravitational force parallel to the ground surface, is an indicator of the degree of instability. k_s varies from 0 (static stability) to $\sin \theta$ (extreme instability). Figure 6.14 shows the histogram of k_s for the entire dataset and $Y'=1$ subset. The probability p'_1 decreases strongly with k_s . Earthquakes are less likely to affect sloping ground after it has become very unstable.

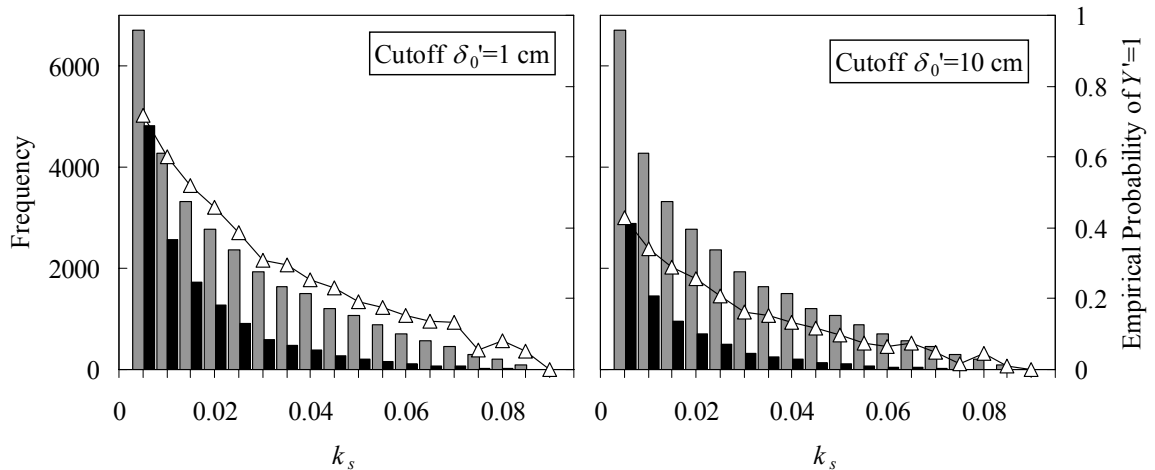


Figure 6.14 Histograms and empirical probabilities of k_s when $\delta_0'=1$ cm and 10cm

Following the approach that led to Equation (11), the following model is obtained to fit the conditional probability for $Y'=1$ given some PGV , k_s and δ_0' values:

$$F'(k_x, PGV) = \begin{cases} \Phi(0.942 \log_{10}(PGV) - 0.822 \log_{10}(k_s) - 2.832) & \text{when } \delta'_0 = 1 \text{ cm} \\ \Phi(1.172 \log_{10}(PGV) - 0.587 \log_{10}(k_s) - 3.277) & \text{when } \delta'_0 = 10 \text{ cm} \end{cases} \quad (6.12)$$

Figure 6.15 shows particular probability curves corresponding to $F_i = 0.9$ and 0.1 , $\delta'_0 = 1$ cm and 10 cm, and $\theta = 1^\circ$ and 5° . The results of Figure 6.15 are reminiscent of those in Figure 6.10. However, they depend on more variables as they describe the contribution of earthquake shaking on gently sloping ground after the onset of instability.

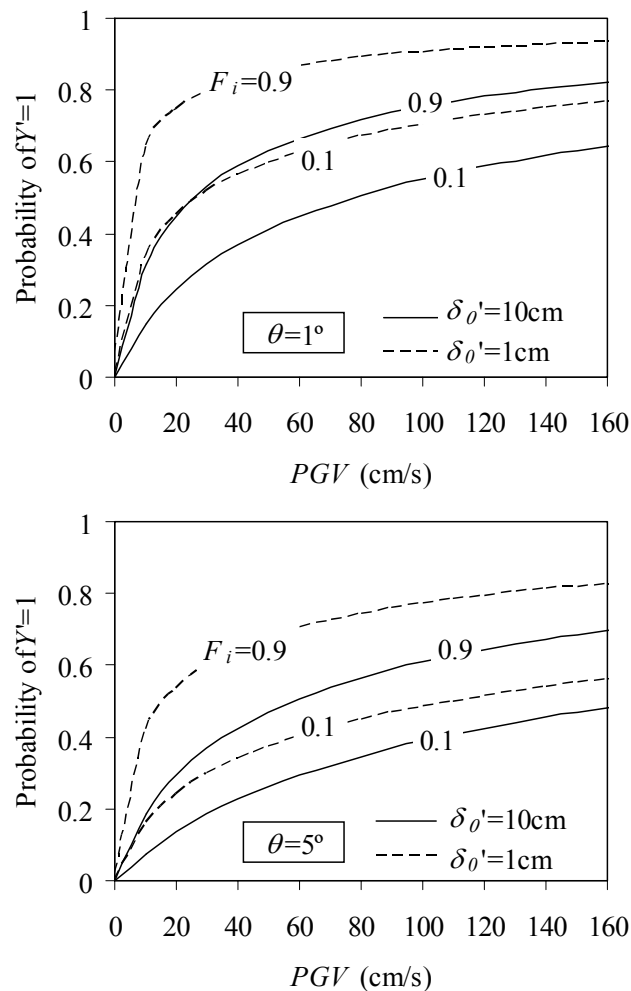


Figure 6.15 Probability curves predicted by Equation (6.12) for various values of F_i , θ and δ'_0

Figures 6.12 to 6.14 are useful to answer the second question about the earthquake contributions that may take place after the onset of instability. Following the onset of instability, under special circumstances when there is severe loss of shear strength, gently sloping ground may move largely unaffected by earthquake shakings. However, in most general cases of moderate reduction in shear strength over extended areas, the motions of gently sloping ground are likely influenced by pulses of earthquake ground velocity.

6.6. Application to Case Histories

The contribution of PGV to the permanent displacement of gently sloping ground, which is shown in Equations 11 and 13, can be investigated using the case histories of liquefaction-induced ground deformations in gently sloping ground that have been documented after past earthquakes (e.g., Bardet et al. 1999; Bartlett and Youd 1992). Table 1 summarizes the main characteristics of a few well-documented case histories containing 242 measurements from five earthquakes with moment magnitude M_w ranging from 6.6 to 9.2. Figure 6.16 shows the histograms of measured total displacement D (m), liquefiable thickness T (m), and slope S (%), *i.e.*, $S = 100 \tan \theta$. T is the cumulative thickness of saturated cohesionless soils (excluding depth >20 m and $>15\%$ clay content) with corrected SPT (Standard Penetration Test) blow counts smaller than 15. To our knowledge, the velocity of liquefaction-induced ground deformation has not been measured directly on gently sloping ground in the field. It has however been measured during shake table tests (e.g., Hadush et al. 2001) and centrifuge tests (e.g., Kulasingam et al. 2004), and it has been found in the order of a few cm/s and to reach maximum of 70

cm/s. As shown in Table 6.1, the values of $PGVs$, which are unavailable from case histories, were either estimated from attenuation relations (e.g., Campbell 1997; Kanno et al. 2006) or inferred from actual seismogram records (Liu and Heaton 1984).

Table 6.1 Summary of case histories of liquefaction-induced lateral ground deformations in gently sloping ground

Earthquake	Number of Cases	M_w	Focal Depth (km)	Epicentral Distance (km)	PGV (cm/s)	Note
1906 San Francisco	2	7.9	8	13, 14	56, 55	Campbell 1997
1964 Alaska	3	9.2	25	35, 100	48, 23	Campbell 1997
1964 Niigata	160	7.5	40	21	58	Kanno et al. 2006
1971 San Fernando	5	6.6	8.4	14	56	Liu and Heaton 1984
1983 Nihokai-Chubu	72	7.7	15	27	60	Kanno et al. 2006

Based on case histories of ground deformations, a few empirical models have been proposed. These models used, instead of PGV , magnitude moment M_w and epicentral distance R . These models can be easily revisited to include the effects of PGV , which were established in the previous probabilistic analysis.

Following the approach of Bardet et al. (2002), a Multiple Linear Regression (MLR) analysis was performed using PGV , T and S as variables (instead of M_w , R , T and S), and yielded the following MLR relation:

$$\log_{10}(D + 0.01m) = 0.364 \log_{10}(S) + 1.461 \log_{10}(PGV) + 0.456 \log_{10}(T) - 2.590 \quad (6.13)$$

where S in (%); PGV in cm/s and T in m.

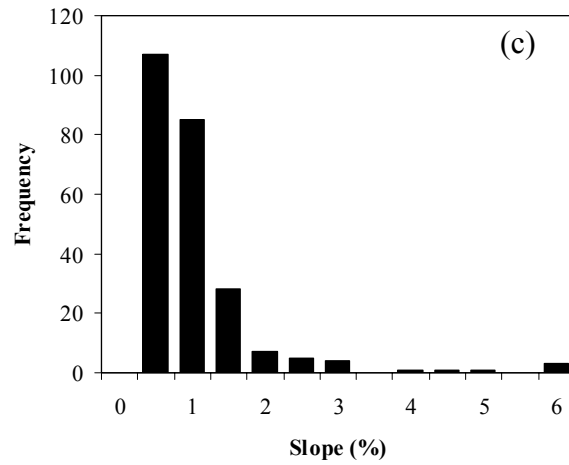
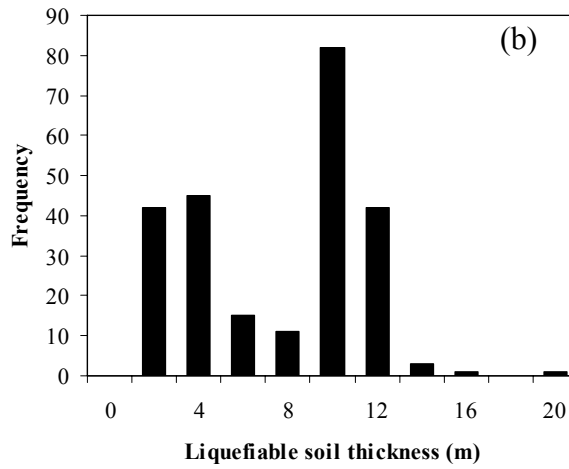
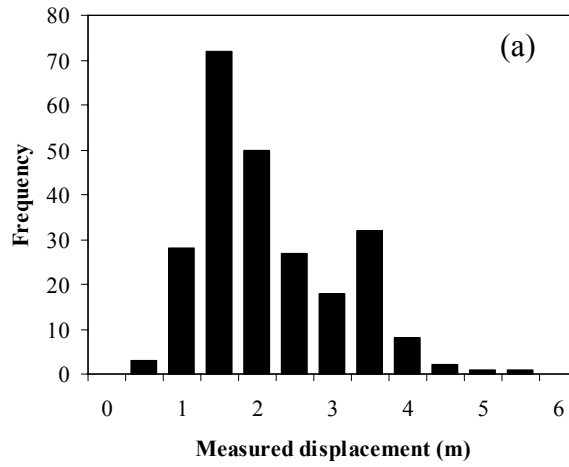


Figure 6.16 Histograms of (a) measured displacements; (b) liquefiable soil thickness; and (c) slope (data after Bartlett and Youd, 1995; Bardet et al., 1999)

Figure 6.17 compares the measured displacements to the values computed from Equation (6.13). In spite of a substantial scatter between predicted and measured values, Figure 6.17 implies that Equation (6.13) predicts liquefaction-induced ground deformations with comparable levels of performance as previous models (i.e., Bardet et al. 2002). It also corroborates the importance of PGV on ground deformation in gently sloping ground, which was derived through physical modeling and probabilistic analyses. Additional work is however required to justify the effects of other physical variables (e.g., k_s).

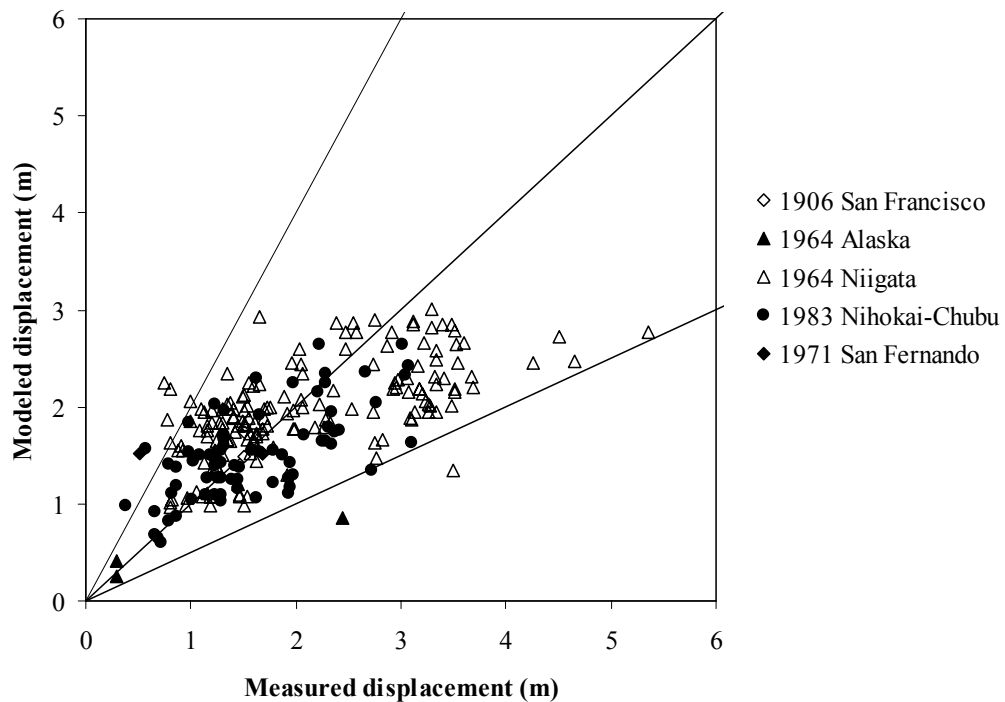


Figure 6.17 Comparison between measured displacement and displacement computed from Equation (6.13)

6.7. Summary

The motions of gently sloping ground during earthquakes have been investigated under the combined effects of transient earthquake shakings, gravity, and partial and total reductions in shear strength of soils resulting from either total liquefaction or partial pore pressure buildups. This study distinguishes the circumstances for which the motions of gently sloping ground may be affected by earthquake shakings and gravity. Based on a physical model and Monte Carlo simulations, it is concluded that the permanent displacements of gently sloping ground are likely influenced by earthquakes, especially through pulses of earthquake ground velocity (e.g., *PGV*). The earthquake transient motions affect primarily the overall motion of unstable ground by initially transferring velocity at the onset of instability, and can still affect its motion after the onset of instability.

Chapter 7. Summary and Conclusions

7.1. Summary of Research

Liquefaction-induced deformations during earthquake pose considerable risks to lifeline systems in urban areas. The empirical predictive models are preferable to other site-specific approaches for the preliminary assessment of liquefaction hazards on regional scales. Those empirical models benefit from a growing number of case histories that require new information technologies of data management. The attempt of this dissertation was to improve the way for managing those case histories in order to develop the next generation of models for regionally predicting liquefaction-induced lateral ground deformations. The major contributions of this dissertation consist of four parts.

The first part of this dissertation looked into the evolution of PER (Post-Earthquake Reconnaissance), in which case histories are collected, documented and distributed. Special attention was put on the potential value of embedded metadata formats that enabled portable files with embedded metadata information. This new technique was applied to an example of the 2008 Wenchuan, China earthquake by automating the generation of PER Web reports. The major findings of this application are: (1) The advances in information technologies have significantly transformed the way PER reports are created and disseminated; (2) The technology of embedded metadata formats is

offering a potential approach for creating the Virtual Earthquake, a global-wide information system for archiving and sharing PER data in a spatial context.

The second part of this dissertation presented a new information system that distributes case histories of liquefaction over the World Wide Web. This system benefits from AJAX (Asynchronous JavaScript and XML), Web and database technology. It takes full advantage of external spatial data offered by multiple data vendors and enables a lightweight Web application with responsive and user-friendly interfaces.

The third part of this dissertation scrutinized the performance of existing empirical models using a subset of case histories that have been managed by the information technologies described in the previous parts. The study site encountered extensive ground failures attributed to liquefaction during two past destructive earthquakes. Three empirical models were integrated into a GIS system for producing maps of liquefaction severity and liquefaction-induced lateral deformations. The disagreement between the simulation results and the field observations infers a knowledge insufficiency in the regional evaluation of liquefaction-induced lateral ground deformations. It therefore raises a demand for the next generation of models that account for physical mechanism as well as statistical analysis of case histories.

The fourth part of this dissertation started the development of the new generation of models for liquefaction-induced lateral ground deformations on regional scales. This study identified earthquake contributions to the motions of unstable mass that has

exhibited temporary losses in shear strength during earthquakes because of liquefaction. A physical model was developed within the framework of the rigid sliding block theory. Base on probabilistic analysis on the propose model, *PGV* (Peak Ground Velocity) was demonstrated to be a dominant seismic parameter that characterizes the earthquake contributions to the motions of unstable mass. Finally, a *PGV*-dependent model was derived from a multiple linear regression analysis on case histories of deformations on gently sloping ground. This new model corroborates the importance of *PGV* on ground deformations, and it is useful for predicting liquefaction-induced lateral ground deformations on regional scales.

7.2. Highlights of Original Contributions

The original contributions of this dissertation are highlighted as follows:

- Embedded metadata formats are first introduced to PER researches for effectively archiving and disseminating PER information on the Internet.
- The rigid sliding block theory is successfully extended to unstable mass that has not been solved by the convention Newmark (1965) seismic deformation analysis because of its reliance on negative yield accelerations.
- Earthquake contributions to the unstable mass motions are identified. *PGV* is demonstrated to be a significant parameter that characterizes the contributions.

- A new *PGV*-dependent model is derived to predict liquefaction-induced lateral ground deformations on large scales. This model corroborates the significance of *PGV* on ground deformations.

References

- Adams, B. J., Mansouri, B., and Huyck, C. K. (2005). "Streamlining post-earthquake data collection and damage assessment for the 2003 Bam, Iran, earthquake using VIEWS (Visualizing Impacts of Earthquakes with Satellites)." *Earthquake Spectra, EERI*, 21(S1), S213-S218.
- Adobe. (2005). "XMP Specification."
<http://partners.adobe.com/public/developer/en/xmp/sdk/XMPspecification.pdf>.
- Ambraseys, N. N., and Menu, J. M. (1988). "Earthquake-induced ground displacements." *Earthquake Engineering and Structural Dynamics*, 16, 985-1006.
- Anagnostopoulos, A., Koukis, G., Sabatakakis, N., and Tsiambaos, G. (2003). "Empirical correlations of soil parameters based on Cone Penetration Tests (CPT) for Greek soils." *Geotechnical and Geological Engineering*, 21, 377-387.
- Arulanandan, K., and Scott, R. F. (1993). "Project VELACS - control test results." *Journal of Geotechnical Engineering*, 119(8), 1276-1292.
- Bardet, J. P. (2003). "Advances in analysis of soil liquefaction during earthquake." *International Handbook of Earthquake and Engineering Seismology*, W. H. K. Lee, H. Kanamori, P. Jennings, and C. Kisslinger, eds., Academic Press, 1175-1201.
- Bardet, J.-P., Hu, J., Tobita, T., and Mace, N. (1999). "Database of case histories on liquefaction-induced ground deformation." Civil Engineering Department, University of Southern California, Los Angeles.
- Bardet, J. P., and Liu, F. (2008). "Motions of gently sloping ground during earthquakes." *submitted to Journal of Geophysical Research - Earth Surface*.
- Bardet, J.-P., Liu, F., and Mokarram, N. "Data and Metadata Modeling for the George E. Brown Jr. Network for Earthquake Engineering Simulation." *EURODYN - Proceedings of the 6th International Conference on Structural Dynamics*, Paris, France.
- Bardet, J.-P., Oka, F., Sugito, M., and Yashima, A. (1995). "The Great Hanshin Earthquake Disaster, The 1995 South Hyogo Prefecture Earthquake, Preliminary Investigation Report." Civil and Environmental Engineering Department,

University of Southern California, Los Angeles, California, USA, and Civil Engineering Department, Gifu University, Gifu, Japan.

- Bardet, J. P., Tobita, T., Mace, N., and Hu, J. (2002). "Regional modeling of liquefaction-induced ground deformation." *Earthquake Spectra, EERI*, 18(1), 19-46.
- Bartlett, S. F., and Youd, T. L. (1992). "Empirical analysis of horizontal ground displacement generated by liquefaction-induced lateral spreads." *Technical Report NCEER-92-0021*, National Center for Earthquake Engineering Research, State University of New York, Buffalo.
- Bartlett, S. F., and Youd, T. L. (1995). "Empirical prediction of liquefaction-induced lateral spread." *Journal of Geotechnical Engineering*, 121(4), 316-329.
- Baziar, M. H., and Dobry, R. (1995). "Residual strength and large-deformation potential of loose silty sands." *Journal of Geotechnical Engineering*, 121(12), 896-906.
- Bennert, T., Maher, A., and Gucunski, N. (2002). "Evaluation of Geotechnical Design Parameters Using the Seismic Piezocone." *FHWA NJ 2001-032*, New Jersey Department of Transportation, CN 600, Trenton, NJ.
- Bierens, H. J. (2007). "EasyReg International." Department of Economics, Pennsylvania State University.
- Biondi, G., Cascone, E., and Maugeri, M. (2002). "Flow and deformation failure of sandy slopes." *Soil Dynamics and Earthquake Engineering*, 22, 1103-1114.
- Cai, Z., and Bathurst, R. J. (1996). "Deterministic sliding block methods for estimating seismic displacements of earth structures." *Soil Dynamics and Earthquake Engineering*, 15, 255-268.
- Campbell, K. W. (1997). "Empirical near-source attenuation relationships for horizontal and vertical components of peak ground acceleration, peak ground velocity, and pseudo-absolute acceleration response spectra." *Seismological Research Letters*, 68(1), 154-179.
- Chang, Y.-S., and Park, H.-D. (2004). "Development of a web-based Geographic Information System for the management of borehole and geologic data." *Computers & Geoscience*, 30, 887-897.
- Davis, C. (2007). Personal communication.
- Donnellan, A., Parker, J. W., and Peltzer, G. (2002). "Combined GPS and InSAR models of postseismic deformation from the Northridge earthquake." *Pure and Applied Geophysics*, 159, 2261-2270.

- Green, R. A. (2001). "Energy-based evaluation and remediation of liquefiable soils," PhD, Virginia Polytechnic Institute and State University, Blacksburg, Virginia.
- Greene, W. H. (2000). *Econometric Analysis*, Prentice-Hall, Inc, Upper Saddle River, New Jersey.
- Hadush, S., Yashimaa, A., Uzuokab, R., Moriguchia, S., and Sawadaa, K. (2001). "Liquefaction induced lateral spread analysis using the CIP method." *Computers and Geotechnics*, 28(8), 549-574.
- Hamada, M., Isoyama, R., and Wakamatsu, K. (1996a). "The 1995 Hyogoken-Nanbu (Kobe) earthquake, liquefaction, ground displacement and soil condition in Hanshin area." The School of Science and Engineering, Waseda University, Japan Engineering Consultants.
- Hamada, M., Isoyama, R., and Wakamatsu, K. (1996b). "Liquefaction-induced ground displacement and its related damage to lifeline facilities." *Soils and Foundations*(Special Issue 1), 81-97.
- Hamada, M., Yasuda, S., Isoyama, R., and Emoto, K. (1986). "Study on liquefaction induced permanent ground displacement." Association for the Development of Earthquake Prediction, Tokyo, Japan.
- Holzer, T. L., Borchardt, R. D., Comartin, C. D., Hanson, R. D., Scawthorn, C. R., Tierney, K., and Youd, T. L. (2003). "The plan to coordinate NEHRP post-earthquake investigations." *Circular 1242*, U.S. Geological Survey, Reston, Virginia.
- Hu, J. (2003). "Modeling of ground deformation using spatial analysis and elasto-plastic finite strain theory," PhD, University of Southern California, Los Angeles, CA.
- Hughes, T. J. R. (2000). *The Finite Element Method: Linear Static, and Dynamic Finite Element Analysis*, Dover Publications, Inc.
- Ingles, J., Darrozes, J., and Soula, J.-C. (2006). "Effects of the vertical component of ground shaking on earthquake-induced landslide displacement using generalized Newmark analysis." *Engineering Geology*, 86, 134-147.
- Iwasaki, T., Tatsuoka, F., Tokida, K., and Yasuda, S. "A practical method for assessing soil liquefaction potential based on case studies at various sites in Japan." *2nd International Conference on Microzonation*, San Francisco, 885-896.
- Iwasaki, T., Tokida, K., Tatsuoka, F., Watanabe, S., Yasuda, S., and Sato, H. "Microzonation for soil liquefaction potential using simplified methods." *3rd International Earthquake Microzonation Conference*, Seattle, 1319-1330.

- Jefferies, M. G., and Davies, M. P. (1993). "Use of the CPTu to Estimate Equivalent SPT N60." *Geotechnical Testing Journal*, 16(4), 458-468.
- Jibson, R. W. (1993). "Predicting earthquake-induced landslide displacements using Newmark's sliding block analysis." *Transportation Research Record 1411*, Transportation Research Board.
- Jibson, R. W. (2007). "Regression models for estimating coseismic landslide displacement." *Engineering Geology*, 91, 209-218.
- Jibson, R. W., Harp, E. L., and Michael, J. A. (2000). "A method for producing digital probabilistic seismic landslide hazard maps." *Engineering Geology*, 58, 271-289.
- Kagawa, T., Abe, A., Ogawa, N., and Minowa, C. "Shaking-table tests on a real-size pile foundation in liquefying sand." *Proceedings of SMIRT 14th Conference*.
- Kanno, T., Narita, A., Morikawa, N., Fujiwara, H., and Fukushima, Y. (2006). "A new attenuation relation for strong ground motion in Japan based on recorded data." *Bulletin of the Seismological Society of America*, 96(3), 879-897.
- Karube, D., and Kimura, M. (1996). "Damage to foundation of railways structures." *Soils and Foundations*(Special Issue 1), 201-210.
- Kayen, R. E., and Mitchell, J. K. (1997). "Assessment of Liquefaction Potential during Earthquakes by Arias Intensity." *Journal of Geotechnical and Geoenvironmental Engineering*, 123(12), 1162-1174.
- Kokusho, T. (1999). "Water film in liquefied sand and its effect on lateral spread." *Journal of Geotechnical and Geoenvironmental Engineering*, 125(10), 817-826.
- Kokusho, T., and Fujita, K. (2002). "Site investigations for involvement of water films in lateral flow liquefied ground." *Journal of Geotechnical and Geoenvironmental Engineering*, 128(11), 917-925.
- Kokusho, T., and Kojima, T. (2002). "Mechanism for postliquefaction water film generation in layered sand." *Journal of Geotechnical and Geoenvironmental Engineering*, 128(2), 129-137.
- Kramer, S. L. (1996). "Liquefaction." *Geotechnical Earthquake Engineering*, Prentice Hall, Upper Saddle River, N. J.
- Kramer, S. L., and Lindwall, N. (2004). "Dimensionality and directionality effects in Newmark sliding block analyses." *Journal of geotechnical and geoenvironmental engineering*, 130(3), 303-315.

- Kramer, S. L., and Smith, M. W. (1997). "Modified Newmark model for seismic displacements of compliant slopes." *Journal of Geotechnical and Geoenvironmental Engineering*, 123(7), 635-644.
- Kulasingam, R., Malvick, E. J., Boulanger, R. W., and Kutter, B. L. (2004). "Strength loss and localization at silt interlayers in slopes of liquefied sand." *Journal of Geotechnical and Geoenvironmental Engineering, ASCE*, 130(11), 1192-1202.
- Kutter, B. L., Gajan, S., Manda, K. K., and Balakrishnan, A. (2004). "Effects of layer thickness and density on settlement and lateral spreading." *Journal of Geotechnical and Geoenvironmental Engineering*, 130(6), 603-614.
- Liao, S. S. C., and Whitman, R. V. (1986). "Overburden correction factors for SPT in sand." *Journal of Geotechnical Engineering, ASCE*, 112(3), 373-377.
- Lin, J. S., and Whitman, R. V. (1983). "Decoupling approximation to the evaluation of earthquake-induced plastic slip in earth dams." *Earthquake Engineering and Structural Dynamics*, 11(5), 667-678.
- Liu, F., Bardet, J. P., and Vajrapu, S. "Information System for Liquefaction Case Histories." *5th China-Japan-US Trilateral Symposium on Lifeline Earthquake Engineering*, Haikou, China.
- Liu, H.-L., and Heaton, T. (1984). "Array analysis of the ground velocities and accelerations from the 1971 San Fernando, California earthquake." *Bulletin of the Seismological Society of America*, 74(5), 1951-1968.
- Makdisi, F. I., and Seed, H. B. (1978). "Simplified procedure for estimating dam and embankment earthquake-induced deformations." *Journal of Geotechnical Engineering Division, ASCE*, 104(7), 849-867.
- Malvick, E. J., Kutter, B. L., Boulanger, R. W., and Kulasingam, R. (2006). "Shear localization due to liquefaction-induced void redistribution in a layered infinite slope." *Journal of Geotechnical and Geoenvironmental Engineering*, 132(10), 1293-1303.
- Marcuson, W. F., III. (1978). "Definition of terms related to liquefaction." *Journal of Geotechnical Engineering Division, ASCE*, 104(9), 1197-1200.
- Martin, G. R. (2000). "Foundation Design for Liquefaction Induced Lateral Displacements." *MCEER Highway Project 094: Seismic Vulnerability of the Highway System, Annual Report for Research Year 1*, MCEER.
- Martin, G. R., Lew, M., Arulmoli, K., Baez, J. I., Earnest, J., Gharib, F., Goldhammer, J., Hsu, D., Kupferman, K., O'Tousa, J., Rea, C. R., Reeder, W., Simantob, E., and

- Youd, T. L. (1999). "Recommendation Procedures for Implementation of DMG Special Publication 117: Guidelines for Analyzing and Mitigating Liquefaction Hazards in California." Southern California Earthquake Center (SCEC), University of Southern California.
- Matasovic, N., E. Kavazanjian, J., and Giroud, J. P. (1998). "Newmark seismic deformation analysis for geosynthetic covers." *Geosynthetics International*, 5(1-2), 237-263.
- Matsui, T., and Oda, K. (1996). "Foundation damage of structures." *Soils and Foundations*, Special Issue 1, 189-200.
- Miles, S. B., and Ho, C. L. (1999). "Rigorous landslide hazard zonation using Newmark's method and stochastic ground motion simulation." *Soil Dynamics and Earthquake Engineering*, 18, 305-323.
- Miles, S. B., and Keefer, D. K. (2000). "Evaluation of seismic slope-performance models using a regional case study." *Environmental & Engineering Geoscience*, 6(1), 25-39.
- Mogami, T., and Kubu, K. "The behavior of soil during vibration." *3rd International Conference on Soil Mechanics and Foundation Engineering*, Zurich, 152-155.
- Mokarram, N. (2006). "Data modeling and integration in geotechnical engineering." *PhD Dissertation Proposal*, Civil and Environmental Engineering Department, University of Southern California, Los Angeles, California.
- Newmark, N. M. (1965). "Effect of earthquake on dams and embankments." *Geotechnique*, 15(2), 139-159.
- Oka, K., Sugito, M., and Yashima, A. (1995a). "The Great Hanshin Earthquake Disaster; The January 17, 1995, South Hyogo Prefecture Earthquake, Preliminary Investigation Report: Part 1." Civil Engineering Department, Gifu University, Gifu, Japan.
- Oka, K., Sugito, M., and Yashima, A. (1995b). "The Great Hanshin Earthquake Disaster; The January 17, 1995, South Hyogo Prefecture Earthquake, Preliminary Investigation Report: Part 2,." Civil Engineering Department, Gifu University, Gifu, Japan.
- Olson, S. M., and Stark, T. D. (2002). "Liquefied strength ratio from liquefaction flow failure case histories." *Canadian Geotechnical Journal*, 39, 629-647.

- Purvis, M., Sambells, J., and Turner, a. C. (2006). "Optimizing and Scaling for Large Data Sets." *Beginning Google Maps Applications with PHP and Ajax: From Novice to Professional*, Apress.
- Rathje, E. M., and Bray, J. D. (2000). "Nonlinear coupled seismic sliding analysis of earth structures." *Journal of Geotechnical and Geoenvironmental Engineering*, 126(11), 1002-1014.
- Rauch, A. F. (1997). "EPOLLS: An Empirical Method for Predicting Surface Displacements Due to Liquefaction-Induced Lateral Spreading in Earthquakes," PhD thesis, Virginia Polytechnic Institute and State University.
- Robertson, P. K., Campanella, R. G., and Wightman, A. (1983). "SPT-CPT correlations." *Journal of Geotechnical Engineering*, 109(11), 1449-1459.
- Robertson, P. K., and Wride, C. E. (1998). "Evaluating cyclic liquefaction potential using the cone penetration test." *Canadian Geotechnical Journal*, 35(3), 442-459.
- Sarma, S. K. (1975). "Seismic stability of earth dams and embankments." *Geotechnique*, 25(4), 743-761.
- Schutzberg, A. (2005). "The Technology Behind Google Maps." *Directions Magazine*, http://www.directionsmag.com/article.php?article_id=760&trv=1.
- Seed, H. B. (1968). "Landslides during earthquakes due to soil liquefaction." *Journal of Soil Mechanics and Foundation Division, ASCE*, 94(SM5), 1053-1122.
- Seed, H. B. (1979). "Soil liquefaction and cyclic mobility evaluation for level ground during earthquakes." *Journal of Geotechnical Engineering Division, ASCE*, 105(GT2), 201-255.
- Seed, H. B., and Idriss, I. M. (1971). "Simplified procedure for evaluating soil liquefaction potential." *Journal of Geotechnical Engineering Division, ASCE*, 97(9), 1249-1273.
- Seed, H. B., and Idriss, I. M. (1982). "Ground motions and soil liquefaction during earthquakes." Earthquake Engineering Research Institute, Berkeley, California.
- Seed, H. B., Tokimatsu, K., Harder, L. F., and Chung, R. M. (1985). "The influence of SPT procedures in soil liquefaction resistance evaluations." *Journal of Geotechnical Engineering, ASCE*, 111(12), 1425-1445.
- Sezen, H., Elwood, K. J., Whittaker, A. S., Mosalam, K. M., Wallace, J. W., and Stanton, J. F. (2000). "Structural Engineering Reconnaissance of the August 17, 1999 Earthquake: Kocaeli (Izmit), Turkey." *PEER Report 2000/09*, Pacific Earthquake

Engineering Research Center, College of Engineering, University of California, Berkeley, Berkeley, CA.

- Sharp, M. K., Dobry, and Abdoun, T. (2003). "Liquefaction centrifuge modeling of sands of different permeability." *Journal of Geotechnical and Geoenvironmental Engineering*, 129(12), 1083-1091.
- Sonmez, H. (2003). "Modification of the liquefaction potential index and liquefaction susceptibility mapping for a liquefaction-prone area (Inegol, Turkey)." *Environmental Geology*, 44(7), 862-871.
- Taboada, V. M., and Dobry, R. (1998). "Centrifuge modeling of earthquake-induced lateral spreading in sand." *Journal of Geotechnical and Geoenvironmental Engineering*, 124(12), 1195-1206.
- Tokimatsu, K., Mizumo, H., and Kakurai, M. (1996). "Building damage associated with geotechnical problems." *Soils and Foundations*(Special Issue 1), 219-234.
- Towhata, I. "Development of geotechnical earthquake engineering in Japan." *the Proceedings 16th International Conference on Soil Mechanics and Geotechnical Engineering*, Osaka, Japan, 251-291.
- Towhata, I., Orense, R. P., and Toyota, H. (1999). "Mathematical principles in prediction of lateral ground displacement induced by seismic liquefaction." *Soils and Foundations*, 39(2), 1-19.
- Trifunac, M. D., and Brady, A. G. (1975). "A study on duration of strong earthquake ground motion." *Bulletin of the Seismological Society of America*, 65, 581-626.
- USGS. (1996). "USGS Response to an Urban Earthquake:Northridge '94." *Open-File Report 96-263*.
- Wartman, J., and Bray, J. D. (2003). "Inclined plane studies of the Newmark sliding block procedure." *Journal of Geotechnical and Geoenvironmental Engineering*, 129(8), 673-684.
- Werner, S. D., Taylor, C. E., Cho, S., Lavoie, J.-P., Huyck, C., Eitzel, C., Chung, H., and Eguchi, R. T. (2006). "REDARS 2 Methodology and software for seismic risk analysis of highway systems." *Special Report MCEER-06-SP08*.
- Whittaker, A., Moehle, J., and Higashino, M. (1998). "Evolution of seismic building design practice in Japan." *The Structural Design of Tall and Special Buildings*, 7(2), 93-111.

- Wilson, R. C., and Keefer, D. K. (1983). "Dynamic analysis of a slope failure from the 6 August, 1979 Coyote Lake, California, earthquake." *Seismological Society of America Bulletin*, 73(3), 863-877.
- Wusteman, J., and O'hleceadha, P. (2006). "Using AJAX to empower dynamic searching." *Information Technology and Libraries*, 25(2), 57-64.
- Yan, L., Matasovic, N., and Kavazanjian, E. J. "Seismic response of rigid block on inclined plane to vertical and horizontal ground motions acting simultaneously." *11th ASCE Engineering Mechanics Conference*, Ft. Lauderdale, Fla., 1111-1113.
- Yegian, M. K., Ghahraman, V. G., Nogole-Sadat, M. A. A., and Daraie, H. (1995). "Liquefaction during the 1990 Manjil, Iran, earthquake, II: case history analysis." *Bulletin of the Seismological Society of America*, 85(1), 83-92.
- Yegian, M. K., Marciano, E. A., and Gharaman, V. G. (1991). "Earthquake-induced permanent deformation: probabilistic approach." *Journal of Geotechnical Engineering Division, ASCE*, 117(1), 35-50.
- Youd, T. L. (1978). "Major cause of earthquake damage is ground failure." *Civil Engineering*, 48, 47-51.
- Youd, T. L., Bardet, J.-P., and Bray, J. (2000). "The 1999 Kocaeli, Turkey, Earthquake." *Earthquake Spectra*, EERI, 462.
- Youd, T. L., Hansen, C. M., and Bartlett, S. F. (2002). "Revised multilinear regression equations for prediction of lateral spread displacement." *Journal of Geotechnical and Geoenvironmental Engineering*, 128(12), 1007-1017.
- Youd, T. L., Idriss, I. M., Andrus, R. D., Arango, I., Castro, G., Christian, J. T., Dobry, R., Finn, W. D. L., Harder, L. F., Jr., Hynes, M. E., Ishihara, K., Koester, J. P., Liao, S. S. C., Marcuson, W. F., III, Martin, G. R., Mitchell, J. K., Moriwaki, Y., Power, M. S., Robertson, P. K., Seed, R. B., and Stokoe, K. H., II. (2001). "Liquefaction resistance of soils: summary report from the 1996 NCEER and 1998 NCEER/NSF workshops on evaluation of liquefaction resistance of soils." *Journal of Geotechnical and Geoenvironmental Engineering*, 127(1), 817-833.
- Youd, T. L., and Perkins, D. M. (1987). "Mapping of liquefaction severity index." *Journal of Geotechnical Engineering*, 11, 1374-1392.
- Zhang, G., Robertson, P. K., and R. W. I. Brachman. (2004). "Estimating liquefaction-induced lateral displacements using the standard penetration test or cone penetration test." *Journal of Geotechnical and Geoenvironmental Engineering*, 130(8), 861-871.

Zhang, J., and Zhao, J. X. (2005). "Empirical models for estimating liquefaction-induced lateral spread displacement." *Soil Dynamics and Earthquake Engineering*, 25, 439-450.

Zimmermann, R., Ku, W.-S., Wang, H., Zand, A., and Bardet, J.-P. (2006). "A Distributed Geotechnical Information Management and Exchange Architecture." *Internet Computing, IEEE*, 10(5), 26-33.

Appendix A Tabulated Results of Case Study

Computation results for available CPT tests are summarized in the following table ($X - x$ coordinates in California, Zone VII of NAD27; $Y - y$ coordinates in California, Zone VII of NAD27; GWD – groundwater table depth; D_1 – displacement calculated from Bardet et al. model; D_2 – displacement calculated from Youd et al. model; D_3 – displacement calculated from Zhang et al. model):

Table A.1 Calculation results of case study

ID	X (m)	Y (m)	GWD (m)	LPI	T_{15} (m)	Slope (%)	D_{5015} (mm)	F_{15} (%)	LDI (cm)	D_1 (m)	D_2 (m)	D_3 (m)
2	1261734	1286981	3.4	8	0.45	3.34	0.92	10.94	77.7	0.24	0.13	2.75
3	1261731	1286963	3.4	4	0.00	3.04			48.8	0.00	0.00	1.58
4	1261298	1287276	8.2	1	0.02	5.00	0.64	14.79	17.8	0.11	0.03	0.93
5	1261292	1287272	3.4	0	0.00	5.90			3.3	0.00	0.00	0.20
6	1261316	1287287	1.8	8	0.08	3.79	1.27	9.86	75.1	0.14	0.05	3.00
7	1261421	1287652	0.6	9	0.20	1.88	0.75	12.75	63.6	0.17	0.06	1.32
8	1261421	1287651	0.6	7	0.37	1.88	0.55	13.47	45.0	0.20	0.09	0.94
9	1261468	1288039	0.6	6	0.45	1.09	0.89	11.36	25.9	0.19	0.09	0.33
10	1261463	1288044	0.6	2	0.38	1.09	0.80	10.91	25.9	0.18	0.08	0.33
11	1261574	1288223	3.0	2	0.03	2.44	0.87	11.60	30.7	0.09	0.02	0.81
12	1261599	1288141	1.8	2	0.00	1.88			35.5	0.00	0.00	0.74
13	1261608	1288049	1.8	3	0.00	1.27			39.0	0.00	0.00	0.57
14	1261608	1287988	3.0	1	0.03	1.19	2.70	1.82	10.6	0.08	0.03	0.15
15	1261891	1287621	3.7	0	0.00	2.36	0.00	0.00	2.5	0.00	0.00	0.06
16	1261515	1288034	0.5	16	0.35	1.15	0.91	11.74	110.9	0.18	0.08	1.49
17	1261558	1288146	1.8	11	0.48	1.61	1.02	11.69	80.3	0.21	0.10	1.45
18	1261569	1288076	2.1	1	0.00	1.34			18.3	0.00	0.00	0.28
19	1261528	1288135	0.3	6	0.28	1.38	0.99	10.77	52.2	0.17	0.07	0.82
20	1261435	1288043	0.5	14	0.98	1.05	1.23	9.90	76.4	0.24	0.14	0.95
21	1261256	1287445	6.4	18	1.38	1.40	1.11	13.06	245.6	0.28	0.16	3.92
22	1261854	1287619	0.6	2	0.00	2.07			26.8	0.00	0.00	0.61
23	1261874	1287584	0.9	0	0.00	2.51			7.3	0.00	0.00	0.20
24	1261814	1287686	0.9	5	0.00	1.30			39.1	0.00	0.00	0.58

Table A.1 Continued

ID	X (m)	Y (m)	GWD (m)	LPI	T_{15} (m)	Slope (%)	D_{5015} (mm)	F_{15} (%)	LDI (cm)	D_1 (m)	D_2 (m)	D_3 (m)
25	1261836	1287648	0.9	6	0.00	1.71			42.1	0.00	0.00	0.80
26	1261802	1287707	2.1	4	0.30	1.20	0.75	11.62	31.7	0.17	0.07	0.44
27	1261749	1287774	2.4	1	0.02	1.09	0.84	14.69	16.5	0.08	0.02	0.21
28	1261475	1287901	4.0	7	0.05	1.45	1.02	11.89	68.2	0.10	0.03	1.12
29	1261484	1288368	5.2	0	0.00	3.16			0.0	0.00	0.00	0.00
30	1261484	1288368	5.2	1	0.00	3.16			16.0	0.00	0.00	0.54
31	1261384	1287650	9.4	1	0.03	1.84	0.64	14.27	29.0	0.09	0.02	0.59
32	1261287	1287507	8.2	2	0.00	1.34			36.0	0.00	0.00	0.55
33	1261391	1287650	5.2	3	0.02	1.85	0.57	14.84	54.6	0.09	0.02	1.12
34	1261896	1287611	4.0	0	0.00	2.57			3.3	0.00	0.00	0.09
35	1261875	1287649	3.7	0	0.00	1.84			0.8	0.00	0.00	0.02
36	1261779	1286999	3.4	7	0.00	3.10			82.2	0.00	0.00	2.71
39	1261194	1287206	6.6	0	0.00	16.21				0.00	0.00	0.00
40	1261205	1287171	6.6	0	0.00	19.17				0.00	0.00	0.00
41	1261237	1287207	6.6	0	0.00	14.41			0.0	0.00	0.00	0.00
109	1261061	1287427	15.2	0	0.00	2.41			0.1	0.00	0.00	0.00
110	1261129	1287703	15.3	0	0.00	2.61			7.4	0.00	0.00	0.21
111	1261151	1287871	14.6	0	0.00	3.70			0.0	0.00	0.00	0.00
112	1261229	1287953	17.6	0	0.00	3.01			2.1	0.00	0.00	0.07
114	1261266	1288055	15.9	0	0.00	3.47			3.1	0.00	0.00	0.11
115	1261179	1288106	17.7	0	0.00	6.52			0.0	0.00	0.00	0.00
116	1261192	1288180	16.9	0	0.00	7.66			8.9	0.00	0.00	0.70
117	1261222	1288260	15.6	0	0.00	8.18			0.1	0.00	0.00	0.01
118	1261303	1288217	15.4	0	0.00	4.07			0.0	0.00	0.00	0.00
121	1261313	1288351	15.1	0	0.00	5.28			0.0	0.00	0.00	0.00
122	1261323	1288493	12.4	0	0.00	8.41			0.0	0.00	0.00	0.00
123	1261285	1288545	9.9	0	0.00	14.49			5.8	0.00	0.00	0.85
124	1261336	1288640	8.0	0	0.00	6.29			0.0	0.00	0.00	0.00
125	1261401	1288516	7.4	1	0.00	3.47			3.0	0.00	0.00	0.11
126	1261207	1288436	16.6	0	0.00	19.94			5.1	0.00	0.00	1.02
127	1261123	1288287	14.4	0	0.00	11.37			14.0	0.00	0.00	1.62
128	1261045	1288375	16.5	0	0.00	19.33			0.0	0.00	0.00	0.00
129	1260981	1288264	16.5	0	0.00	12.67			0.0	0.00	0.00	0.00
130	1261079	1288227	15.3	0	0.00	9.57			0.0	0.00	0.00	0.00
131	1260922	1288347	30.1	0	0.00	16.44			0.0	0.00	0.00	0.00
132	1260927	1288201	15.5	0	0.00	9.92			0.0	0.00	0.00	0.00
133	1260881	1288105	14.3	0	0.00	9.21			0.0	0.00	0.00	0.00
134	1261026	1288036	14.4	0	0.00	8.92			0.0	0.00	0.00	0.00
135	1261118	1287991	16.6	0	0.00	6.11			0.0	0.00	0.00	0.00
136	1261023	1287918	14.2	0	0.00	6.40			0.0	0.00	0.00	0.00
137	1260942	1287871	13.8	0	0.00	6.48			23.0	0.00	0.00	1.54
138	1260912	1287963	13.2	0	0.00	8.18			0.4	0.00	0.00	0.03

Table A.1 Continued

ID	<i>X</i> (m)	<i>Y</i> (m)	GWD (m)	<i>LPI</i>	<i>T</i> ₁₅ (m)	Slope (%)	<i>D</i> ₅₀₁₅ (mm)	<i>F</i> ₁₅ (%)	<i>LDI</i> (cm)	<i>D</i> ₁ (m)	<i>D</i> ₂ (m)	<i>D</i> ₃ (m)
140	1261051	1287832	16.0	0	0.00	5.11			0.0	0.00	0.00	0.00
141	1261020	1287749	18.7	0	0.00	4.39			0.0	0.00	0.00	0.00
142	1260908	1287798	14.8	0	0.00	5.39			4.9	0.00	0.00	0.28
143	1260824	1288002	11.4	0	0.00	7.26			0.0	0.00	0.00	0.00
144	1260764	1287862	10.8	0	0.00	5.68			0.0	0.00	0.00	0.00
145	1260711	1287703	9.9	0	0.00	4.97			0.0	0.00	0.00	0.00
148	1260699	1287590	16.5	0	0.00	4.17			0.0	0.00	0.00	0.00
149	1260821	1287563	21.3	0	0.00	3.26			4.3	0.00	0.00	0.15
150	1260921	1287515	20.3	0	0.00	2.98			0.4	0.00	0.00	0.01
151	1260878	1287421	19.7	0	0.00	4.28			0.1	0.00	0.00	0.01
152	1260759	1287466	21.3	0	0.00	2.80			0.0	0.00	0.00	0.00
153	1261045	1287587	16.6	0	0.00	2.86			0.7	0.00	0.00	0.02
155	1261111	1287560	15.8	0	0.00	2.38			0.0	0.00	0.00	0.00
158	1261016	1287302	14.3	0	0.00	8.16			0.8	0.00	0.00	0.07
165	1260955	1287362	15.6	0	0.00	4.96			1.2	0.00	0.00	0.06
166	1260715	1287521	4.7	0	0.00	3.16			0.0	0.00	0.00	0.00
167	1260742	1287553	4.5	0	0.00	3.39			2.7	0.00	0.00	0.10
168	1260750	1287571	3.5	0	0.00	3.50			4.9	0.00	0.00	0.18
169	1260805	1287480	1.0	2	0.20	3.21	0.97	8.55	5.4	0.19	0.09	0.18
170	1260822	1287515	5.3	0	0.00	3.10			0.0	0.00	0.00	0.00
171	1260815	1287567	6.5	3	0.20	3.26	1.10	11.27	25.0	0.19	0.08	0.87
172	1260898	1287557	6.2	1	0.00	3.14			3.5	0.00	0.00	0.12
173	1260860	1287528	8.9	0	0.00	3.18			57.1	0.00	0.00	1.93
174	1260863	1287483	2.5	0	0.00	3.41			21.4	0.00	0.00	0.77
175	1260776	1287521	4.3	1	0.10	2.99	1.21	8.04	5.5	0.15	0.06	0.18
176	1260758	1287500	3.8	0	0.00	2.96			3.1	0.00	0.00	0.10
177	1260740	1287603	1.5	3	0.00	4.01			5.4	0.00	0.00	0.23
178	1260775	1287499	3.1	0	0.00	2.88			2.1	0.00	0.00	0.06
179	1260788	1287491	1.7	2	0.00	2.96			34.1	0.00	0.00	1.08
180	1260837	1287486	7.8	0	0.00	3.20			0.0	0.00	0.00	0.00
181	1260838	1287503	6.8	1	0.00	3.06			26.3	0.00	0.00	0.86
182	1260837	1287519	6.2	0	0.00	3.11			6.0	0.00	0.00	0.20
183	1260736	1287511	4.4	1	0.00	3.00			13.9	0.00	0.00	0.45
184	1260721	1287569	0.0	11	0.20	3.72	0.75	12.92	1.0	0.19	0.08	0.04
185	1260710	1287551	0.5	3	0.00	3.59			11.3	0.00	0.00	0.43
186	1260764	1287547	4.6	0	0.00	3.15			97.7	0.00	0.00	3.27
187	1260800	1287550	2.5	3	0.00	3.18			39.8	0.00	0.00	1.34
188	1260860	1287560	0.0	5	0.20	3.20	0.66	13.45	1.9	0.19	0.07	0.07
189	1260784	1287585	2.2	0	0.00	3.53			43.7	0.00	0.00	1.63
190	1260743	1287578	3.4	0	0.00	3.74			52.4	0.00	0.00	2.07
191	1260763	1287595	2.4	0	0.00	3.68			10.7	0.00	0.00	0.41
192	1262494	1287985	5.0	0	0.00	4.35			11.3	0.00	0.00	0.51

Table A.1 Continued

ID	<i>X</i> (m)	<i>Y</i> (m)	GWD (m)	<i>LPI</i>	<i>T</i> ₁₅ (m)	Slope (%)	<i>D</i> ₅₀₁₅ (mm)	<i>F</i> ₁₅ (%)	<i>LDI</i> (cm)	<i>D</i> ₁ (m)	<i>D</i> ₂ (m)	<i>D</i> ₃ (m)
193	1262504	1288036	4.5	0	0.00	3.86			3.3	0.00	0.00	0.14
194	1262518	1288088	5.9	0	0.00	3.06			1.0	0.00	0.00	0.03
195	1262531	1288165	4.5	0	0.00	2.38			12.0	0.00	0.00	0.31
197	1262582	1288078	5.9	0	0.00	3.38			0.3	0.00	0.00	0.01
198	1262560	1287981	7.0	0	0.00	4.83			1.3	0.00	0.00	0.07
199	1262629	1288070	5.8	1	0.00	3.35				0.00	0.00	0.00
200	1262692	1288056	5.5	0	0.00	2.77			17.2	0.00	0.00	0.51
201	1262610	1288032	5.1	1	0.00	3.94			0.0	0.00	0.00	0.00
202	1262346	1287979	4.2	0	0.00	1.95			43.2	0.00	0.00	0.93
203	1262323	1288022	4.5	0	0.00	2.02			10.5	0.00	0.00	0.23
204	1262361	1288061	4.7	0	0.00	2.28			16.5	0.00	0.00	0.41
205	1262337	1288071	4.6	0	0.00	2.31			2.9	0.00	0.00	0.07
206	1262264	1288116	4.3	1	0.00	2.42			0.6	0.00	0.00	0.02
207	1262291	1288088	5.8	0	0.00	2.37			0.3	0.00	0.00	0.01
208	1262359	1288147	5.3	0	0.00	2.41			0.7	0.00	0.00	0.02
209	1262192	1288044	5.1	0	0.00	2.06			8.8	0.00	0.00	0.20
210	1262126	1288166	6.6	2	0.00	2.35			0.2	0.00	0.00	0.01
211	1262221	1288212	7.0	2	0.15	2.40	0.98	11.30	0.1	0.16	0.06	0.00
212	1262264	1287884	4.4	0	0.00	1.54			3.7	0.00	0.00	0.06
213	1262220	1287917	4.7	0	0.00	1.40			13.1	0.00	0.00	0.21
214	1262254	1287939	5.1	0	0.00	1.45			32.5	0.00	0.00	0.54
215	1262229	1287977	4.5	0	0.00	1.63			0.0	0.00	0.00	0.00
216	1262210	1288012	5.1	0	0.00	1.85			0.9	0.00	0.00	0.02
217	1262298	1287967	4.4	0	0.00	1.66			0.8	0.00	0.00	0.01
218	1262261	1287909	5.2	0	0.15	1.43	0.78	14.65	0.3	0.15	0.05	0.00
219	1262273	1287915	5.0	1	0.00	1.55			0.1	0.00	0.00	0.00
220	1262336	1287940	4.4	0	0.00	1.93			0.9	0.00	0.00	0.02